

Trinity College Dublin
Coláiste na Tríonóide, Baile Átha Cliath
The University of Dublin

Study of Kerr Soliton Microcombs in Optical Microresonators

by

Adnan Ali Afridi

Supervised by **Prof. John F. Donegan**

A thesis presented for the degree of Doctor of Philosophy

(2023)

at

School of Physics
Trinity College Dublin

Declaration

I, Adnan Ali Afridi, declare that this thesis has not been submitted as an exercise for a degree at this or any other university and it is entirely my own work.
I agree to deposit this thesis in the University's open access institutional repository or allow the library to do so on my behalf, subject to Irish Copyright Legislation and Trinity College Library conditions of use and acknowledgment.

Signature

Date

Acknowledgements

First and foremost, I would like to thank my supervisor Prof. John F. Donegan, for giving me an opportunity to join his lab as a PhD student. I am extremely grateful for his extraordinary support, motivation, friendly environment and invaluable guidance during the course of my PhD studies. I am also thankful for his trust and let me a part of an enthusiastic team in building the soliton experimental setup. Moreover, without his constant availability for discussion and well-informed suggestions will not be possible to get many new ideas and excellent research output. The time spent and fruitful suggestions in preparing manuscripts and theses will never be forgotten.

I owe special thanks to Dr. Haizhong Weng who introduced me to optical microresonators and frequency combs. I was fortunate for being together with him in the lab, his mentoring and expertise helped me a lot during my course of study. I would like to appreciate his long fruitful discussions in understanding the simulations, soliton dynamics, and careful attention in preparing the results. Besides this, I appreciate his pleasant personality and friendship and enjoyed occasionally traveling together to amazing places in Ireland.

I thanks a lot to our collaborators Prof. Weihua Guo and Dr. Jia Liu for their support. We are grateful for their hard and excellent work on the fabrication of aluminum nitride devices. I thank Prof. Weihua Guo for his knowledgeable feedback and advice on both the simulation and experimental parts. I also appreciate you joining our group meetings despite having a busy schedule.

I am also thankful to Dr. Jing Li for introducing me to a clean-room. I appreciate his efforts and long hours of hard work in the clean-room on the fabrication part. Apart from research, I had a great time together as office mates and kept a friendly environment. I would also like to thank all our former and present group mates Dr.

Gaurav Jain, Dr. Robert McKenna, and Dr. Chris Murray, Dr. Sepideh Naimi, Michael McDermott, Dovydas Mickus, Caolán Murphy for the wonderful time together. I will not forget to acknowledge and thank the school of physics finance and IT teams. They have been very much supportive all these years and so can I focus on my research.

I thank the science foundation Ireland (SFI) and the national natural science foundation of China (NSFC) for supporting and funding this project.

Last but not least, I would like to thank my parents for their best possible care, motivation, unconditional support in all forms and prayers. Their true love and affection always give me the courage and helped me to move forward and accomplish my goals successfully.

Contents

Declaration i

Acknowledgements ii

Abstract xviii

1 Introduction 1

1.1 Microresonators based optical frequency co-mbs 2

1.1.1 An octave-span microcomb 4

1.1.2 Dissipative Kerr solitons (DKSs) 5

1.2 Mircoresonator theory 6

1.2.1 Transmission and Enhancement factors 9

1.2.2 Free spectral range (FSR) 14

1.2.3 Quality factor (Q) and extinction ratio (ER) 16

2 Dispersion in Microresonators 20

2.1 Optical modes analysis in 2D waveguide 20

2.2 Microresonator platforms used in this work 23

2.3 Microresonator dispersion 25

2.3.1 Group velocity dispersion (GVD) in AlN microresonators . . . 26

2.3.2 Microresonators integrated dispersion (D_{int}) 28

2.4 Conclusion 36

3 Effect of thermal tuning and mode coupling on soliton microcombs in AlN microresonators 37

3.1 Introduction 37

3.1.1 Dual-mode scheme 38

3.2 Device characterization 41
3.3 Experimental setup and generation of an oct-ave-span dissipative Kerr soliton (DKS) 43
3.4 Thermal tuning of resonance modes 46
3.5 Experimental demonstration of an octave-span DKS at different temperatures and tuning soliton existence range (SER) 50
3.5.1 Two-solitons generation 54
3.5.2 Microcombs from other mode families 56
3.6 f_{ceo} characterization measurements 59
3.7 Conclusion 61

4 Breather soliton and soliton crystals in AlN microresonators 63
4.1 Introduction 63
4.2 Device characterization 65
4.3 Experimental demonstration of breather solitons 66
4.3.1 Pumping other TE resonance modes 69
4.3.2 Breather and single soliton generation with various detuning speeds of the laser wavelength 71
4.3.3 Breather and single soliton in TE_{10} mode 73
4.4 Breather soliton crystals (BSCs) 76
4.4.1 Experimental Observation of breather soliton crystals (BSCs) 77
4.5 Conclusion 81

5 Dual-mode scheme single soliton generation and AMX-induced soliton crystals (SCs) in S_3N_4 microresonators 82
5.1 Introduction 82
5.2 Design of dual-mode microresonators and ch-aracterization 84
5.3 Generation of an octave-spanning DKS via dual-modes scheme 88
5.4 Generation of soliton crystals (SCs) 90
5.5 Conclusion 96

6 Conclusion and Future work 98

List of Figures

1.1 (a) Pulse train in conventional mode-locked laser. The cavity round-trip time is T_R and $\Delta\phi$ is pulse envelope phase shift due to the difference in group and phase velocities. (b) An optical spectrum in the frequency domain corresponding to (a), the spectrum consists of discrete equidistant comb lines with frequency repetition rate f_{rep} and offset frequency f_{ceo}. 2

1.2 Schematic illustration of the χ^2 and χ^3 nonlinear parametric process: (a) (i) Second harmonic generation (SHG), where two pump photons generate a new photon with twice the frequencies of the pump (ω+ω=2ω). (ii) Sum/difference frequency generation (SFG/DFG), here a new photon is generated with the frequency equal to the sum/difference of the input (ω_3=ω_1±ω_2). (b) (i) Third harmonic generation (THG), is a nonlinear process where a new photon has triple the frequency of the pump(3ω=ω+ω+ω). (ii) Self- (SPM) and Cross-phase modulations (XPM), in SPM process the intensity of the propagating field induces a modification in the refractive index and in the XPM the co-propagating fields induce modification of the refractive index. (iii) Degenerate FWM is the parametric process where two photons with the same frequencies generate two new photons (2ω_1=ω_2+ω_3). In non-degenerate FWM, the two photons are annihilated and two new photons are generated, satisfying an energy conservation (ω_1+ω_2=ω_3+ω_4). (c) Microresonator-based optical frequency comb spectrum via cascaded FWM processes 1 and 2. 3

1.3 Schematic illustration of f-2f self-reference scheme in an octave-span spectrum. In this scheme, f_n and f_{2n} are the frequencies at the lower and higher end of the spectrum. The lower frequency f_n is doubled via SHG. The beat note of $2f_n$ and f_{2n} can provide the f_{ceo}. 5

1.4 Schematic illustration of dissipative Kerr solitons (DKSs) generation (a) Sketch of effects, such as dispersion balanced by Kerr non-linearity and loss balanced by the gain to maintain the single soliton state. (b) Single soliton in the microresonator cavity and the obtained spectrum at the output. 6

1.5 Sketch of all-pass microresonators with an integrated straight waveguide (a) circular microcavity and (b) racetrack microcavity. 7

1.6 Schematic model of an all-pass microresonator with the zoomed-in sketch of the coupling region. In the coupling region, k and t are the coupling and transmission coefficients whereas E_{c2} and E_{c1} are the fields coupling into and out of the microcavity. The input and output fields are E_{in} and E_{out} as well as α_{ring} is the amplitude of cavity intrinsic losses per around-trip, respectively. 8

1.7 Calculated transmission and enhancement factors versus t/a ratio for a 60-μm-radius AlN microresonator. 11

1.8 Transmissions spectra versus wavelength in over-coupling ($t/a<1$), critical coupling ($t=a$) and under-coupling ($t/a>1$) conditions. 12

1.9 Power enhancement (B) spectra versus wavelength in over-coupling ($t/a<1$), critical coupling ($t=a$) and under-coupling ($t/a>1$) conditions. 12

1.10 Calculated phase shifts (a) over-coupling ($t/a<1$), a continuous phase shift of 2π (b) critical coupling ($t=a$), sharp phase shift of π at resonance and (c) under-coupling ($t/a>1$). 13

1.11 (a) Simulated transmission versus wavelength for 60-μm-radius AlN, the free spectral range (FSR) and full width half maximum (FWHM) are marked. (b) Simulated variation of FSR versus microring radius. . 15

1.12 Calculated Q-factors versus the cavity loss at the over-coupling, critical coupling and under-coupling conditions. 18

1.13 Calculated ER variation versus the ratio of Q_c and Q_{int}. At critical coupling (Q_c=Q_{int}) the ER goes to maximum. 18

2.1 Schematic illustration of (a) Total internal reflection (TIR) of light in 1D waveguide. Illustration of the cross-section view of basic geometries (b) rib waveguide (c) ridge waveguide. 21

2.2 (a) Schematic illustration of cross-section our AlN waveguide. Simulated electric field distribution using finite element method (FEM) solver (b) TE mode profiles (c) TM mode profiles. 22

2.3 (a) Effective refractive index versus wavelength for the TE fundamental, first and second order modes (b) Effective refractive index versus wavelength for TM fundamental, first and second order modes. 23

2.4 Schematic illustration of the fabrication process of AlN microresonators on sapphire using standard electron beam lithography. 25

2.5 Simulated group velocity dispersion (GVD) calculations of a 60-μm-radius and 1.2 μm fully etched AlN microresonator with varying ring widths (RWs) of 1.9, 2.3, 2.6, and 3.6 μm. It depicts the GVD profiles at fundamental and higher orders (for wider RW) polarization modes. (a) TE (b) TM. 27

2.6 Process flow of microresonators dispersion calculation based on the material and geometry dispersion via finite element method (FEM). . 29

2.7 Schematic illustration of (a) microresonator resonator modes (green) and comb lines separated by an FSR of $D_1/2\pi$. ω_μ is the angular frequency at relative mode numbers μ, where ω_0 is pump frequency. (b) Integrated dispersion (D_{int}) profile where the pump position is denoted by A, B is the position with positive curvature and FSR separations is maximum and DW wave position is denoted by point C. 30

2.8 Calculated integrated dispersion (D_{int}) of a 60-μm-radius AlN microresonator with fixed height of 1.2 μm and angle of 72°.The Upper panel shows the dispersion curves of TE_{00} mode family at different widths. The Lower panel shows dispersion curves of TE_{10} mode family at different ring widths. 31

2.9 Calculated integrated dispersion (D_{int}) of a 60-μm-radius AlN microresonator with fixed height of 1.2 μm and angle of 72°. The Upper panel shows the dispersion curves of TM_{00} mode family at various ring widths. The lower panel shows dispersion curves of TM_{10} mode family at various ring widths. 32

2.10 Extracted TE and TM modes FSRs with various MRR waveguide widths using the FEM simulation. 33

2.11 Calculated integrated dispersion (D_{int}) of a 60 μm-radius AlN microresonator with fixed width of 2.3 μm and angle of 72°. The Upper panel shows the dispersion curves of TE_{00} mode family at various etching depths. The Lower panel shows dispersion curves of TM_{00} mode family at various etching depths. 33

2.12 Calculated integrated dispersion (D_{int}) of a 60-μm-radius AlN microresonator with fixed width of 2.3 μm and core height of 1.2 μm. Series of D_{int} curves are calculated for a TE_{00} mode family at various sidewall angles of 72°, 74°, 76°, 78° and 80°, respectively. 34

2.13 Schematic illustration of cross-sections of various proposed LN waveguides designs. W is LN MRR top width; H is total thickness; h is unetched thickness; θ is sidewall angle. (a) Type I is air cladded (b) Type II is SiO_2 cladded and (c) Type III is SiO_2 cladded on etched LN. 35

2.14 Calculated integrated dispersion (D_{int}) curves for 100-μm-radius LN where Type-I is curve corresponds to the air cladded design, Type-II is SiO_2 cladded and Type-III is SiO_2 cladded on etched LN. 36

3.1 (a) Schematic illustration of setup used for the Kerr soliton generation using the dual mode (1P2R) strategy. CW laser: continuous wave laser; FPC: fiber polarization controller; EDFA: erbium-doped fiber amplifier. (b) Principle of thermal compensation using the dual modes scheme. At state (i) the pump wavelength $P_{\lambda 1}$ is coupled into the main resonance (TE_{00}). When tuning the pump wavelength to $P_{\lambda 2}$ position in the state (ii) the power is coupled to both the modes and relatively red shifts. Soliton state (iii) is reached when tuning the pump to the $P_{\lambda 3}$ position i.e., the red-side of the pump resonance. The pump mode slightly blue shifts accompanied by a reduction in the cavity power which is compensated with the help of TE_{10} mode that stabilizes the soliton state. (c) Diagram of intracavity power and the evolution of different wave-forms at the different states of the DKS generation. 40

3.2 Simulated separations between two adjacent TE resonance wavelengths for an AlN MRR with the radius of 60 μm, the thickness of 1.2 μm and various RWs. 41

3.3 (a) Experimental setup used for device characterization. CW: continuous wave laser; FPC: fiber polarization controller; OSA: optical spectrum analyzer; PM: power meter. (b) Microscopic image of one of the devices used in this work. (c) Measured transmission trace of the device with TE mode polarizations. (d) Zoomed in image of the two fitted adjacent modes at around $\sim$1550 nm. 42

3.4 (a) Standard experimental setup used for DKS generation. CW: continuous wave seed laser (Santec TSL-710); FPC: fiber polarization controller; EDFA: erbium-doped fiber amplifier; OSA: optical spectrum analyzer (Yokogawa-AQ6375B); FBG: fiber Bragg grating; PM: power meter (Santec MPM-210); PD: photodiode; ESA: electric spectrum analyzer. (b) Recorded transmission trace of the two adjacent modes at 350 mW on-chip and laser sweep speed of 1 nm/s. The different color shadings on the transmission trace correspond to the soliton existence range (SER) and TE_{10} mode. (c) Microscope image of strong green light observed at the soliton state. (d) Measured optical spectra. Upper panel: MI comb, lower panel: single soliton and fitted with the $sech^2$ envelope (black dashed line). Inset is the recorded RF noise spectra of the corresponding MI (blue), single soliton (green) microcomb states and the PD noise floor (black). 44

3.5 (a) Standard experimental setup used for device transmission spectra measurements with the addition of a thermo-electric controller (TEC). Inset is the microscopic image of the coupling system. (b) Measured transmission spectra of four groups of TE resonances, between 1547.5 to 1557.5 nm wavelength range, at various temperatures. (c) Maps of the TE_{00} and TE_{10} modes in the regions (i)-(iv), in temperatures ranging from 15°C to 60°C. The TE_{00} mode is on the left in the regions (i) and (ii) whereas in (iii) and (iv) it shifts to the red side, respectively. In region (ii), the TM_{00} mode appears at temperatures above 30°C. 47

3.6 (a) Zoomed-in image of transmission spectra of TE resonances (region ii) near 1550 nm at different temperatures with a step of 5°C. (c) Upper panel: The difference of the resonance wavelength between the TE_{10} and TE_{00} modes [also the TM_{00} mode in region (ii)] at different temperatures. Lower panel: The extinction ratios (ERs) versus temperature of the modes A and B. 49

3.7 (a) Extracted loaded Q-factors of the TE_{00} and TE_{10} resonance modes versus temperatures in the region (iii), without the mode coupling effect. (b) Free spectral range (FSR) variation with temperatures, upper panel: TE_{00} polarization mode and lower panel: TE_{10} polarization mode. 49

3.8 (a) Scheme of energy flow in the integrated microresonator. (b) Resonance transmissions, at 16°C with an on-chip power of 320 mW. Upper panel: all- and pump-transmissions at the laser tuning speed of 1nm/s, lower panel: converted light (the difference between all- and pump-transmissions). Soliton access possibility with brown spheres. (c) Resonance transmissions at 28°C with an on-chip power of 280 mW. Upper panel: all- and pump-transmissions at the laser tuning speed of 1 nm/s, lower panel: converted light. Soliton access possibility with brown spheres. 51

3.9 (a) Measured optical spectra of single-soliton recorded at the TEC temperatures of 16°C and 28°C, respectively. Corresponding on-chip powers are 280 mW and 320 mW. The black dashed line shows $sech^2$ fit. (b) Zoomed-in view of the DKS comb lines and second-order diffraction lines at the lower frequency range. (c) RF noise spectra of the single-soliton and PD noise floor. 53

3.10 (a) 3D histogram showing the relationship between TEC temperature, on-chip power and soliton step (termed as soliton existence range). (b) Soliton existence range (SER) (marked green rectangles) at different temperatures. 54

3.11 (a) Measured converted light trace (difference between all- and pump-transmissions) at 29°C with an on-chip power of ∼310 mW. (b) Measured optical spectra of two-soliton microcombs. The spectra fitting (red colored) reflects the solitons relative positions circulating in the microcavity. 55

3.12 Pumping the TE_{10} mode (a) Measured spectra of breather soliton (green) at 16°C and no stable comb (red) at 28°C (b) Low-frequency RF noise spectrum corresponds to breather state. 57

3.13 (a) Zoomed-in image of transmission spectra of TM resonances (region ii) near 1550 nm at different temperatures with a step of 5°C. (b) Measured MI comb spectra, pumping TM_{00} mode in the temperature range between 16°C to 28°C. 58

3.14 (a) Zoomed-in image of the comb-lines and second-order diffraction lines at the longer wavelength. (b) Optical spectral lines of the soliton microcombs at long wavelength by tuning the laser wavelength from 1550.58 to 1550.73 nm. (c) The variation in the carrier-offset frequency (f_{ceo}) versus the laser wavelength at various temperatures. 60

4.1 (a) Experimental setup used for device characterization. CW, continuous wave laser; FPC, fiber polarization controller; OSA, optical spectrum analyzer; PM, power meter. (b) Transmission of the device with TE modes polarization. (c) Two fitted adjacent modes at around ∼1556 nm. (d) Measured FSRs and extracted Q_{load} for the TE resonances in the range 1550-1570 nm. 66

4.2 (a) Two adjacent modes of resonance transmission at 250 mW and laser sweep speed of 1 nm/s. The different color shadings on the transmission correspond to microcomb states from (i)-(iv). (b) Microcomb evolution map. (c) Measured optical-spectra.(i) Multi-FSR primary comb (ii) MI comb (iii) Breather state (iv) Breather soliton with SRS Stokes line and (v) is the stokes emissions when the laser wavelength stop position is on the TE_{10} mode. Inset of state (iv) is the zoomed-in image of the SRS Stokes and microcomb lines. (d) Recorded RF noise spectra of corresponding microcomb states (i)-(v). 67

4.3 (a) Transmission spectrum of TE polarization modes in the range 1550-1570 nm, at power of ∼ 40 μW. The three sets (i)-(iii) of pumped resonances are marked with orange, green and blue colors.(b) Transmission traces of resonances (i)-(iii) at a pump power of 250 mW (c) Measured Kerr microcomb optical spectra (range 1300-1850 nm) by pumping the TE_{00} modes of resonance wavelengths in (b). (d) Measured optical spectra of Kerr microcomb primary and/or SRS Stokes lines by pumping the TE_{10} resonance modes in (b). 70

4.4 Experimental demonstration of breather and single soliton microcombs. (a) Optical spectra of breather and single soliton microcombs at fixed power of 250 mW and various laser sweep speeds of 2, 6 and 10 nm/s.(b) Corresponding RF noise spectra. 72

4.5 Experimental demonstration of 4/5 of an octave-spanning single soliton microcomb. (a) Optical spectra of a single soliton microcomb (1200-2100 nm) at 400 mW pump power and fitted with a sech^2 black dashed line. (b) Corresponding recorded RF noise spectra of the soliton microcomb together with PD floor noise level. 73

4.6 (a) Transmission spectrum of the TE polarization mode of the second device in the range 1560 to 1568 nm at $\sim$40 μW power.(b) Measured FSRs and extracted Q_L-factors in the 1540-1575 nm range. 74

4.7 Experimental demonstration of breather and single soliton microcombs in the TE_{10} mode.(a) Measured optical spectra at 400 mW (i) primary, (ii) MI, (iii) breather soliton, and (iv) single soliton microcombs, using manual tuning. The red solid line in the lower panel (state iv) is the D_{int} simulation of the TE_{10} mode.(b) Corresponding RF noise spectra (i)-(iv) of states in (a). 75

4.8 Simulation of the TE_{10} breather and single soliton microcombs using the LLE. (a) Simulated breather (upper panel) and single soliton (lower panel) microcomb with 490 mW pump power. (b) Intracavity field evolution map (top) and intracavity power evolution (bottom) by tuning from blue to red regions. 76

4.9 Schematic illustration of breathing perfect soliton crystals. N is the maximum number of equidistant optical pulses over the circumference of the cavity. 77

4.10 (a) Transmission spectrum of the TE polarization modes in the range from 1540 to 1570 nm under $\sim$40 μW power. The right side scale is 3-dB linewidth of the TE_{00} (marked with triangle symbol) and the TE_{10} (marked with circle symbols) polarization modes.(b) Pump resonance wavelength with Lorentzian fitting.(c) Microscopic image of the 60 μm-radius AlN device. 78

4.11 Experimental measurements of breathing perfect soliton crystals.(a) Optical spectra recorded at different red-detuned laser wavelength stop positions which is presented in the top inset of (a). 5-FSR soliton crystal (lower panel) is fitted with $sech^2$, where the pump and mode interaction points are marked with red triangle and cross symbols, respectively. (b) Corresponding RF noise spectra at detuning positions (i)-(iv). 79

4.12 Pulse measurement.(a) Experimental setup used for pulse measurements using SHG-based autocorrelator (AC).(b) AC measurement results for the states (i)-(iv). 80

5.1 Scheme presenting the single soliton microcombs applications [53]. . 83

5.2 (a) Schematic of 2D cross-section parameters of the Si_3N_4 microresonator. (b) Microscopic image of the fabricated 23-μm-radius MRRS with integrated bus waveguides. (c) Simulated TE polarization resonant wavelengths for Si_3N_4 MRRs with a fixed radius of 23-μm , waveguide thickness of 0.80 μm and various RWs of 1.68-1.8 μm with the step of 20 nm. (d) Measured TE polarization transmission spectra of the 23-μm-radius MRRs with the diverse RWs (range of 1.68:0.02:1.80 μm). The target dual-modes with pump on the blue side are denoted by the dashed rectangular boxes. 86

5.3 (a) Calculated integrated dispersion via FEM-based simulations of the 23-μm Si_3N_4 MRRs with various RWs. (b) Measured optical spectra of the designed MRRs. The dashed lines indicated the mode interaction positions. Variations in the comb spectra are clear from the different RWs. 88

5.4 (a) Zoomed-in image of the two close modes. (b) Converted light (difference between the pump and all transmission) trace at a pump power of 150 mW. The soliton step, also termed SER, is marked with a green rectangle. (c) Measured optical spectrum of the single soliton. 89

5.5 Measured transmission spectrum at TE polarization mode for the device D1 at the laser wavelength range between 1480 nm to 1640 nm. The longitudinal pumped modes (marked with red rectangles) to obtain the various SCs are denoted by the relative mode numbers (μ_p) far from the mode crossing position (marked with green rectangle and denoted by the relative mode number (μ_m). Inset (i) is the calculated integrated dispersion for the TE_{00} mode as a function of relative mode numbers μ where μ_p=0 is at around 1557 nm. Inset (ii) is the zoomed-in image of the mode interaction near 1615 nm. 91

5.6 Experimental results of N=6 SCs in device D1. (a) Measured comb power at on-chip power of 255 mW. The SCs access region of 0.04 nm i.e, $\sim$ 5 GHz, is marked with a green rectangle. The red circular dots denotes the wavelength stop position to access the three comb states i.e., Primary, MI and SCs microcombs. (c) Measured optical spectra (i) Primary comb (ii) MI comb and (iii) SCs. Insets in states (ii)-(iii) of Fig. 5.6(c) are the corresponding RF spectra. (d) SCs evolution map and different comb states are marked with white dashed lines (i) Primary comb (ii) MI comb and (iii) SCs with N=6. 92

5.7 (a) Optical spectra of different octave-spanning SCs obtained in D1 at the relative pump modes μ_p= 2,1,0,-1 and the mode interaction at μ_m=-7. The symbols circle and cross denote the pump and mode interaction, respectively. (b) Measured auto-correlation traces of the obtained different SCs. 94

5.8 (a) Measured transmission spectrum of D2 at the TE polarization mode in the laser wavelength range 1480-1640 nm. The pump modes are marked with red rectangles far from the mode interaction position (marked with a green rectangle). Inset is the calculated integrated dispersion for the TE_{00} mode as a function of relative mode numbers μ at the around μ_p=0, i.e., 1548 nm. (b) Optical spectra of different SCs in device D2. The symbols circle and cross denote the pump and mode interaction, respectively. (c) Measured corresponding AC traces. 95

List of Tables

5.1 Summary of the dimensions of the employed devices D1 and D2. Obtained diverse SCs with N soliton number, pump wavelengths at the relative mode numbers and the mode interaction positions. 95

Abstract

Microresonator-based Kerr optical frequency combs exhibit a spectrum of discrete and equally spaced frequency lines. The comb source is a precise frequency ruler to measure time and distance to extraordinary precision and therefore has been a hot topic of research for more than a decade. Since the discovery in 2007, a monolithic microresonator-based Kerr frequency comb (microcomb hereafter) generated via parametric four-wave mixing using a continuous-wave pump laser, emerged as an alternative scheme to large-scale fiber-based comb sources. Microresonators have attracted considerable interest due to miniaturization, chip-scale integration of pump and cavity, and spectral coverage from the visible to the mid-infrared.

In recent years, the demonstration of novel dissipative Kerr solitons (DKS) in a microresonator was a tremendous breakthrough and revolutionized the field of microcomb technology because of the strong coherence, low noise (mode-locking), high stability, and broad spectral bandwidth of the soliton state. The Kerr solitons in a high-Q microcavity can be accessed under two crucial conditions. The first condition maintains the pulse shape with the balance between the dispersion and Kerr nonlinearity. The second condition that maintains the soliton is the loss in the cavity is compensated by the nonlinear parametric gain through the driving continuous wave laser. These prominent characteristics and a spectral width of an octave-spanning comb enable stable measurement of the comb via the self-referencing technique. This makes it an extraordinary candidate for monolithic integration in many commercial applications, particularly for timing and precision measurements.

In this thesis, we thoroughly investigate the nonlinear dynamics in aluminum nitride (AlN) and silicon nitride (Si_3N_4) microresonators especially the microcomb generation and the soliton access. In particular, we proposed a reliable, universal scheme named dual-mode microresonators to access octave-spanning soliton microcombs,

which is comparatively straightforward and cost-effective. With this method, we for the first time experimentally demonstrated a stable single-soliton (f_{rep}, 374 GHz) in an AlN microresonator with an octave-spanning (1100-2300 nm) comb owing to the engineered dispersion. Our highlight is the broad soliton existence range (SER, 10.4 GHz), which is 7 times greater than recently reported. This is quite useful for long-term stabilization thus enabling applications outside the laboratory, such as communication and LiDAR. In addition, with the aid of an external temperature controller, we successfully control the mode coupling, further extend the SER to 16 GHz and can reduce the carrier offset frequency (f_{ceo}) from ∼40 to ∼30 GHz with a decrease in temperature. The temperature controller can also be used to enrich the soliton dynamics, i.e., various two solitons state in this case. Thirdly, different soliton behavior such as the breather solitons and near-octave spanning soliton crystals were also experimentally observed in other dual-mode AlN devices due to the interaction of the two transverse mode families. Lastly, we confirm the robustness of the above-mentioned scheme in dual-mode Si_3N_4 microresonators with a fixed radius and obtained state-of-the-art results: single-soliton (f_{rep}, 1 THz) and various perfect soliton crystals (N= 4, 5, 6, 7, 8) with octave-spanning ranges. These solitons can be easily reached with a slow pump tuning rate. More importantly, the measurement results including the mode separation and dispersion agree with our simulation results very well. This indicates that such dual-mode microresonators can be designed and demonstrated with different material platforms.

Keywords: Microresonators, Kerr optical frequency combs, dual-modes scheme, dissipative Kerr-solitons, breather solitons, perfect soliton crystals.

Publications

1. H. Weng, **A. Afridi**, J. Liu, J. Li, J. Dai, X. Ma, Y. Zhang, Q. Lu, W. Guo, and J. Donegan, "Near-octave-spanning breathing soliton crystal in an AlN microresonator," Opt. Lett. 46, 3436-3439 (2021).

2. H. Weng, J. Liu, **A. Afridi**, J. Li, J. Dai, X. Ma, Y. Zhang, Q. Lu, J. Donegan, and W. Guo, "Directly accessing octave-spanning dissipative Kerr soliton frequency combs in an AlN microresonator," Photon. Res. 9, 1351-1357 (2021).

3. **A. Afridi**, H. Weng, J. Li, J. Liu, M. McDermott, Q. Lu, W. Guo, and J. Donegan, "Breather solitons in AlN microresonators," Opt. Cont. 1, 42-50 (2022).

4. H. Weng, **A. Afridi**, J. Li, M. McDermott, H. Tu, L. P. Barry, Q. Lu, W. Guo, and J. Donegan, "Dual-mode microresonators as straightforward access to octave-spanning dissipative Kerr solitons", APL Photon. 7, 066103 (2022).

5. **A. Afridi**, H. Weng, J. Li, R. McKenna, M. McDermott, H. Tu, Q. Lu, W. Guo, and J. Donegan, "Effect of Thermal Tuning and Mode Coupling On Soliton Microcombs in AlN Microresonators," IEEE Journal of Selected Topics in Quantum Electronics (2022), doi: 10.1109/JSTQE.2022.3196124.

Other contributions not included in the thesis work

1. J. Liu, H. Weng, **A. Afridi**, J. Li, J. Dai, X. Ma, H. Long, Y. Zhang, Q. Lu, J. Donegan, and W. Guo, "Photolithography allows high-Q AlN microresonators for near octave-spanning frequency comb and harmonic generation," Opt. Exp. 28, 19270-19280 (2020).

2. H. Weng, J. Liu, **A. Afridi**, J. Li, J. Dai, X. Ma, Y. Zhang, Q. Lu, J. Donegan, and W. Guo, "Octave-spanning Kerr frequency comb generation with stimulated Raman scattering in an AlN microresonator," Opt. Lett. 46, 540-543 (2021).

Conferences contribution

1. "Breather soliton observation in AlN microresonators" Poster presentation, Photonics Ireland (2021).

2. "Ultra-wide soliton access window in an AlN microresonator " Poster presentation, Conference on Lasers and Electro-Optics (CLEO), San Jose, USA, (2022).

3. "Ultra-wide soliton access window in an AlN microresonator " Poster presentation, MICROCOMB22, Switzerland (2022).

Chapter 1

Introduction

The technology of optical frequency combs (OFCs) and the development of laser-based precision spectroscopy were developed by John L. Hall and Theodor W. Hänsch and were awarded half of the 2005 physics Nobel prize for their significant achievement [1]. Traditional femtosecond OFCs sources include mode-locked Ti-sapphire and erbium-doped fibre lasers [2][3]. The mode-locked lasers are optical cavities that comprise of a gain medium and a saturable absorber. In the mode-locked laser, the gain medium oscillates with longitudinal cavity modes corresponding to the gain bandwidth and the saturable absorber produces the pulsed operation [4]. As shown in Fig. 1.1(a), a train of stable short pulses are emitted in the time domain by the mode-locked lasers with the pulse period equal to the cavity length. A phase shift ($\Delta\phi$) occurs in the field of one pulse to the next due to the difference in the group and phase velocities. In the frequency domain, the train of pulses can be represented as equidistant lines resembling a comb structure and thus named as frequency comb, shown in Fig. 1.1(b). The carrier offset frequency (f_{ceo}) in the frequency domain is related to the phase shift ($\Delta\phi$) and its stabilization [5] paved the way for various significant applications such as an optical frequency synthesizer [6], atomic clock [7] and molecular fingerprinting [8], etc. The conventional mode-locked laser-based OFC sources are bulky, with high power consumption, low stability and low repetition rates. Later microresonators-based OFCs were developed and delivered a significant breakthrough in nonlinear photonics research. In 2007, the first OFCs were demonstrated in a 75 μm diameter silica based microresonator [9]. These microresonators-based OFCs are of much interest due to

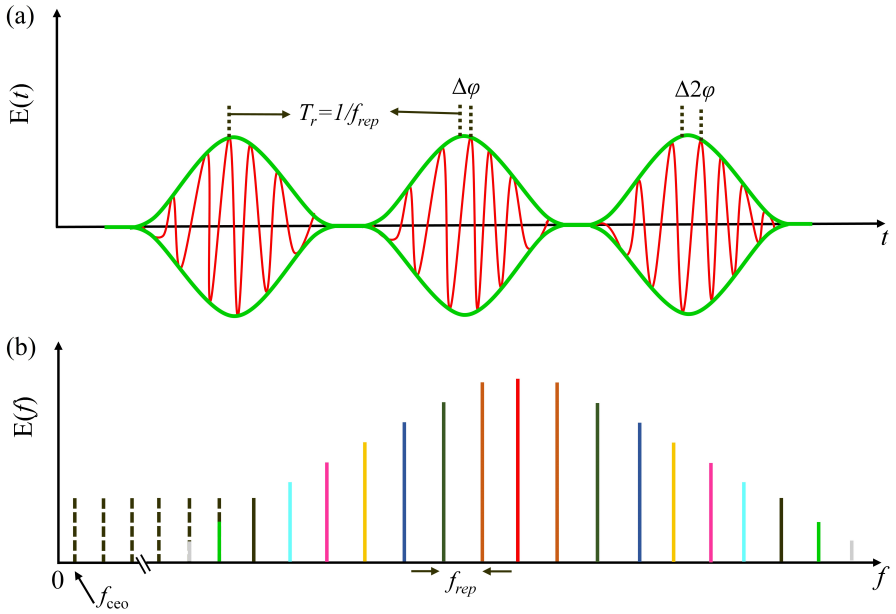


Figure 1.1: (a) Pulse train in conventional mode-locked laser. The cavity round-trip time is T_R and $\Delta\phi$ is pulse envelope phase shift due to the difference in group and phase velocities. (b) An optical spectrum in the frequency domain corresponding to (a), the spectrum consists of discrete equidistant comb lines with frequency repetition rate f_{rep} and offset frequency f_{ceo}.

the reduced size, simplicity and low power consumption compared to femtosecond mode-locked lasers. Another key merit that attracted researchers and scientists is its compatibility with the complementary metal-oxide-semiconductor (CMOS) fabrication process and on-chip integration. This made large-scale fabrication feasible for many industrial and commercial applications.

1.1 Microresonators based optical frequency combs

In microresonators, a continuous wave (CW) laser is the source for generating the frequency combs by pumping light into the dielectric microcavity. The pumped light is confined in the cavity of a small volume and exploits various nonlinear processes for comb generation. The nonlinear processes in the microcavities can be expressed by the time-dependent polarization induced in the nonlinear medium in the presence of an applied electric field [10]

$$P(t) = \varepsilon_o(\chi^1 E(t) + \chi^2 E(t)^2 + \chi^3 E(t)^3 + ...) \tag{1.1}$$

where χ^n, n=1,2,3... are the terms in the optical susceptibility. Depending on the symmetry of the microresonator material, the nonlinear effects such as second-(χ^2) and third-order (χ^3) are exploited. The χ^2 processes include the second harmonics generation (SHG), sum/difference frequency generation (SFG/DFG), schematically illustrated in Fig. 1.2(a). Another second-order nonlinear process is the electric-optic effect (EO) Pockels effect, which induces a modification in the refractive index due to the parametric mixing of an external optical field. The χ^3 non-linearity effects/phenomena include third harmonic generation (THG), self-phase modulation (SPM), cross-phase modulation (XPM) and four-wave mixing (FWM), schematically illustrated in Fig. 1.2(b). The confined light in the microcavity excites the

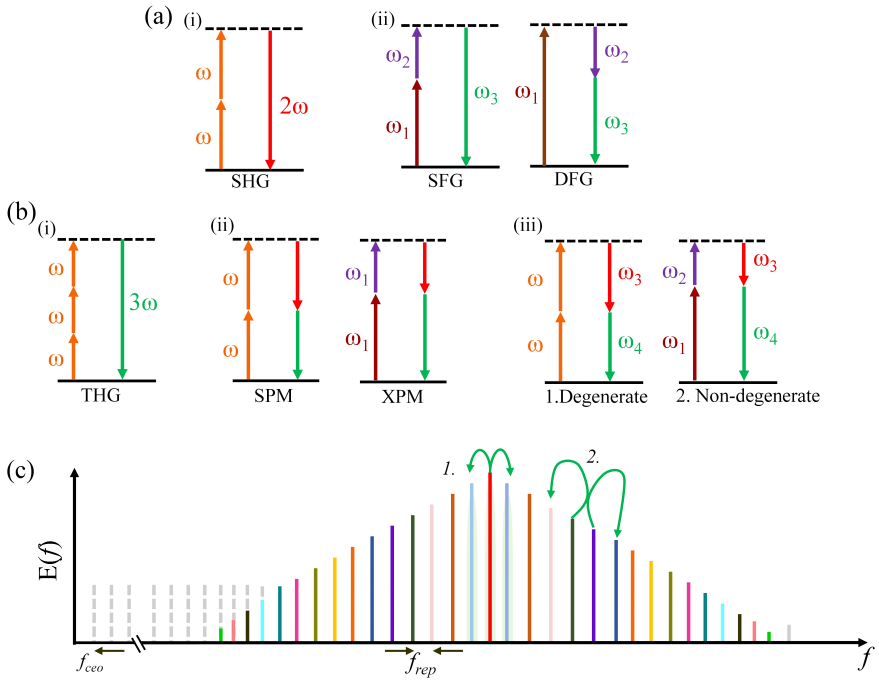


Figure 1.2: Schematic illustration of the χ^2 and χ^3 nonlinear parametric process: (a) (i) Second harmonic generation (SHG), where two pump photons generate a new photon with twice the frequencies of the pump ($\omega+\omega=2\omega$). (ii) Sum/difference frequency generation (SFG/DFG), here a new photon is generated with the frequency equal to the sum/difference of the input ($\omega_3=\omega_1\pm\omega_2$). (b) (i) Third harmonic generation (THG), is a nonlinear process where a new photon has triple the frequency of the pump($3\omega=\omega+\omega+\omega$). (ii) Self- (SPM) and Cross-phase modulations (XPM), in SPM process the intensity of the propagating field induces a modification in the refractive index and in the XPM the co-propagating fields induce modification of the refractive index. (iii) Degenerate FWM is the parametric process where two photons with the same frequencies generate two new photons ($2\omega_1=\omega_2+\omega_3$). In non-degenerate FWM, the two photons are annihilated and two new photons are generated, satisfying an energy conservation ($\omega_1+\omega_2=\omega_3+\omega_4$). (c) Microresonator-based optical frequency comb spectrum via cascaded FWM processes 1 and 2.

modes of the microring due to the strong light-matter interaction. Among the various non-linear processes, as defined above, the χ^3 Kerr non-linearity FWM process initiates the frequency comb and is thus named the Kerr frequency comb. The microcomb first side-bands are generated via a degenerate four-wave mixing (FWM), indicated in Fig. 1.2(c) (process 1). Where two pump photons with the same angular frequencies (ω) are annihilated and create two new photons on the side-bands with the frequency up-shift known as signal (ω_3) and frequency downshift known as idler (ω_4). The signal and idler side bands can enhance the process of creation by the multiple side-band generation if their modes coincide with microresonator modes as shown in Fig. 1.2(c) (process 2). The side-bands generated by the FWM are multiple FSR and equidistant. For a cascaded process, non-degenerate FWM processes are significant in achieving the broadband frequency comb with the discrete and equidistant spectral lines in the frequency domain. In the non-degenerate process, two idler and/or signal photons serve as pump photons and produce two new photons of different frequencies. The process is termed non-degenerate as the frequencies of all four photons are different. Both degenerate and non-degenerate FWM leads to cascaded FWM and the comb spectrum contains discrete, equidistant comb lines. The broadening of the comb is limited by the microresonator dispersion which will later be discussed in chapter 2. To some extent, one can overcome the difference between the comb lines and cavity modes by increasing the pump power to pull the modes, via SPM and XPM, resulting in the mode-locking of the comb lines for the broad comb generation.

1.1.1 An octave-span microcomb

To stabilize the microresonator frequency comb and detect the off-set frequency (f_{ceo}) it is essential to reach an octave-span bandwidth. An octave-span covers the spectrum of comb lines from n to 2n range and f_{ceo} can be detected using the self-referencing f-2f scheme [2][11]. In this scheme, f_n=nf_{rep}+f_{ceo} and f_{2n}=2nf_{rep}+f_{ceo} are the comb lines at the shorter and longer sides of the spectrum, as shown in Fig. 1.3. The lower frequency f_n is doubled using a crystal with χ^2 non-linearity and transfers the original frequency to $2f_n$. The beat note of $2f_n$ and f_{2n} will provide the f_{ceo} and

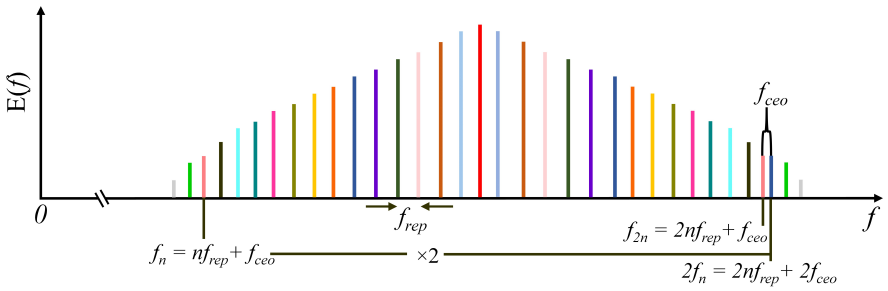


Figure 1.3: Schematic illustration of f-2f self-reference scheme in an octave-span spectrum. In this scheme, f_n and f_{2n} are the frequencies at the lower and higher end of the spectrum. The lower frequency f_n is doubled via SHG. The beat note of $2f_n$ and f_{2n} can provide the f_{ceo}.

calculated as

$$f_{ceo} = 2f_n - f_{2n} = 2nf_{rep} + 2f_{ceo} - 2nf_{rep} - f_{ceo} \tag{1.2}$$

It was a breakthrough in optical frequency comb technology to reach an octave-span using a microresonator compared to the traditional femtosecond laser comb [12][13]. This enabled the technology for many potential applications such as spectroscopy [2], optical clock [14] and frequency synthesizer [15], etc.

1.1.2 Dissipative Kerr solitons (DKSs)

The solitons are the mode-locked state of optical microcombs. The soliton microcombs feature unique characteristics such as low noise, strong coherence and can stably last for a long period of time. In high-Q microcavities, stable solitons can be accessed by the double balance between the cavity dispersion counterbalanced by the Kerr non-linearity as well as cavity losses counterbalanced by the parametric gain, as shown in Fig. 1.4. The solitons in the cavity attain a smooth coherent pulse shape without any perturbation. The first two terms (dispersion and Kerr non-linearity) are related to the pulse duration where dispersion limits the duration which is balanced by Kerr non-linearities. The second two terms (loss and gain) are related to the pulse energy where cavity losses are compensated by the parametric Kerr FWM process gain, driven by CW laser-thus named dissipative Kerr solitons (DKSs). Furthermore, the strikingly broadening of the DKSs spectrum width due to soliton-induced Cherenkov radiation has made remarkable advancement in micro-

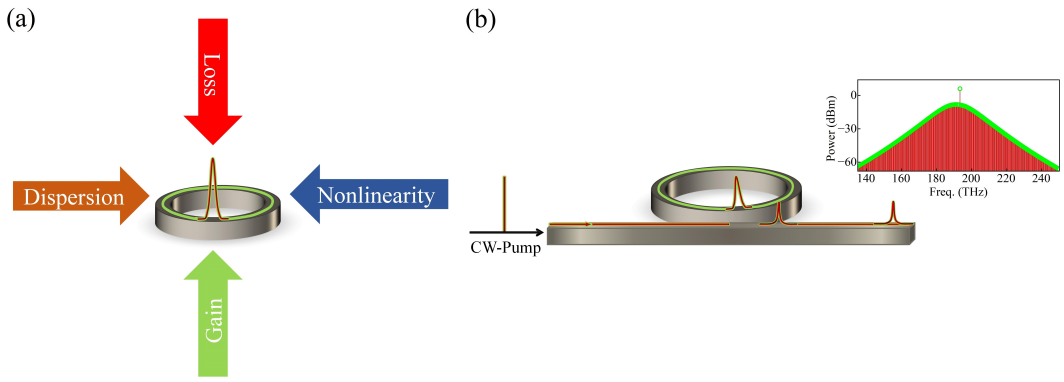


Figure 1.4: Schematic illustration of dissipative Kerr solitons (DKSs) generation (a) Sketch of effects, such as dispersion balanced by Kerr non-linearity and loss balanced by the gain to maintain the single soliton state. (b) Single soliton in the microresonator cavity and the obtained spectrum at the output.

comb technology [16]. Consequently, DKSs have been realized in a growing number of platforms including crystalline ultra-high Q MgF_2 [17], silica [18][19], and integrated platforms such as Si_3N_4 [20][21][22], AlGaAs [23], $LiNbO_3$ [24][25], SiC[26], AlN [27][28], Ta_2O_5 [29], and GaN [30].

1.2 Mircoresonator theory

Microring resonators consist of resonant cavities formed by the closed loop of the waveguide. The closed loop of the waveguide can be designed in the form of a ring or racetrack of 10's micron in size, the microresonator theoretical sketch is shown in Fig. 1.5. To confine the light in the microring, single or multiple bus waveguides use evanescent coupling to one or two sides of the ring. The coupling of the bus waveguide with the ring can be a lateral or vertical coupling. In lateral coupling, the straight waveguide is placed horizontally in the same plane whereas in vertical coupling the microring is placed on top of the straight waveguide. Lateral coupling of the bus waveguide to the ring is preferred due to ease of desired design parameters control in fabrication and at resonance significantly enhances the material nonlinear properties [31]. The lateral configuration with one coupled waveguide is known as an all-pass. In this work, we focused on the all-pass lateral waveguide configuration of the microresonators.

In all-pass microresonators, light is coupled in the integrated bus waveguide from

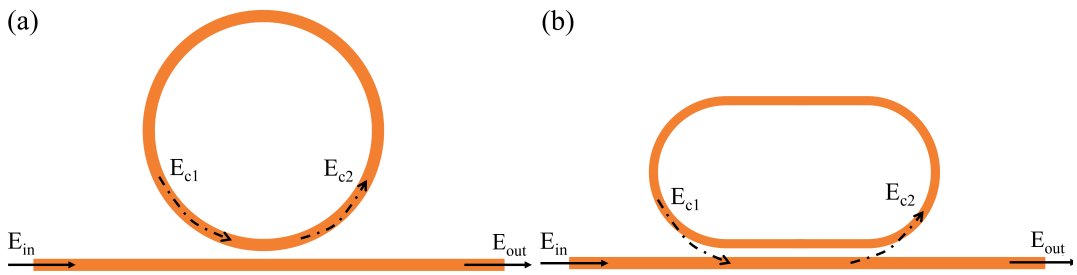


Figure 1.5: Sketch of all-pass microresonators with an integrated straight waveguide (a) circular microcavity and (b) racetrack microcavity.

one input end and is coupled into the microring cavity because of evanescent coupling where the light starts to circulate in the cavity. The coupling of light into the microring occurs in the region where there is the proximity between the bus waveguide and the microring whereas the remainder of the light passes through the output of the bus waveguide. The coupling strength is controlled by the gap between the waveguide and the microring at the coupling region. The intensity in the cavity increases as the light coupled into the straight waveguide interferes with the light in the microring at the coupling region with the phase difference of 2π i.e. constructive interference and the cavity is on resonance. In other words, one can say the cavity satisfies the resonance condition if βL=2πm, where β is the propagation constant, L is the effective length of the cavity and m is the mode number. The light coupled into the cavity will constructively interfere when the optical circumference of the cavity is an integer multiple of the input wavelength (λ), i.e. n_{eff}L=m.λ (effective refractive index n_{eff}= cβ/ω, L is effective length of cavity). The light at the out of the all-pass microresonator is due to the destructive interference at the coupling region of the microcavity and when the phase difference between the two evanescent fields is π that results in the light at the output in the form of the transmission spectrum.

From the all-pass microresonator sketch, as shown in Fig. 1.6, the external input electric field is E_{in} and can be written as E_{in}=$E_{in}e^{-i\omega t}$ where ω is the angular frequency. The input light is coupled into the microring near the coupling region i.e., E_{c2}. The coupled light stays in the cavity whereas E_{c1} is the fraction of light coupled out of the cavity in the coupling region. Before reaching the cavity coupling region, the amplitude of the circulating light at each round cycle is reduced by a=

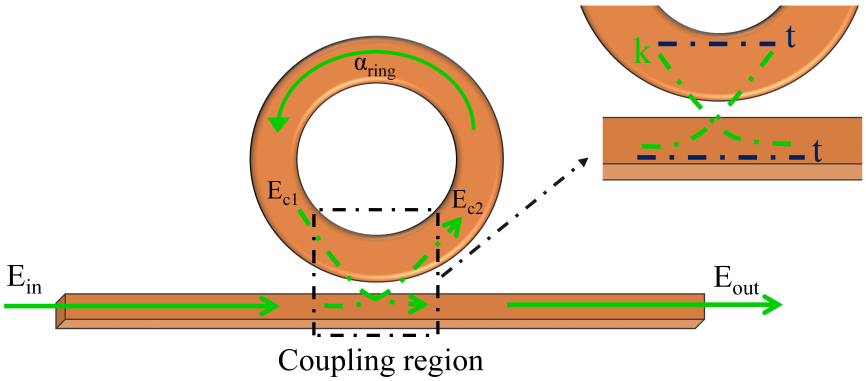


Figure 1.6: Schematic model of an all-pass microresonator with the zoomed-in sketch of the coupling region. In the coupling region, k and t are the coupling and transmission coefficients whereas E_{c2} and E_{c1} are the fields coupling into and out of the microcavity. The input and output fields are E_{in} and E_{out} as well as α_{ring} is the amplitude of cavity intrinsic losses per around-trip, respectively.

$e^{-\alpha_{ring}L/2}$ and has a corresponding build-up phase shift. The propagation losses (α_{ring}) in the cavity per length L that affect the circulating light are due to the sidewall roughness, scattering losses and material absorption. E_{out} is the fraction of light coupled out of the microring into the bus waveguide and collected at the output. From the zoom-in image of the coupling region, t and k are the transmission- and cross-coupling coefficients. The transmission coefficient is the ratio of the input and output fields on each pass and is also known as coupling strength. The cross-coupling coefficient is the fields in the cavity before and after the coupling region i.e., E_{c2} and E_{c1}, respectively.

Furthermore, the microresonator performance depends on the coupling strength (t) and the intrinsic cavity loss amplitude (a) per cycle. The coupling state is over-coupling (t$<a$) when the intrinsic cavity losses are less than external coupling strength losses. In the over-coupling regime, the coupling gap between the waveguide and microring is small. The coupling state is critical (t$=a$), when the external coupling and intrinsic cavity losses are equal. It is the desired coupling state in microresonators, where an intracavity power is a maximum. Finally, the coupling state is under-coupled (t$>a$), when the intrinsic cavity loss is larger than the external coupling strength. The coupling between the waveguide and the microring is weak. The under-coupled condition occurs when the gap between the waveguide and the microring is large.

1.2.1 Transmission and Enhancement factors

An optical microresonator is characterized by measuring some of the following significant parameters such as transmission spectrum (T), enhancement factor (B) and quality factor (Q). The transmission spectrum is the ratio of the transmitted power to the input power at a particular frequency. We start by mathematically deriving the microresonator transmission expression using coupled mode equations. As shown in Fig. 1.6, a typical model of an all-pass microresonator is used, with an input laser light E_{in} and output light as E_{out}. E_{c1} and E_{c2} are the light coupling into the straight waveguide and out of the waveguide to the microcavity whereas t and k are the self- and cross-coupling coefficients, assuming zero coupling losses and therefore satisfying the relation $|t|^2+ |k|^2=1$. Considering zero reflections the microresonator output field can be written in matrix equation as [31][32]

$$\begin{bmatrix} E_{c2} \\ E_{out} \end{bmatrix} = \begin{bmatrix} t & e^{i\pi/2}k \\ e^{i\pi/2}k & t \end{bmatrix} \begin{bmatrix} E_{c1} \\ E_{in} \end{bmatrix} \tag{1.3}$$

after the field in the cavity one round cycle, E_{c1} can be expressed as

$$E_{c1} = e^{-i\alpha_{ring}L/2}e^{i\beta L}E_{c2} = ae^{i\phi}E_{c2} \tag{1.4}$$

where a is the fraction of cavity field amplitude after one round cycle and ϕ is the associated phase change, ϕ=βL= $2\pi n_{eff}$/L. The input amplitude of the field into the microring at the coupling region and the field at the throughput can be written as

$$E_{c2} = tE_{c1} + e^{i\pi/2}kE_{in} \tag{1.5}$$

$$E_{out} = e^{i\pi/2}kE_{c1} + tE_{in} \tag{1.6}$$

using eq. (1.4) in (1.5) and (1.6)

$$E_{c2} = e^{i\pi/2}kE_{in} + tae^{i\phi}E_{c2} \tag{1.7}$$

$$E_{out} = tE_{in} + ae^{i\phi}e^{i\pi/2}kE_{c2} \tag{1.8}$$

from eq. (1.7), we can write as

$$E_{in} = \frac{E_{c2} - tae^{i\phi}E_{c2}}{ke^{i\pi/2}} \tag{1.9}$$

using eq.(1.9) we can write eq. (1.8) as

$$E_{out} = \frac{tE_{c2} - t^2ae^{i\phi}E_{c2}}{ke^{i\pi/2}} + ae^{i\phi}e^{i\pi/2}kE_{c2} \tag{1.10}$$

$$E_{out} = \frac{tE_{c2} - t^2ae^{i\phi}E_{c2} - ak^2e^{i\phi}E_{c2}}{ke^{i\pi/2}} \tag{1.11}$$

$$E_{out} = \frac{tE_{c2} - ae^{i\phi}E_{c2}}{ke^{i\pi/2}} \tag{1.12}$$

Solving equations (1.9) and (1.12), the ratio between the output field and the input field amplitudes can be written as

$$\frac{E_{out}}{E_{in}} = \frac{t - ae^{i\phi}}{1 - ate^{i\phi}} \tag{1.13}$$

so the power transfer coefficient i.e., microresonator transmission at throughput can be obtained as [33][32]

$$T = \mid \frac{E_{out}}{E_{in}} \mid^2 = \frac{t^2 + a^2 - 2at\cos\phi}{1 + a^2t^2 - 2at\cos\phi} \tag{1.14}$$

Similarly, the ratio between the circulating optical field and the input field amplitudes can be written as

$$\frac{E_{c1}}{E_{in}} = \frac{ake^{i\phi}}{1 - ate^{i\phi}} \tag{1.15}$$

Thus, an intracavity intensity buildup factor can be derived as

$$B = \mid \frac{E_{c1}}{E_{in}} \mid^2 = \frac{(1 - t^2)a^2}{1 + a^2t^2 - 2at\cos\phi} \tag{1.16}$$

Assuming a 60-μm radius microring and cavity loss attenuation coefficient (α_{ring}) equal to 1 dB/cm. Using equations (1.14) and (1.16), we calculate the variation of transmission (T) and cavity buildup factor (B) versus the ratio of t and a. As shown in Fig. 1.7, at the critical coupling condition (t=a), the transmission goes

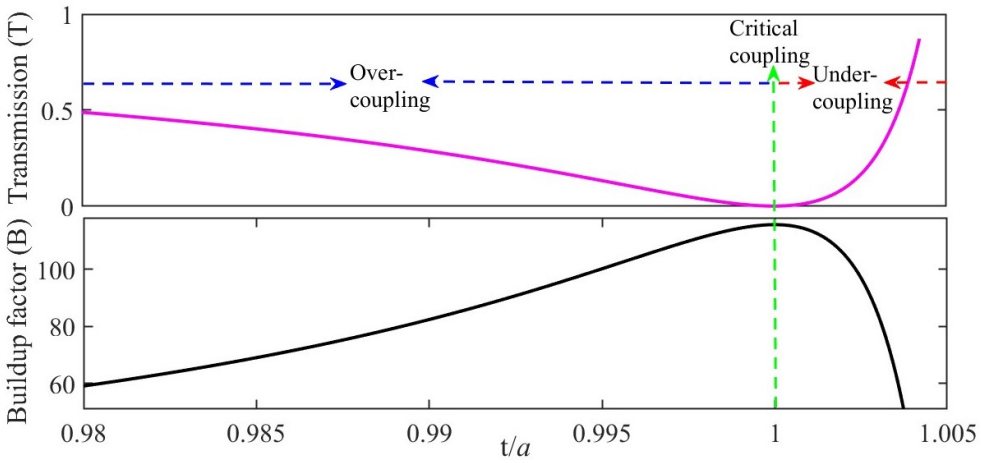


Figure 1.7: Calculated transmission and enhancement factors versus t/a ratio for a 60-μm-radius AlN microresonator.

to zero and the cavity build-up factor is maximum. This gives an understanding that the amplitude of the field coupled into the microcavity is balancing the loss of microcavity field amplitude per round trip. As a result, the light is perfectly coupled into the microcavity with zero transmission at throughput and attains maximum cavity build-up factor. For an over-coupling condition (t$<a$), the cavity transmission decreases whereas significant enhancement in the build-up factor with the increment of t. For the case of an under-coupling (t$>a$), there is a rapid decrease in the transmission and cavity build-up factor with the increase in the t. The field coupling into the cavity is less than the intrinsic cavity losses. Therefore, from the above analysis, the self-coupling coefficient t and the cavity round trip field amplitude (a) are significant parameters in the microresonator performance. For an efficient nonlinear effect, a significant improvement in the t and a can be achieved by careful optimization of the integrated bus waveguide gap and the fabrication process to reduce the cavity losses, respectively.

Furthermore, we study the response of the transmission intensity (T) at the three different coupling conditions of the microresonator in the wavelength range of 1547-1556 nm and plotted in Fig. 1.8. When t=a (critical coupling), we see that at the resonance wavelength the transmission is zero and the spectrum shows a narrow linewidth (which will be explained in the later sections). For the cases, t$<a$ (over-coupling) and t$>a$ (under-coupling), the applied field reaches the output with an undesired microresonator response.

Similarly, the response of cavity build-up factor (B) in the wavelength range of

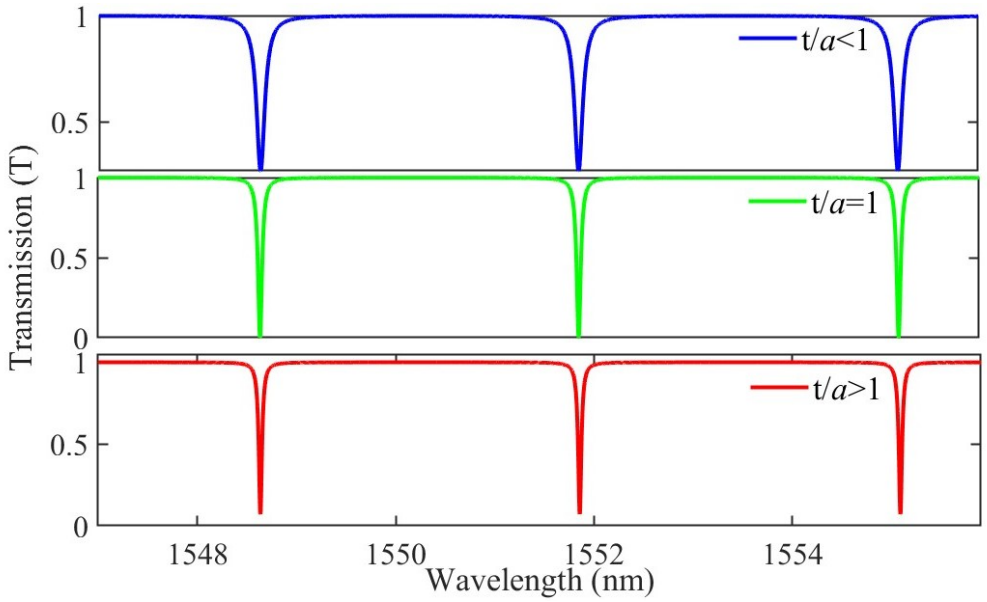


Figure 1.8: Transmissions spectra versus wavelength in over-coupling (t/a<1), critical coupling (t=a) and under-coupling (t/a>1) conditions.

1547-1556 nm is shown in Fig. 1.9. For the case of t=a (critical condition), we see maximum cavity power enhancement compared to t<a (over-coupling) and t<a (under-coupling).

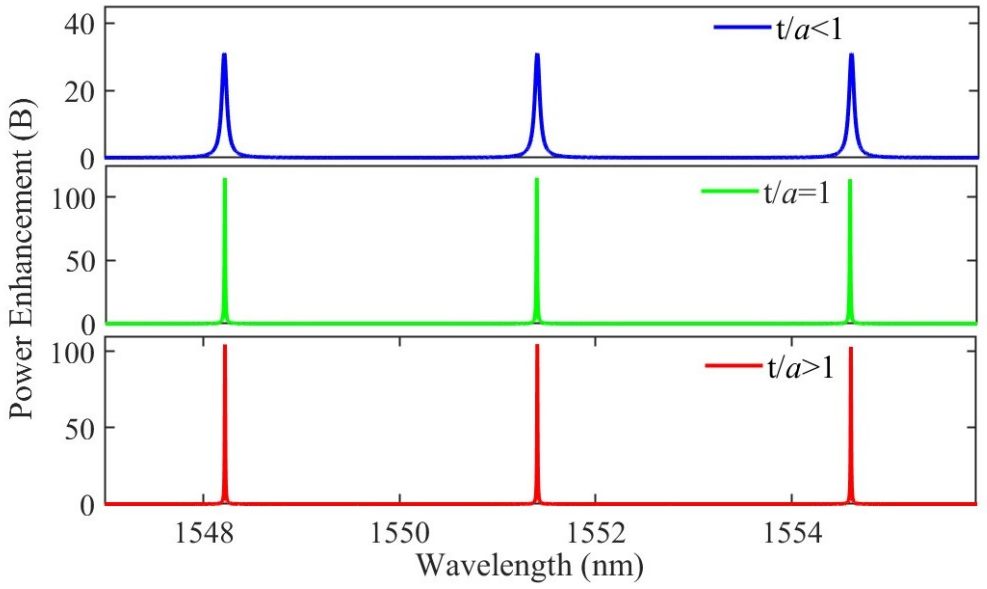


Figure 1.9: Power enhancement (B) spectra versus wavelength in over-coupling (t/a<1), critical coupling (t=a) and under-coupling (t/a>1) conditions.

Phase shift

The phase shift at the resonance wavelengths can be obtained by taking the ratio between the amplitude of the field of microring at the output to the input light field. The phase shift at the throughput can be written as

$$\Theta = arg\left(\frac{E_{out}}{E_{in}}\right) = arg\left(\frac{t - ae^{i\phi}}{1 - ate^{i\phi}}\right) \tag{1.17}$$

Figure 1.10 illustrates the phase shift (Θ) of the output field as a function of wavelength at the three different coupling conditions. In the case of over-coupling (t=0.95a) the phase shift is continuous and at the resonance a shift of 2π is achieved. For critical coupling (t=a), an abrupt phase shift between the input and output field occurs on the resonance and is equal to π. Whereas, an under-coupling (t=1.002a) condition has a negligible phase shift off-resonance and a sharp phase shift of less than π occurs on the resonant mode.

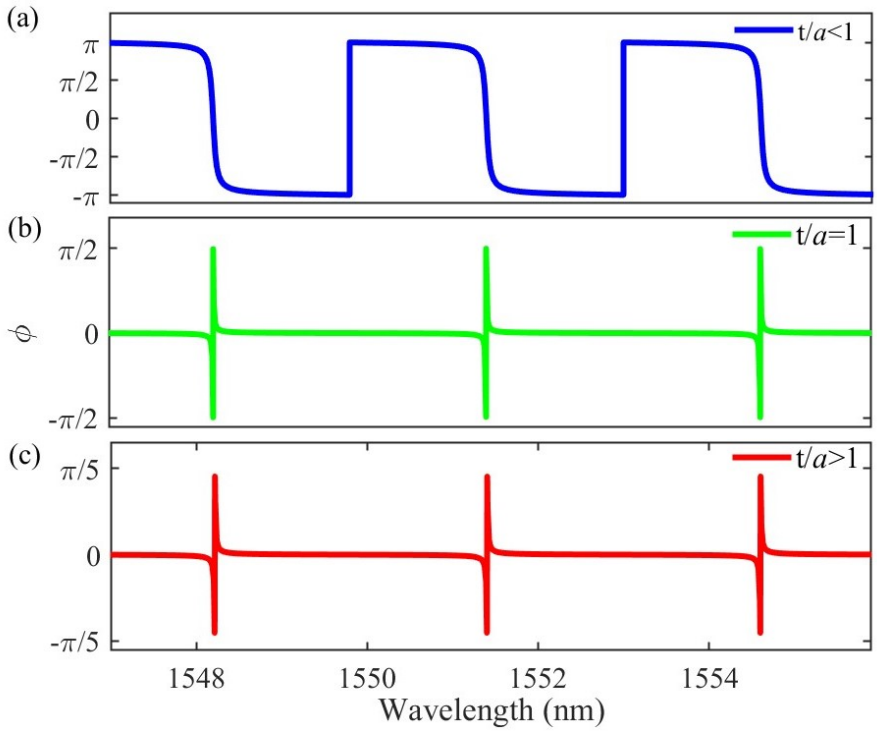


Figure 1.10: Calculated phase shifts (a) over-coupling (t/a<1), a continuous phase shift of 2π (b) critical coupling (t=a), sharp phase shift of π at resonance and (c) under-coupling (t/a>1).

1.2.2 Free spectral range (FSR)

The separation between the adjacent resonance modes (same family) in the transmission spectrum is defined as a free spectral range (FSR), as shown in Fig. 1.11(a). It is also defined as inversely proportional to the cavity round trip time. The microresonator FSR can be theoretically calculated for the cavity satisfying the resonance condition i.e., an optical path length of a cavity is an integer multiple of wavelength (n_{eff}/L=mλ). We can write FSR in terms of frequency as

$$n_{eff}L = \frac{mc}{f_m} \tag{1.18}$$

$$f_m n_{eff} = \frac{mc}{L} \tag{1.19}$$

from the definition, the FSR is the difference between the adjacent longitudinal modes (m) and (m+1), respectively. The FSR can be derived as

$$FSR = \Delta f_m = f_{m+1} - f_m \tag{1.20}$$

$$\Delta f = \left(n_{eff} + \frac{f \partial n_{eff}}{\partial f} \right) = \frac{c}{L} \tag{1.21}$$

where n_g=f n_{neff}+f ∂ n_{eff}/f is a group velocity and equation (1.21) becomes

$$FSR_f = \Delta f = \frac{c}{n_g L} \tag{1.22}$$

The FSR can be related in terms of wavelength as

$$FSR_\lambda = \Delta\lambda = \frac{\lambda^2}{n_g L} \tag{1.23}$$

Furthermore, for a circular cavity the circumference of the optical path L is 2πR. The FSR can be expressed as

$$FSR_\lambda = \Delta\lambda = \frac{\lambda^2}{n_g 2\pi R} \tag{1.24}$$

From equation (1.24) the cavity FSR is dependent on the radius and the refractive index. An increase in the radius will decrease the cavity FSR as shown in Fig.

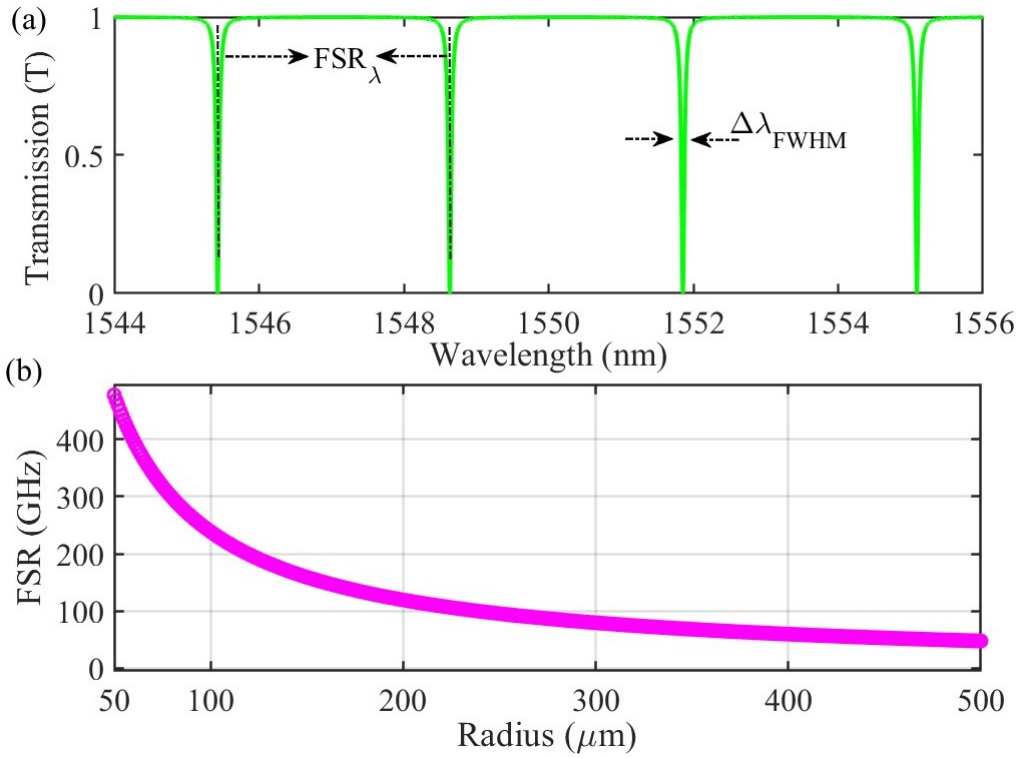


Figure 1.11: (a) Simulated transmission versus wavelength for 60-μm-radius AlN, the free spectral range (FSR) and full width half maximum (FWHM) are marked. (b) Simulated variation of FSR versus microring radius.

1.11(b). A significant parameter in the transmission curve related to the microcavity performance is the full-width half maximum (FWHM). The FWHM is obtained at the resonance mode peak as shown in Fig. 1.11(a). At each periodic resonance, it satisfies the resonance condition i.e., $\phi_R = 2\pi$N, and the power enhancement is maximum. The FWHM is half of the maximum power enhancement, using eq. (1.16) we can write

$$\frac{(1-t^2)a^2}{1+a^2t^2-2at\cos\phi} = \frac{(1-t^2)a^2}{2(1+a^2t^2-2at)} \tag{1.25}$$

$$cos(\phi) = \frac{1+a^2t^2-4at}{-2at} \tag{1.26}$$

At the resonance, we can expand the cosϕ in Taylor series by ignoring the higher-order terms

$$cos(\phi) = 1 - \frac{\Delta\phi^2}{2} \tag{1.27}$$

solving equation (1.25) and (1.26)

$$\Delta\phi = \frac{(1-at)}{\sqrt{at}} \tag{1.28}$$

As we know, at the resonance condition $\phi = 2\pi \mathrm{n}_{eff}/\lambda$

$$\Delta\phi = \frac{2\pi L}{\lambda^2} n_g \Delta\lambda \tag{1.29}$$

Using eqs. (1.28) and (1.29), we can derive $\Delta\lambda$

$$\Delta\lambda = \frac{\lambda^2}{2\pi L n_g} \frac{(1-at)}{\sqrt{at}} \tag{1.30}$$

$$\Delta\lambda = \frac{FSR_{(\lambda)}}{2\pi} \frac{(1-at)}{\sqrt{at}} \tag{1.31}$$

Finally, FWHM can be written as, $\Delta\lambda_{FWHM} = 2.\Delta\lambda$, eq. (1.31) can be written as

$$\Delta\lambda_{FWHM} = \frac{FSR_{(\lambda)}}{\pi} \frac{(1-at)}{\sqrt{at}} \tag{1.32}$$

1.2.3 Quality factor (Q) and extinction ratio (ER)

The Quality factor (Q-factor) is a very crucial parameter used to characterize the optical microresonators. The Q-factor determines the sharpness of the resonances and is defined as the ratio of the energy stored by the system to the energy reduced by the system in one round trip and is called the loaded quality factor (Q_L). The Q-factors determine the ability of the resonator to confine the light field. When the input field is coupled into the microcavity, the energy losses associated to the coupled microresonator are in two parts, one is the transmission loss of light solely in the microcavity (including material absorption, microcavity scattering loss, etc.) and the other is the coupling loss between the microring and the coupling waveguide i.e. coupling region. Therefore, the microring transmission losses contribute to the intrinsic quality factor (Q_{int}) whereas the coupling quality factor (Q_c) only includes the loss in the coupling region, and finally the loaded Q_L of the system contain the overall loss and are related by the expression

$$\frac{1}{Q_L} = \frac{1}{Q_{int}} + \frac{1}{Q_c} \tag{1.33}$$

The Q_L is usually measured experimentally using the following expression

$$Q_L = \frac{\lambda r}{\Delta\lambda} \tag{1.34}$$

where λ_r is the resonance wavelength and $\Delta\lambda$ is the FWHM of the resonant mode. Using eq. (1.32), Q_L becomes

$$Q_L = \frac{\pi L n_g}{\lambda} \frac{\sqrt{at}}{(1-at)} \tag{1.35}$$

From the definition of Q_{int} explained above, it is energy stored in the isolated microcavity without an external coupling. We can derive Q_{int} from eq. (1.35) by assuming t=1

$$Q_{int} = \frac{\pi L n_g}{\lambda} \frac{\sqrt{a}}{(1-a)} \tag{1.36}$$

As we know that a=e$^{-i\alpha_{ring}L/2}$ is the cavity field, the simplified form of eq. (1.36) can be derived as

$$Q_{int} = \frac{2\pi n_g}{\lambda a} \tag{1.37}$$

Moreover, we theoretically studied the variation of the Q factor at the different coupling conditions. At the critical coupling condition (t=a), we have minimum transmission (T=0) at the throughput as shown in Fig. 1.8. In the cases of the over- and under-coupling conditions the transmission is not zero and is dependent on the coupling gap. The Q_{int} and Q_L are related to Q_L and transmission in the following relations [34]

$$Q_{int} = \frac{2Q_L}{1 \pm \sqrt{T}}, Q_c = \frac{2Q_L}{1 \mp \sqrt{T}} \tag{1.38}$$

Figure 1.12 illustrates the variation of Q with the microring loss coefficient α. At the critical coupling (Q_{int}= Q_c) and the loaded Q can be obtained as $2Q_L$=Q_{int}+ Q_c. As shown in Fig. 1.12, for the case of over-coupling and under-coupling the Q_c is less and greater than Q_{int}, respectively. Therefore, the Q_c i.e., coupling strength, is a significant factor to obtain the desired Q_L.

From the coupling schemes, the extinction ratio (ER) is another significant parame-

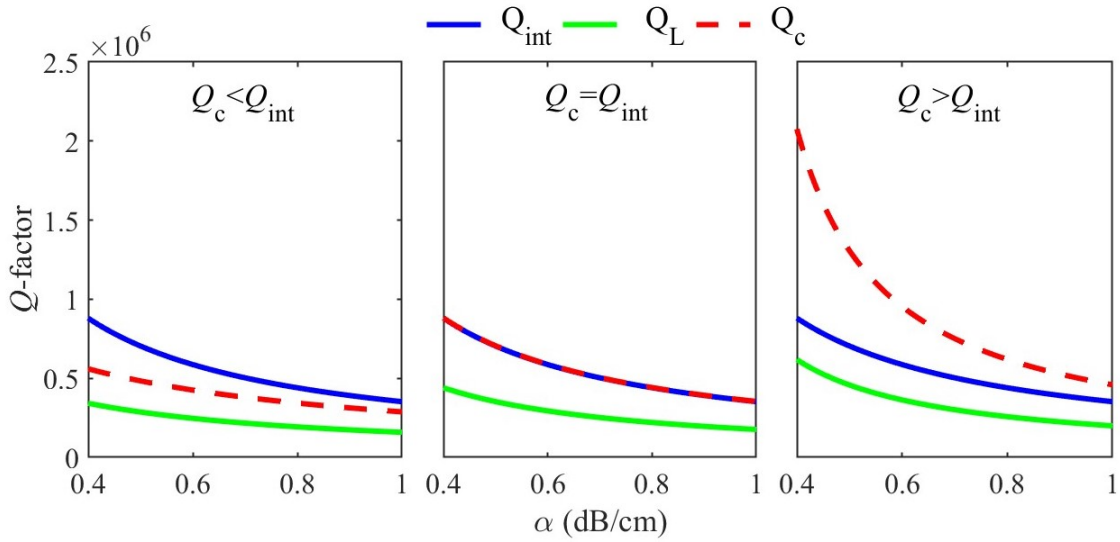


Figure 1.12: Calculated Q-factors versus the cavity loss at the over-coupling, critical coupling and under-coupling conditions.

ter for efficient comb generation. The larger value of ER gives us the critical coupling and the larger value of power enhancement in the cavity. The gap size at the coupling region helps us to achieve the best power enhancement. Experimentally the ER is the difference between the maximum and minimum transmission of the resonant mode. Using eq. (1.14), mathematically ER is the ratio of the transmission maximum value to the minimum value.

$$ER = \frac{T_{max}}{T_{min}} = \left(\frac{Q_{int} - Q_c}{Q_{int} + Q_c}\right)^2 \tag{1.39}$$

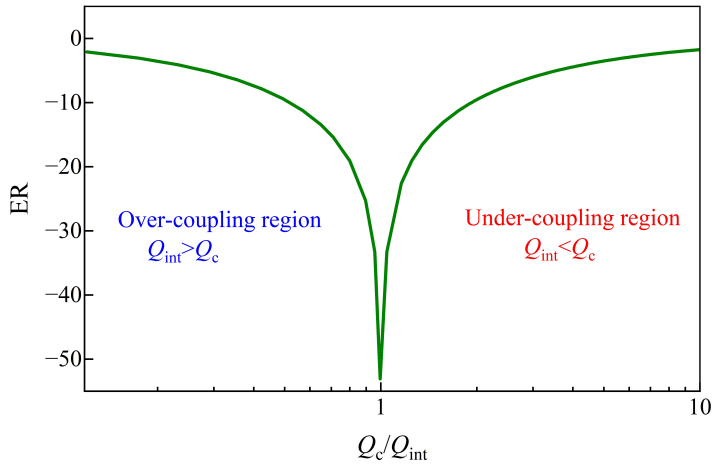


Figure 1.13: Calculated ER variation versus the ratio of Q_c and Q_{int}. At critical coupling (Q_c=Q_{int}) the ER goes to maximum.

Theoretically, the extinction ratio is the logarithm of the ratio of the maximum

transmittance to the minimum transmittance at the transmission end. As shown in Fig. 1.13, the ER is maximum for the case of microresonator critical coupling (Q_c/Q_{int}=1) condition.

$$ER = 10\log_{10}\left(\frac{T_{max}}{T_{min}}\right) \tag{1.40}$$

This chapter mainly introduces the fundamental theory of microresonators including its working principle and basic vital characteristics. Based on the integrated bus waveguide to the microring, characterization parameters of the microring, transmission and enhancement factors as well as the quality factor, extinction ratio, free spectral range, full width half maximum, etc., are introduced and its influence on the optical frequency comb is analyzed at low power. Whereas, the light-matter interaction in the presence of high pump power and dispersion engineering, which is key to efficient microcombs generation, will be explored in the next chapter.

Chapter 2

Dispersion in Microresonators

This chapter discusses the dispersion in microcavities. We studied the relationship between the various geometry parameters i.e., ring width, height and radius, to engineer the dispersion profile for broadband microcombs. Based on the FEM simulations we also proposed future design schemes.

2.1 Optical modes analysis in 2D waveguide

Light is channeled in the core of a dielectric waveguide using the phenomenon of total internal reflection (TIR). Total internal reflection is achieved in optical waveguides where the reflective index of the core (n_2) is larger than the surrounding cladding layer (n_1). For TIR, angle of incident light at the core interface should be less than the critical angle (θ_c) and is given as [35]

$$\theta_c = sin^{-1}(\frac{n_2}{n_1}) \tag{2.1}$$

The schematic of TIR in a 1D waveguide is shown in Fig. 2.1(a). To confine the light in the waveguide core with low loss, we must consider the change in phase as the light propagates. The incident light ray in the core of the waveguide ought to be in phase with itself to achieve constructive interference. Thereby, the light ray is waveguided over a longer distance and with stronger intensity. The propagating light ray with a particular angle in the waveguide corresponds to the waveguide modes. Each one of the modes possesses distinct phase velocity and therefore have a distinct refractive index. Furthermore, the optical waveguide modes have a definite electromagnetic

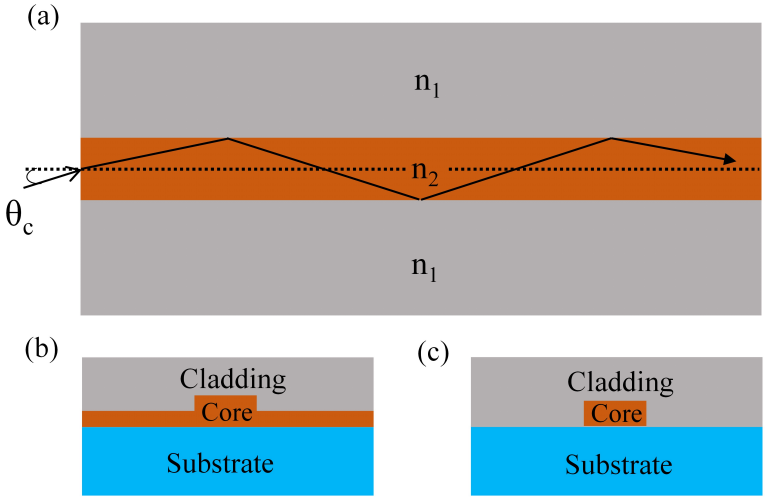


Figure 2.1: Schematic illustration of (a) Total internal reflection (TIR) of light in 1D waveguide. Illustration of the cross-section view of basic geometries (b) rib waveguide (c) ridge waveguide.

field of propagation and modes can be divided into the transverse electric (TE), transverse magnetic (TM) and transverse electromagnetic (TEM) fields. The TE, TM and TEM modes have transverse fields perpendicular to the plane of incidence. In integrated photonics, 2D waveguides with three different refractive indices of substrate, core and cladding are designed. Typically, due to ease in fabrication rib or ridge waveguides geometries are used, schematic of their cross-sectional view is shown in Fig. 2.1(b) and (c), respectively. Therefore, not only different refractive indices but the geometry of waveguides are potentially significant for mode field analysis.

In this thesis, 2D angled ridge waveguides are used, lateral cross-sectional schematic diagram is shown in Fig. 2.1 (c). The finite-element method is used to solve the modes or field distributions. The mode field distribution takes into account both the geometry parameters and the index of core and cladding. Using COMSOL FEM simulations were performed on the 2D axisymmetric geometry of the AlN ridge waveguide with a cross-section of 1.2 $\times$ 3.6 μm^2 (Height and Width) and a radius of 60-μm. The fabrication process is explained in the section below. Considering the experimental structure, the angle of the AlN waveguide (core) is 72°, fabricated on a sapphire substrate and cladding of silicon dioxide (SiO_2), a lateral

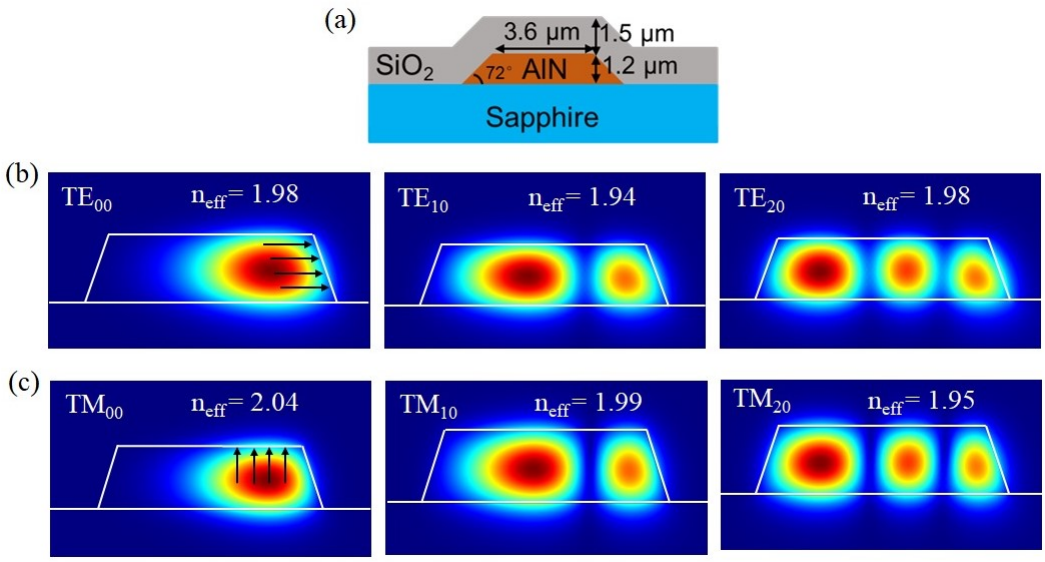


Figure 2.2: (a) Schematic illustration of cross-section our AlN waveguide. Simulated electric field distribution using finite element method (FEM) solver (b) TE mode profiles (c) TM mode profiles.

cross-sectional schematic diagram is shown in Fig. 2.2(a). Figures 2.2(b) and (c) are the FEM simulations of the mode field distributions carried out on our structure at a wavelength of 1.55 μm. Our structure supports both transverse electric (TE) and transverse magnetic (TM) polarization modes. From the simulation results, the field distribution of the TE polarization shows discontinues on the side walls of the core waveguide whereas the field distribution of the TM polarization shows discontinues on the upper and lower edges of the waveguide. The effective refractive index is wavelength-dependent $n_{eff}(\lambda)$ and values vary with variations in the sample geometry. The electromagnetic wave in the waveguide has different modes and each mode with a specific polarization has a different effective index. For TE polarization mode, the waveguide can confine fundamental (TE_{00}), first (TE_{10}) and second (TE_{20}) order TE modes. The effective refractive index (n_{eff}) for the TE_{00} mode is 1.98, n_{eff} for the TE_{10} mode is 1.94 and it is 1.89 for the TE_{20} mode (see Fig. 2.2(b)), respectively. In the case of TM polarization, our AlN waveguide geometry supports fundamental (TM_{00}), first (TM_{10}) and second (TM_{20}) order modes. The effective refractive index for the TM_{00} mode is 2.04, n_{eff} for the TM_{10} mode is 1.99 and it is 1.95 for the TM_{20} mode (see Fig. 2.2(c)), respectively. The difference in the values of effective refractive indices is due to the evanescent field within the cladding material.

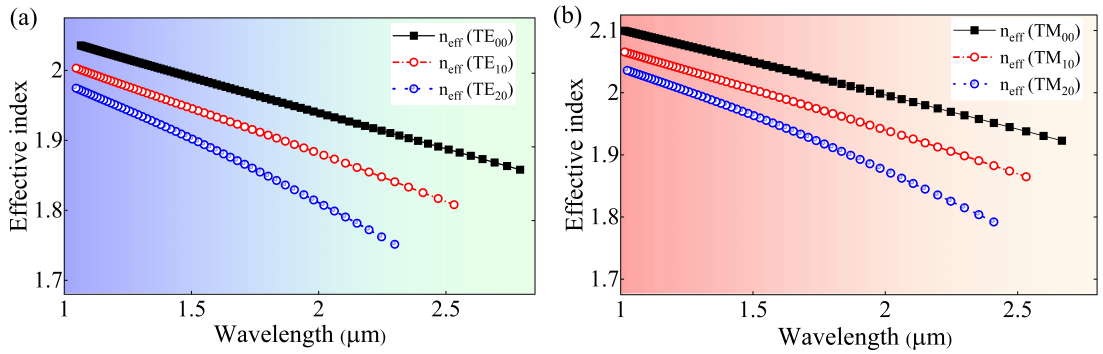


Figure 2.3: (a) Effective refractive index versus wavelength for the TE fundamental, first and second order modes (b) Effective refractive index versus wavelength for TM fundamental, first and second order modes.

Furthermore, to simulate the total dispersion of the waveguide, it is crucial to consider both the material and geometric dispersion. Using an AlN waveguide with 60-μm radius, the height of 1.2 μm and waveguide width of 3.6 μm, the corresponding effective indices versus the wavelength are plotted in Fig. 2.3. The target narrower and wider ring widths used in our thesis are $\sim$2.3 and $\sim$3.6 μm, respectively. The wider structure supports the multi-modes of TE and TM polarizations (see Figures 2.2(a) and (b)). The cut-off wavelength i.e., the particular wavelength beyond which the mode vanishes, for the TE_{00} and TM_{00} modes are $\sim$2.8 μm and $\sim$2.7 μm on the longer wavelength side, respectively. The waveguide can support three modes, fundamental, first and second order TE and TM at shorter wavelengths. The corresponding short cut-off wavelength for TE modes is $\sim$1.1 μm and for TM modes it is around 1 μm. In both cases of TE and TM modes, the effective refractive indices decrease with increasing wavelength, due to the fact, that modal confinement becomes less with the increase in the wavelength and consequently the refractive index for the material decreases.

2.2 Microresonator platforms used in this work

In this thesis, we employed two types of microresonator platforms, aluminum nitride (AlN) and silicon nitride (Si_3N_4), which were fabricated in the Huazhong university of science and technology (HUST) lab [36] and Ligentec (Switzerland) [37]. Similar to Si_3N_4, AlN has a high refractive index of 2.1 at 1.55 μm and therefore strong confinement [38]. It has minimal two-photon absorption (TPA) due to the wide

bandgap (6.2 eV) and is therefore suitable for telecommunication applications [39]. AlN has both third-order (χ^3) Kerr and strong second-order (χ^2) Pockels effect nonlinearities making it wideband comb source and a promising platform for microcomb technology [40][28][41][42][43][44][45]. The presented results in this work are mostly realized using the AlN microring resonators (MRRs) from our HUST collaborators and fabricated using standard lithography (Nikon NSR-2005i9C stepper). The detailed fabrication processes are explained below.

Fabrication process flow of AlN microresonators

The single crystal AlN (1.2 μm) layer was grown on a 430 nm thick sapphire (Al_2O_3) by metal-organic chemical vapor deposition (MOCVD) [46]. The fabrication steps are illustrated in Fig. 2.4 and explained as follows:

I) A thick layer of SiO_2 (800 nm) was deposited using a plasma-enhanced chemical vapor deposition (PECVD). The chromium (Cr) metal layer, a thickness of 70 nm, was deposited on the SiO_2 followed by photoresist spin. The metal layer prior to the photoresist has two functions; first it is used as a conductive layer and second to etch the hard SiO_2, due to low etching selectivity between the SiO_2 and photoresist. Finally, a SPR955 photoresist (900 nm) was spin-coated onto the Cr layer.

II) To produce the straight and ring waveguides, expose the photoresist to an i-line UV illumination system (365 nm Hg spectral peak).

III) Transfer the mask to Cr. Etch the Cr with inductively coupled plasma (ICP) etching technique based on the Cl_2O_2 recipe.

IV) Remove the residual resist.

V) Next, using Cr as mask, the hard SiO_2 was etched using ICP based on SF_6/Ar.

VI) Remove the residual Cr layer with a commercially available Cr-removing solution.

VII) The AlN was etched using a SiO_2 mask. An optimized Cl_2/BCl_3/Ar recipe for ICP dry etching process was employed with the selectivity ratio of 2.4:1 and etching rate of 205 nm/min.

VIII) Remove the residual SiO_2 with the buffered oxide etch (BOE) solution.

IX) Finally, the device is cladded with the thin protective layer of SiO_2 (1.5 μm) by plasma-enhanced chemical vapor deposition (PECVD).

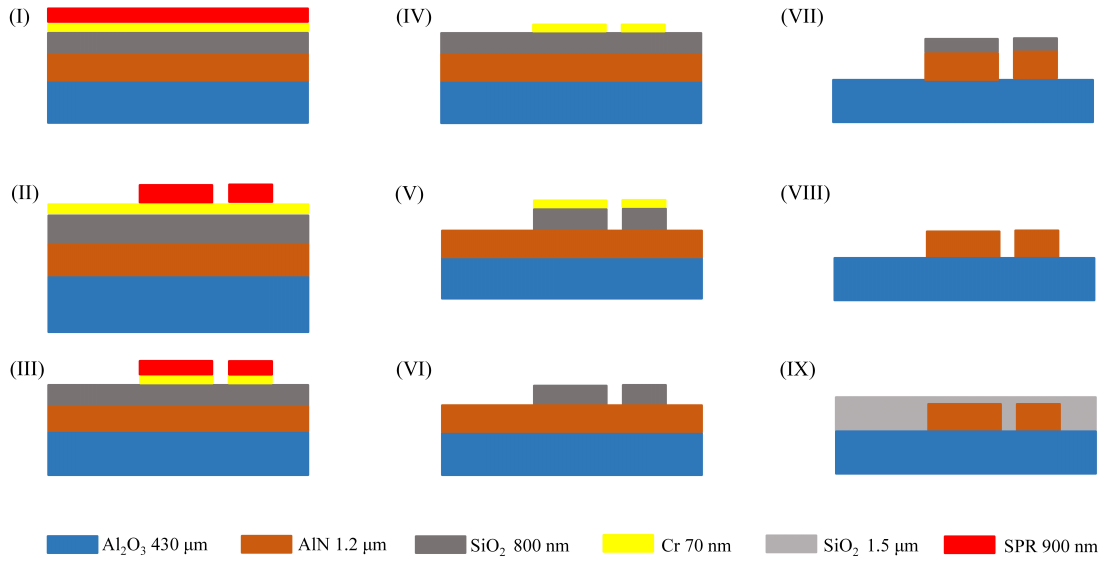


Figure 2.4: Schematic illustration of the fabrication process of AlN microresonators on sapphire using standard electron beam lithography.

2.3 Microresonator dispersion

In any sort of non-linear material, it is essential to understand and control the dispersion of the refractive index. Light with different frequencies travel at a different speed in bulk material due to the refractive index (n) of a material. This type of frequency-dependent refractive indices is known as material dispersion. In the case of integrated optical waveguides, we have an additional dispersion due to the geometry, e.g., width (W), height (H) and angle (θ), of the optical waveguides, known as the geometric dispersion. The propagating light the phase constant (β) of solved modes is directly proportional to the effective refractive index (n_{eff}). Whereas (n_{eff}) accounts for both the material and geometry of the waveguide which is defined as [35]

$$n_{eff} = \frac{\beta}{k_o} \tag{2.2}$$

where k_o is the wave-vector in free space and can be written as $k_o = 2\pi/\lambda$. To further elaborate the cavity dispersion the phase constant, in terms of frequency $\beta(\omega)$, can be expanded in the Taylor series around the frequency (ω_0)

$$\beta_\omega = \beta_0 + \beta_1(\omega - \omega_0) + \frac{1}{2!}\beta_2(\omega - \omega_0)^2 + ... \tag{2.3}$$

From eq. 2.3, (β_0) and (β_1) are related to the phase and group velocities of the light. Whereas, β_2 is related to the group velocity dispersion (GVD) of the propagating light. The explicit information of the pulse broadening lies in the value and sign of the β_2. When the value of β_2 is greater than zero the GVD is known as normal dispersion and in case the β_2 is less than zero the GVD is known as anomalous dispersion. In normal dispersion (β_2>0), the higher frequencies travel slower than the higher frequencies whereas in the anomalous dispersion regime (β_2<0), the higher frequencies travel faster. The microresonator GVD is further explained and simulation results are explained in the section below.

2.3.1 Group velocity dispersion (GVD) in AlN microresonators

The group velocity dispersion (GVD) of a microresonator is typically represented by dispersion parameter D, which explains the variation of n_{eff} with wavelength (λ) in the waveguide core. The parameter can be written as [47]

$$D = -\frac{\lambda}{c}\frac{d^2 n_{eff}}{d\lambda^2} \tag{2.4}$$

where dispersion parameter (D) is expressed in units of ps/(nm-km). Similarly, GVD can be classified into normal and anomalous dispersion based on the value of dispersion parameter D. For this notation, when the value of D is positive (D>0) it is known as anomalous dispersion and opposite to this i.e., (D<0) the dispersion is normal. Anomalous dispersion is crucial and desired for broadband comb generation. The third order (χ^3) Kerr nonlinear four-wave mixing (FWM) is the dominant nonlinear interaction process in the AlN microresonators studied here. Whereas, for an efficient FWM phase matching should be achieved and is made possible by near zero anomalous GVD preferably in the C-band range (1530-1565 nm). Covering the range for commercial applications in sensing and long-distance communications with the low attenuation [48][49].

Geometry of microresonator is most critical to engineer and get near zero anomalous (D≈0) dispersion of modes over a specific spectral range. Using the finite-element method (FEM) solver, GVD profiles are calculated for the AlN microresonator. The

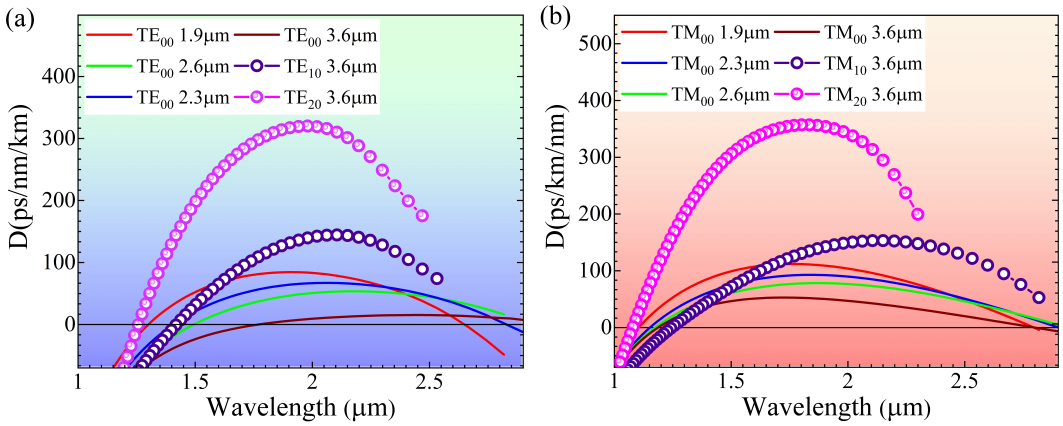


Figure 2.5: Simulated group velocity dispersion (GVD) calculations of a 60-μm-radius and 1.2 μm fully etched AlN microresonator with varying ring widths (RWs) of 1.9, 2.3, 2.6, and 3.6 μm. It depicts the GVD profiles at fundamental and higher orders (for wider RW) polarization modes. (a) TE (b) TM.

parameters of waveguide geometry are based on an experimental structure with a 60-μm radius and the sidewall angle of the core is 72°. We have plotted GVD mode profiles of the AlN microresonator waveguide, shown in Fig. 2.5(a) and (b), with height of 1.2 μm and varying widths of 1.9, 2.3, 2.6 and 3.6 μm. From Fig. 2.5(a) and (b), we can confirm that by decreasing the waveguide width anomalous GVD increases for the TE_{00} and TM_{00} polarization modes. Note that a wider waveguide width of 3.6 μm can support higher-order modes of TE and TM polarizations. From the GVD profiles of the TE polarization modes in Fig. 2.5(a), we find that TE_{00} mode for the waveguide widths of 1.9, 2.3 and 2.6 μm is in an anomalous dispersion region around the telecommunication wavelength range. The dispersion profile of the TE fundamental mode for 3.6 μm width is not favorable for phase-matching as it is in a normal dispersion region below the wavelength of 1.75 μm. The dispersion of higher-order TE modes for the 3.6 μm waveguide has rather larger values of anomalous dispersion. Here, the 2.6 μm width is most suitable as it shows anomalous dispersion but near zero in the spectral range from 1.5 to ~1.9 μm. The TE fundamental mode of the 2.6 μm waveguide can then satisfy the phase matching condition and has the potential for efficient FWM and broadband comb generation. For the TM polarization, the waveguide widths of 1.9, 2.3, 2.6 and 3.6 μm, the fundamental mode GVD supports anomalous dispersion in the telecommunication spectral range, as shown in Fig. 2.5(b). The TM_{00} GVD curve of 3.6 μm waveguide is the most suitable as it presents anomalous and near zero dispersion.

2.3.2 Microresonators integrated dispersion (D_{int})

One of the key drivers of microresonator-based broadband systems and soliton generation in photonic integration is dispersion engineering. Microresonators dispersion profiles can be effectively engineered by tailoring the waveguide geometry. Broadband microcombs of at least an octave-spanning are prerequisites for self-referencing applications in microcomb technology [15][50]. This has been made possible with the engineering microresonators dispersion. Therefore, considerable effort has been made by researchers in studying dispersion in various material platforms and different geometries. Here, dispersion engineering has been studied in aluminum nitride (AlN) and lithium niobate ($LiNbO_3$) waveguides with different geometries.

To simulate the total dispersion of the microresonator, it is crucial to consider both the material and geometric dispersion. The wave-optics module in the COMSOL software can be configured to simulate the effective index and field distributions [51]. Iterative calculations were performed to reveal the eigen frequencies (exact resonance frequencies). The dispersion calculation is illustrated in the flow diagram in Fig. 2.6 and explained in the following steps

1. Define parameters: Select the "2D Axisymmetric" geometry. By implementing 2D axisymmetric simulation considers the 3D structure of the actual model, therefore making the simulation more efficient. Define the geometry parameters and the frequency range. To add the material dispersion the Sellmeier equations of the AlN MRR films are imported to the solver and reveal the refractive index, using the following equations:

$$n^2_{AlN} = \left(2.66 + \frac{1.55\lambda^2}{\lambda^2 - 0.185^2} + \frac{8\lambda^2}{\lambda^2 - 20^2}\right) \tag{2.5}$$

$$n^2_{Al_2O_3} = \left(1 + \frac{1.5039759\lambda^2}{\lambda^2 - 0.0740288^2} + \frac{0.55069141\lambda^2}{\lambda^2 - 0.1216529^2} + \frac{6.5927379\lambda^2}{\lambda^2 - 20.072248^2}\right) \tag{2.6}$$

$$n^2_{SiO_2} = \left(1 + \frac{0.6961663\lambda^2}{\lambda^2 - 0.0684043^2} + \frac{0.4079426\lambda^2}{\lambda^2 - 0.1162414^2} + \frac{0.897479\lambda^2}{\lambda^2 - 9.896161^2}\right) \tag{2.7}$$

2. Simulate n_{eff}: An iterative approach is adopted. Sweep the frequency range and FEM solver will find the effective refractive index.

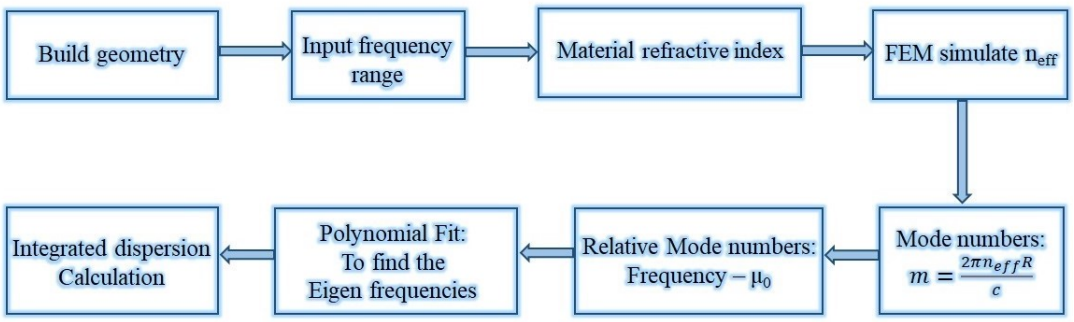


Figure 2.6: Process flow of microresonators dispersion calculation based on the material and geometry dispersion via finite element method (FEM).

3. Calculations: Define the center (pump) wavelength. Calculate the mode number at each frequency for the target mode family. Fit the absolute frequencies with respect to the relative mode number with the appropriate polynomial. The required dispersion parameters are obtained from the fitting.

4. Integrated dispersion D_{int}: Using the Taylor expansion, the resonance frequencies around the pump can be written as [52]

$$D_{int}(\mu) \equiv \omega_\mu - (\omega_0 + D_1\mu) = \frac{1}{2!}D_2\mu^2 + \frac{1}{3!}D_3\mu^3 + ... \tag{2.8}$$

where μ is relative mode number, ω_0 is pump frequency, $D_1/2\pi$ is FSR of microresonator around the pump, $D_2/2\pi$ is second-order dispersion and $D_3/2\pi$ is related to higher order dispersion.

The integrated dispersion (D_{int}) defines the deviation of resonance frequencies and dispersion terms from an equidistant frequency grid, where μ is relative mode numbers of comb lines, $D_1/2\pi$ is FSR around the pump, as shown in schematic diagram in Fig. 2.7(a). The anomalous GVD leads to a mode-locked state where all comb lines are equally spaced else noise will build up during FWM and the microcomb will not be in soliton state [53][16].

Moreover, from the schematic diagram of D_{int} in Fig. 2.7(b), position A is the pump center frequency and MRR modes FSR increases around this point. As the modes move further away from the center at position B modes are at maximum FSRs value. The FSRs decrease on the region after position B where the D_{int} curve has a negative curvature. At position C we access the dispersive wave (DW) where the

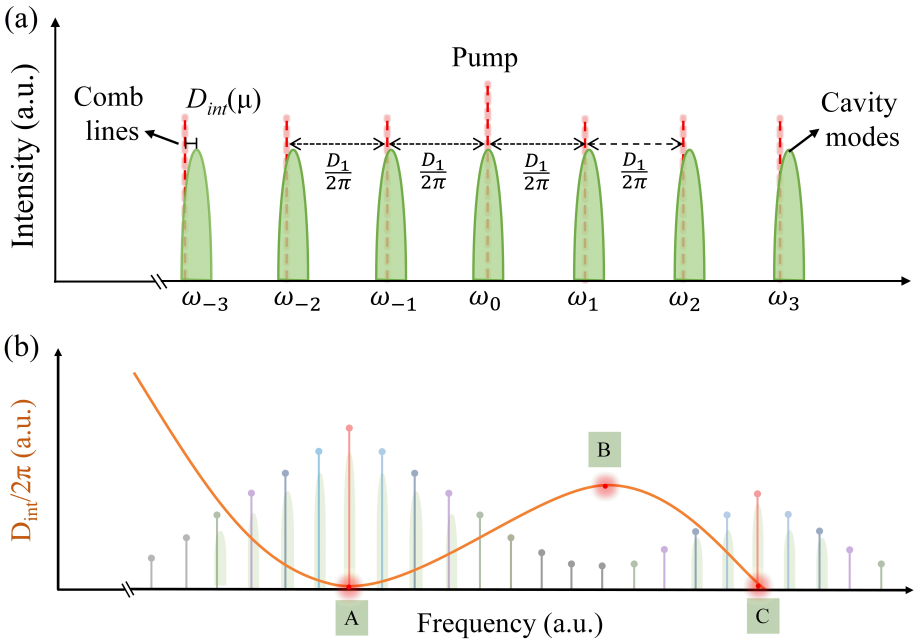


Figure 2.7: Schematic illustration of (a) microresonator resonator modes (green) and comb lines separated by an FSR of $D_1/2\pi$. ω_μ is the angular frequency at relative mode numbers μ, where ω_0 is pump frequency. (b) Integrated dispersion (D_{int}) profile where the pump position is denoted by A, B is the position with positive curvature and FSR separations is maximum and DW wave position is denoted by point C.

value of D_{int} goes to zero. The energy of the dispersive wave is related to the GVD. When the β_2=0 the energy in the wings of the DW can enhance and this is very well presented theoretically in [54]. Notably, a significant amount of experimental work has been reported on the study of DW and consequently is a source of broadening the comb spectrum [55][13][56]. The Cherenkov radiation process leads to a tunable tail in the microcomb spectrum domain. The near-zero anomalous dispersion and suitable third-order dispersion parameter, realized through the rigorous geometry dispersion, can reveal the Cherenkov-induced DW.

D_{int} calculations for AlN MRR at various ring widths (RWs)

Based on the FEM simulation, a series of D_{int} curves are calculated for intracavity TE and TM (fundamental and higher order) mode families. Structure of 60-μm-radius AlN MRR with fixed waveguide height (h) of 1.2 μm and sidewall angle (θ) of 72° designed in COMSOL. The model is scanned for a series of microring top widths i.e., 2.1, 2.3, 2.5, 2.7, 2.9, 3.1, 3.5 and 3.7 μm, respectively. Here all the curves are solved using a fifth-order polynomial fit with center pump frequency (ω_0)

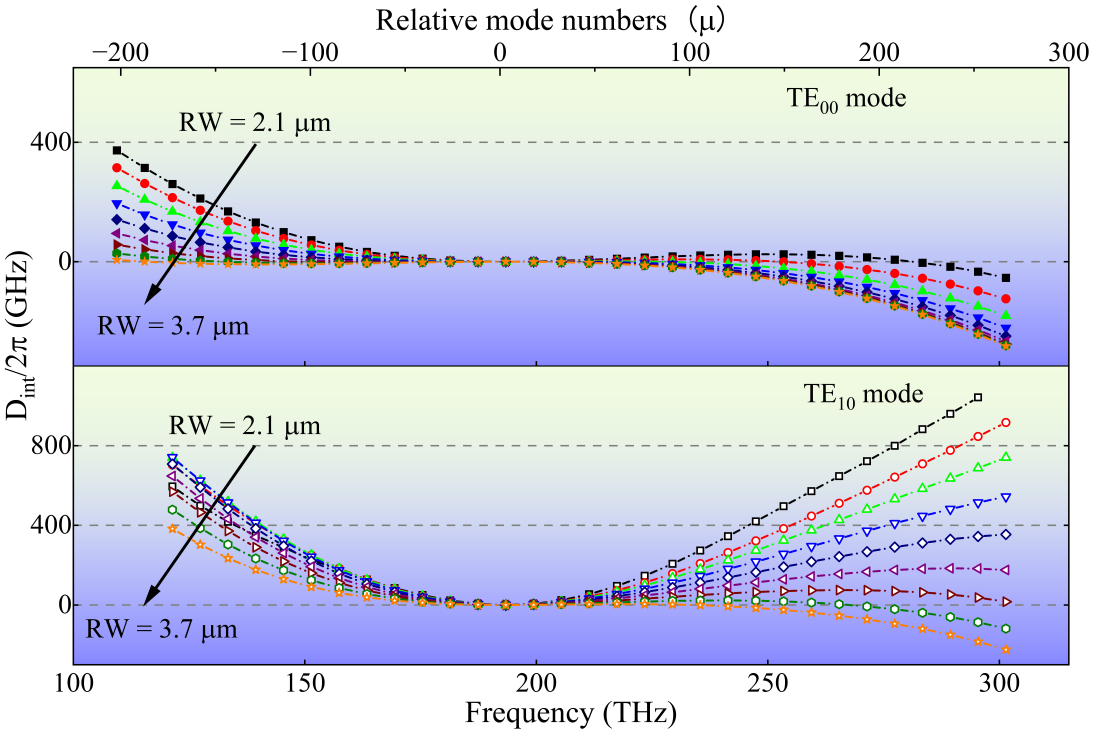


Figure 2.8: Calculated integrated dispersion (D_{int}) of a 60-μm-radius AlN microresonator with fixed height of 1.2 μm and angle of 72°.The Upper panel shows the dispersion curves of TE_{00} mode family at different widths. The Lower panel shows dispersion curves of TE_{10} mode family at different ring widths.

of 193.4 THz (1550 nm). The TE_{00} mode (see Fig. 2.8 upper panel), anomalous dispersion and DW (D_{int}=0) at higher frequency can be accessed for the narrower waveguide (<2.5 μm) widths [27]. Due to the strong electric field mode distribution at the waveguide side wall, the dispersion curves have an obvious shift to the higher frequency range [56]. For the TE_{10} mode (see Fig. 2.8 lower panel), the desired dispersion and DW can be achieved with wider MRR cavities (e.g., 3.5-3.7 μm). The narrower widths waveguide in this case, shows large values of anomalous dispersion i.e., not suitable for efficient broadband FWM.

Similarly, dispersion calculations are made for the intracavity TM_{00} and TM_{10} mode families, shown in Fig. 2.9 (upper and lower panel). Unlike the TE_{00} mode, the TM_{00} mode dispersion curves for the MRR widths of 2.7 μm and wider can achieve a DW (D_{int}=0) at higher frequency as far as ∼295 THz from the pump, as shown in Fig. 2.9 (upper panel). The dispersion profile of waveguide width of around 3.7 μm can exhibit a DW at around 255 THz. Whereas, on the lower frequency range, we have comparably near zero anomalous dispersion makes it a potential design of choice.

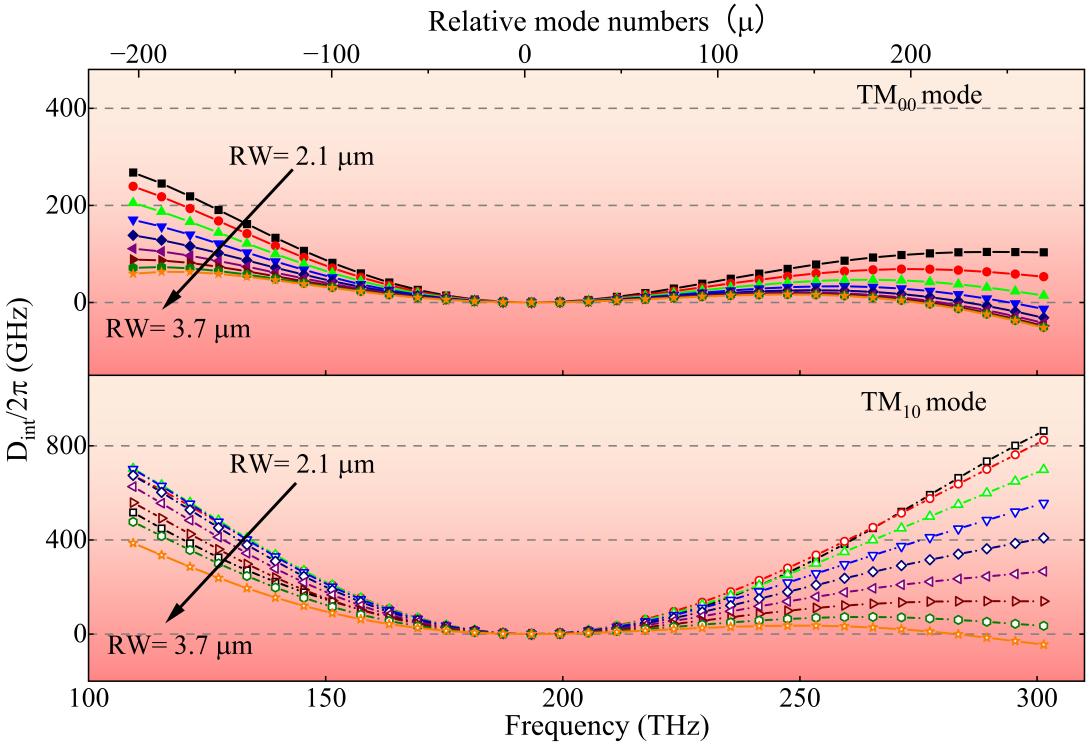


Figure 2.9: Calculated integrated dispersion (D_{int}) of a 60-μm-radius AlN microresonator with fixed height of 1.2 μm and angle of 72°. The Upper panel shows the dispersion curves of TM_{00} mode family at various ring widths. The lower panel shows dispersion curves of TM_{10} mode family at various ring widths.

Integrated dispersion calculations are made for the TM_{10} mode family as well, shown in Fig. 2.9 lower panel. DW in the case of TM_{10} mode can be accessed with wider MRR width at around 283 THz. Finally, the simulated results of TM_{00} and TE_{10} have been experimentally demonstrated for wider AlN MRR in [36][57]. Next, the simulated FSRs for both the TE and TM mode families are extracted using the FEM solver, as shown in Fig. 2.10. The FSR of the TE_{00} and TM_{00} decreases with the increase in the MRR width, where the FSRs increase for TE_{10} and TM_{10} modes, respectively. The simulated FSRs for TE_{00} (∼375 GHz) and TM_{00} (∼364 GHz) from our target waveguide design of a wider (∼3.6 μm) MRR are consistent with the experimental values [36]. Similarly, well consistent results were retrieved for narrow waveguide (∼2.3 μm) MRR [58].

D_{int} calculations for AlN MRR at various ring heights (RHs)

We explore the effect of change in height of MRR waveguide core on the dispersion for the TE_{00} and TM_{00} mode families. The width of the MRR core is kept fixed to

2.3 μm whereas the model is scanned at the various RHs from 1.20 to 1.30 μm at the deviation of 20 nm. The calculated dispersion curves for TE_{00} and TM_{00} mode families are shown in Fig. 2.11 upper and lower panel, respectively. The center pump frequency (ω_0) is taken 193.4 THz. As shown in Fig. 2.11, the change in height has

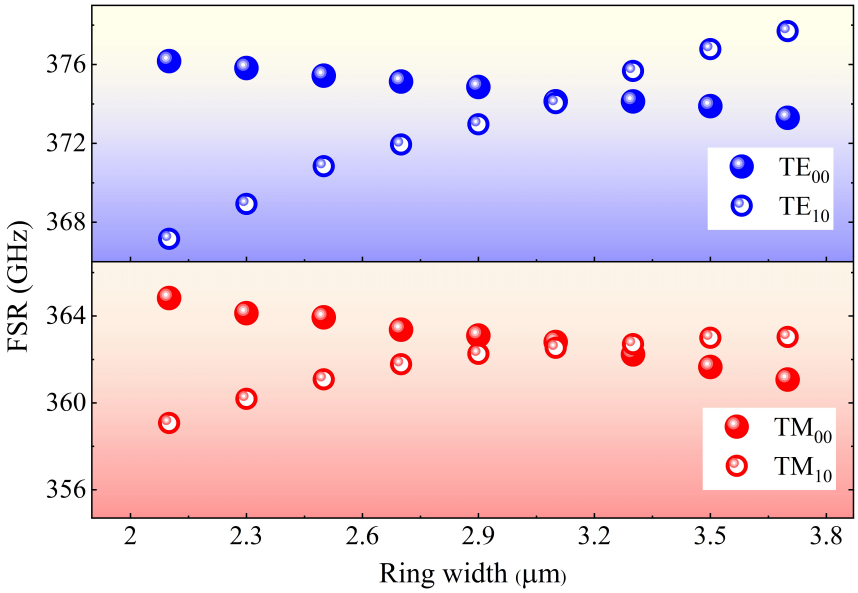


Figure 2.10: Extracted TE and TM modes FSRs with various MRR waveguide widths using the FEM simulation.

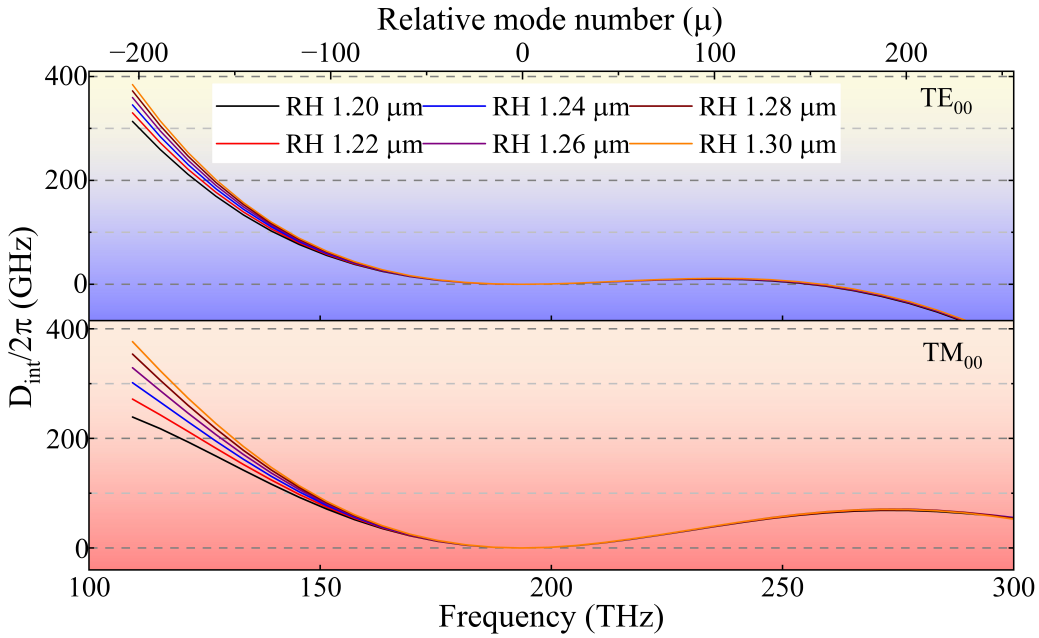


Figure 2.11: Calculated integrated dispersion (D_{int}) of a 60 μm-radius AlN microresonator with fixed width of 2.3 μm and angle of 72°. The Upper panel shows the dispersion curves of TE_{00} mode family at various etching depths. The Lower panel shows dispersion curves of TM_{00} mode family at various etching depths.

a strong influence on the lower frequency dispersion curve. It is worth noting that the TM_{00} mode distribution is on the upper and lower edges of the waveguide. Therefore, the dispersion curve of the TM_{00} mode at the lower frequency range has an obvious shift compared to the TE_{00} mode.

D_{int} calculations for AlN MRR at various sidewall angles (θ)

The accuracy of MRR waveguide sidewall angles is a challenge in device fabrication. It also has a significant effect on D_{int} dispersion engineering. In our target design of the AlN platform, a slight variation of angle has an obvious change in the DW position at a higher frequency range. As shown in Fig. 2.12, deviation of a 2-degrees angle causes the phase-matching point for DW to shift by 10 THz.

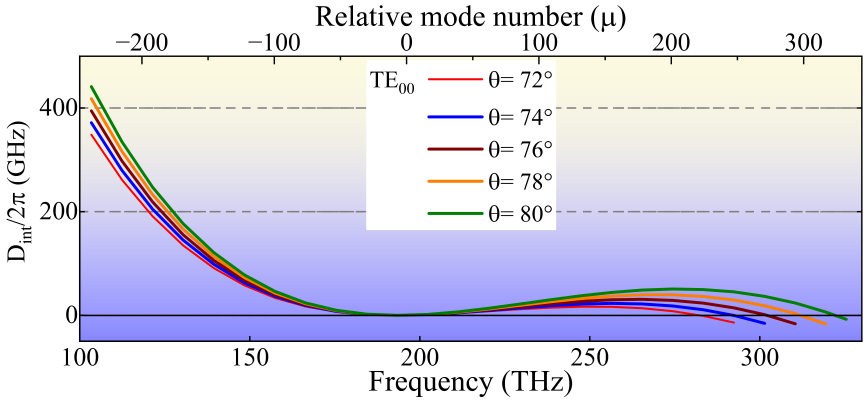


Figure 2.12: Calculated integrated dispersion (D_{int}) of a 60-μm-radius AlN microresonator with fixed width of 2.3 μm and core height of 1.2 μm. Series of D_{int} curves are calculated for a TE_{00} mode family at various sidewall angles of 72°, 74°, 76°, 78° and 80°, respectively.

Integrated dispersion D_{int} in lithium niobate microresonators

Lithium niobate ($LiNbO_3$) exhibits strong χ^2 and χ^3 non-linearities which makes it a potential candidate in microcomb technology and photonic integration with the extension of the comb range into the visible [24][25][59][60]. The $LiNbO_3$ platforms further opening opportunities in many key components desired for commercial applications [61][62][63][64][65]. Besides a high-quality factor (Q), anomalous dispersion is essential for MRR to generate broad Kerr microcombs. Therefore, we explore dispersion engineering for various lithium niobate (LN) geometries using FEM. As

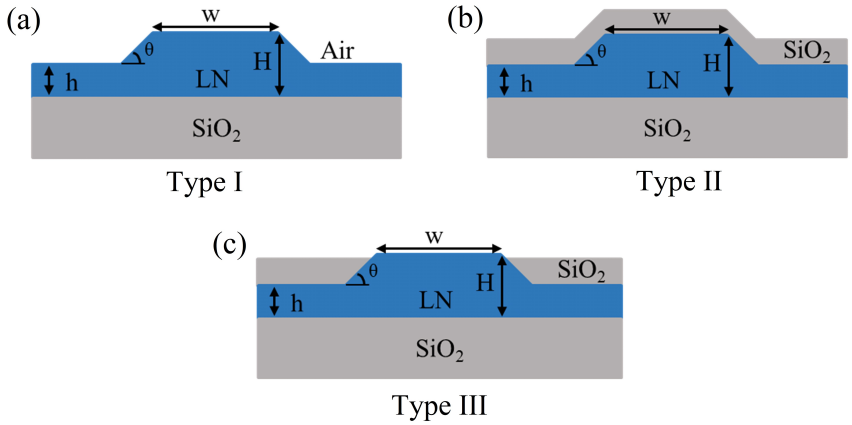


Figure 2.13: Schematic illustration of cross-sections of various proposed LN waveguides designs. W is LN MRR top width; H is total thickness; h is unetched thickness; θ is sidewall angle. (a) Type I is air cladded (b) Type II is SiO_2 cladded and (c) Type III is SiO_2 cladded on etched LN.

shown in Fig. 2.13(a)-(c), all the geometries of LN waveguides have a radius and cross-section (W $\times$ H) of 100-μm and 1.5 $\times$ 0.6 μm^2, respectively. We propose various designs of the cladding layers to fabricate reliable devices with favorable dispersion. Figure 2.13(a) shows the schematic of type-I air cladded LN waveguide. The type-II is where we use 400 nm SiO_2 cladding on LN waveguide as shown in Fig. 2.13(b). In the case of Type-III, shown Fig. 2.13(c), the etched LN (MRR sidewalls) is cladded with 400 nm SiO_2. The AlN MRRs we studied above had an oxide capping and this helped greatly to ensure that the samples were stable and used over a long period. The LN materials are rather thin and so, we also sought to see the effects on the dispersion from capping the samples. In this way, we were able to ensure that devices could also be used over a long period.

Next, we calculated the integrated dispersion for all three types of design schemes, as shown in Fig. 2.14. The Type-I dispersion curve is in an anomalous region with huge hump at a longer frequency side that can lead to weak comb lines [25]. The Typ-II D_{int} curve is in normal dispersion region where D$>$ 0. Type-III has desired near-zero anomalous dispersion and the obtained curve is flat on both the lower and higher frequencies sides.

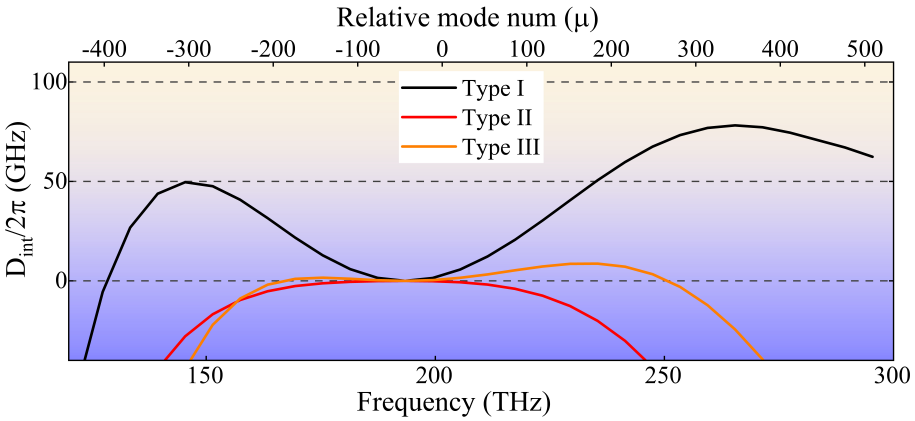


Figure 2.14: Calculated integrated dispersion (D_{int}) curves for 100-μm-radius LN where Type-I is curve corresponds to the air cladded design, Type-II is SiO_2 cladded and Type-III is SiO_2 cladded on etched LN.

2.4 Conclusion

The dispersion engineering plays a crucial role in the satisfaction of the phase-matching condition. The phase-matching leads to the efficient FWM and broadband microcomb spectrum. using the FEM simulations we calculated the integrated dispersion for the two material platforms i.e., AlN and LN. As most of the experimental part in this thesis is from the AlN microresonator we specifically evaluate the AlN cavity dispersion. For the microring cavity, dispersion engineering is done by the variation of the cavity parameters such as microring width (RW), height (RH) and cavity angle. All three cavity parameters are vital in achieving favorable dispersion profiles i.e., near-zero anomalous dispersion. Among all the three parameters we found that the microring top width has more degrees of freedom to tailor the dispersion. Finally, we studied the future potential design schemes of LN microresonators and calculated corresponding integrated dispersion.

Chapter 3

Effect of thermal tuning and mode coupling on soliton microcombs in AlN microresonators

This chapter reports the access to octave-spanning single soliton microcomb in our AlN microresonator using the dual-mode 1P2R strategy. The main goal of this work is to explore mode coupling and how to improve access and increase the stability of the single soliton. Using our standard soliton setup with the thermo-electric controller (TEC), we have performed thermal tuning of the resonance modes and observed a strong mode coupling between the fundamental TE and TM polarization. We present the widest soliton existence range (SER) in this platform with the deterministic generation of octave-spanning-single soliton microcombs.

3.1 Introduction

The demonstration of the DKS in microresonators and achievement of broad spectral width due to soliton-induced Cherenkov radiation, makes it a hot research topic in the nonlinear photonics field and corresponding applications [15][16][17][50][53][66]-[67][68][69]. However, a deterministic, reliable and easy approach to accessing the broadband single DKS is always desired and one of the key challenges. Therefore, sundry experimental schemes have been reported for the generation of stable DKS in various microresonator platforms e.g., fast laser frequency scan, power-kicking scheme, cavity thermal tuning method, dual-pump auxiliary lasers and dual-pump single resonance scheme. To access the stable DKS, reduced thermo-optic effect and

cavity thermal equilibrium is crucial. During the process of pumping, the microresonator cavity heats up due to the thermo-optic effect. Therefore, the method of fast laser frequency scan was introduced to sweep the pump laser with appropriate speed to the red-detuned position and achieve cavity thermal-equilibrium [17][29]. It is important to note that the fast laser scan speed is a viable approach to overcome the intracavity thermal effects and is determined by the Q-factor, thermal response time and pump power. The next reliable developed scheme is Power kicking which is potentially adopted for situations with short-lived solitons [70]. The microresonator cases with strong thermo-optic effects results in unstable short soliton steps. The soliton access in the short step-like region is challenging and not deterministic. Hence, the power kicking approach is used in order to control the power and stabilize the soliton region, additional components such as modulators are required [70][71]. Another approach for stable DKS generation was developed by microresonator cavity thermal tuning [72]. Using the integrated heaters on the cavity allows for a change to the pump frequency with limited tuning. Moreover, the scheme has better stability and low tuning speed compared to the laser frequency scan technique [72][73][74]. These schemes are potentially significant for increasing the short-living solitons existence range. For more reliable and easier access to single DKS, a dual-pump and -resonances scheme was developed [75]. The intracavity thermal instability exists in soliton region which is compensated by using an additional auxiliary laser. The auxiliary laser resonance power and wavelength configuration helps to balance intracavity power allowing the soliton to form [30][75][76]. Another method, for a definite route to generate the stable DKS is dual-pump and single resonance [77]. In this scheme, an optical side-band helps to mitigate the thermal drift and achieve thermal equilibrium for stable DKS generation but with more elaborate equipment needed.

3.1.1 Dual-mode scheme

The schemes discussed in section 3.1 are potentially a significant addition and evolution toward the deterministic generation of DKS. However, the additional requirement of equipment and diverse tuning parameters makes it costly and challenging for many practical applications which require an octave-span broad microcomb. There-

fore, we present a rather simple and robust approach to access an octave-spanning DKSs and is known as a single pump and dual-resonance modes (abbreviated as 1P2R), as reported in [27]. The two adjacent resonance modes with the same polarization are requisite of this scheme. Figure 3.1(a) is the schematic illustration of the setup used for stable DKSs generation using the 1P2R approach. Here the fundamental TE (TE_{00}) resonance is the pump mode and initiates the nonlinear process of four-wave mixing (FWM). Whereas the high order TE (TE_{10}) resonance is an auxiliary mode that is employed to achieve thermal equilibrium and thereby stabilize the soliton. The stages to realize a stable DKS using the two adjacent modes are shown in the schematic diagram of Fig. 3.1(b). The pump mode (TE_{00}) is in the blue-detuned region away from the cavity resonance (C-resonance). We scan (forward-tuning) the pump wavelength into the C-resonance (see Fig. 3.1(b) stage (i)), a primary comb with the side-bands of multi-FSR appears. On further detuning the laser wavelength in the C-resonance, such that the power is injected into the TE_{00} and the TE_{10} resonances modes, due to the thermal effect both resonance modes will red-shift (see Fig. 3.1(b) stage (ii)). As from the Fig. 3.1(b) stage (ii), the pump is still on the blue side of the TE_{00} mode, an unlocked microcomb with modulation instability (MI) state is observed. With the increase of the pump wavelength into the red-detuned position, the TE_{10} auxiliary resonance mode helps to mitigate the cavity thermo-optic effect. We observe a sudden reduction in the cavity power and the TE_{10} mode now takes most of the pump power with a slight blue shift as shown in Fig. 3.1(b) stage (iii). Therefore, a stable single soliton is accessed in the presence of the auxiliary TE_{10} mode. Further, the pump splits into the C-resonance and soliton resonance (S-resonance). Due to access energy dissipation, the amplitude of the S-resonance is lower and depends on the number of solitons (N). At this stage of stable DKS/s evolution a step/s like a region appear in the intracavity power as shown in Fig. 3.1(c) stage (iii). It is also worth mentioning here that an octave-spanning soliton has been demonstrated with the dual-mode mixed polarization strategy in a previous study [20]. However, accessing the octave-spanning DKS using dual-mode with mixed polarization requires very precise polarization control. In contrast to the 1P2R mixed polarization, our strategy of the 1P2R with the same polarization modes is a simpler route for soliton creation and the resonance modes

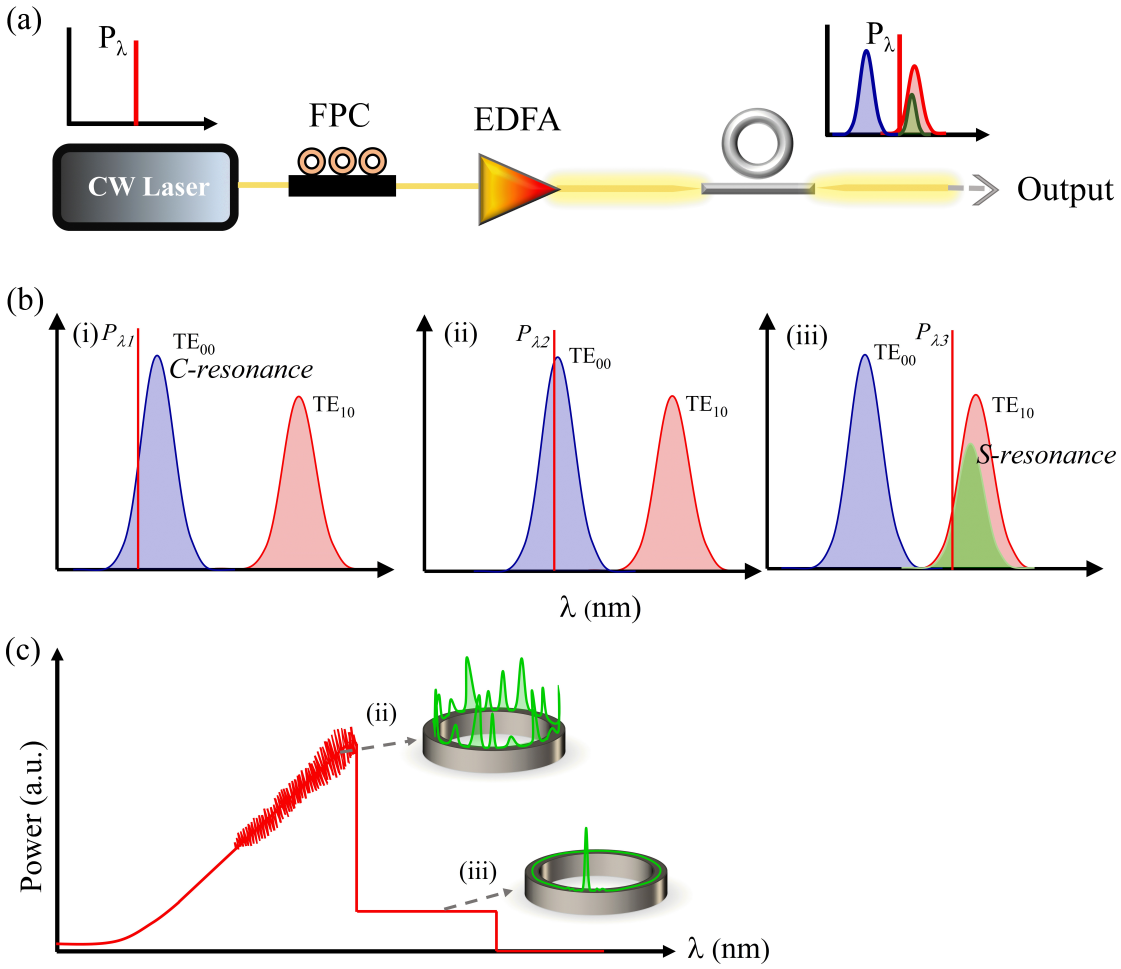


Figure 3.1: (a) Schematic illustration of setup used for the Kerr soliton generation using the dual mode (1P2R) strategy. CW laser: continuous wave laser; FPC: fiber polarization controller; EDFA: erbium-doped fiber amplifier. (b) Principle of thermal compensation using the dual modes scheme. At state (i) the pump wavelength $P_{\lambda 1}$ is coupled into the main resonance (TE_{00}). When tuning the pump wavelength to $P_{\lambda 2}$ position in the state (ii) the power is coupled to both the modes and relatively red shifts. Soliton state (iii) is reached when tuning the pump to the $P_{\lambda 3}$ position i.e., the red-side of the pump resonance. The pump mode slightly blue shifts accompanied by a reduction in the cavity power which is compensated with the help of TE_{10} mode that stabilizes the soliton state. (c) Diagram of intracavity power and the evolution of different wave-forms at the different states of the DKS generation.

separation can be potentially engineered by careful geometry design and fabrication. We have successfully demonstrated an octave-spanning DKS using the 1P2R approach in two microresonator platforms i.e., AlN and Si_3N_4, respectively. Here we will focus on the results AlN microring resonator (MRR), being our first platform where we reported an octave-spanning DKS microcomb using the 1P2R scheme.

To realize the two adjacent modes an optimal cavity layout structure is vital. There-

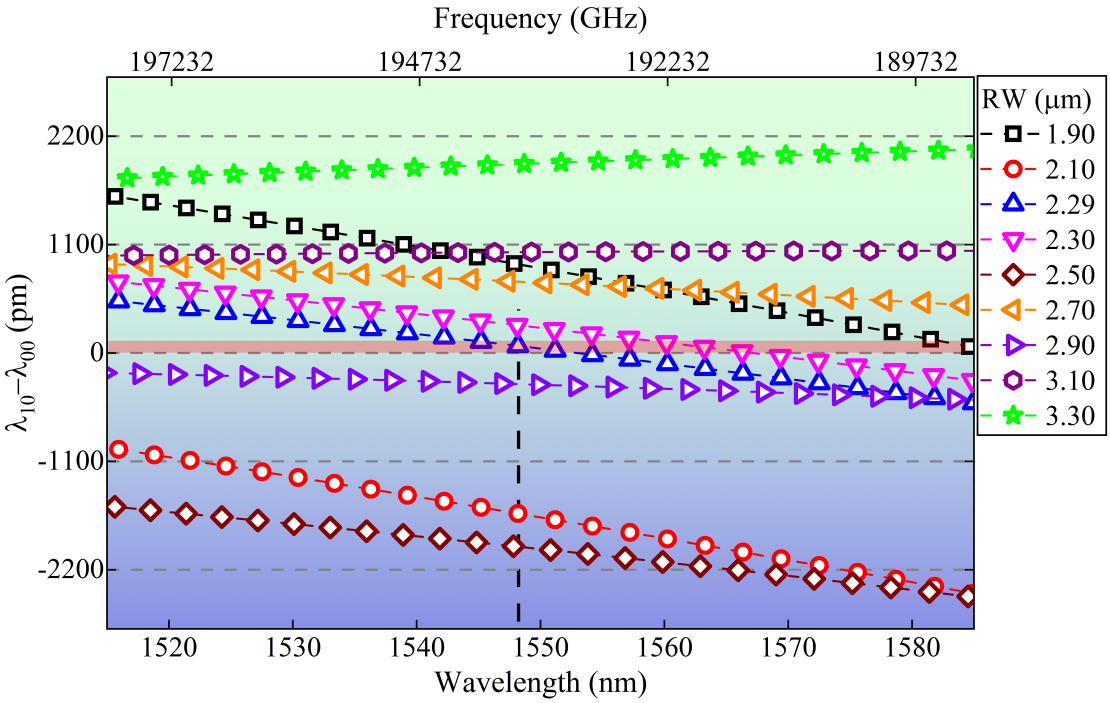


Figure 3.2: Simulated separations between two adjacent TE resonance wavelengths for an AlN MRR with the radius of 60 μm, the thickness of 1.2 μm and various RWs.

fore, we simulated the resonance wavelengths by calculating the eigenfrequencies using COMSOL multiphysics. Figure 3.2 shows wavelength separations (range, 1515 nm to 1585 nm) of a fixed 60 μm-radius-AlN MRR with varied ring widths (RWs). The overall slope (dλ/dW) decreases with the increase in the RWs. It is also important to mention those positive separations with pump (λ_{00}) at the blue side is of particular interest. For the narrower RW ~2.29 μm (used in this experiment) we can observe two close modes at ~1585 nm and ~1548 nm, respectively. Note that a shift in the two near modes of ~15 nm occurs when changing the RW from 2.29 to 2.30 μm. Whereas in the case of 3.10 μm width the separation is almost constant due the nearly equivalent FSRs i.e, ~372 GHz.

3.2 Device characterization

Figure 3.3(a) illustrates the experimental setup used to test the performance of the AlN device and measure the resonance characteristics such as Q-factor, ER and coupling loss. A continuous wave (CW) laser (Santec TSL710) is used to characterize the device in the wavelength range of 1543 nm to 1563 nm. The output power is set

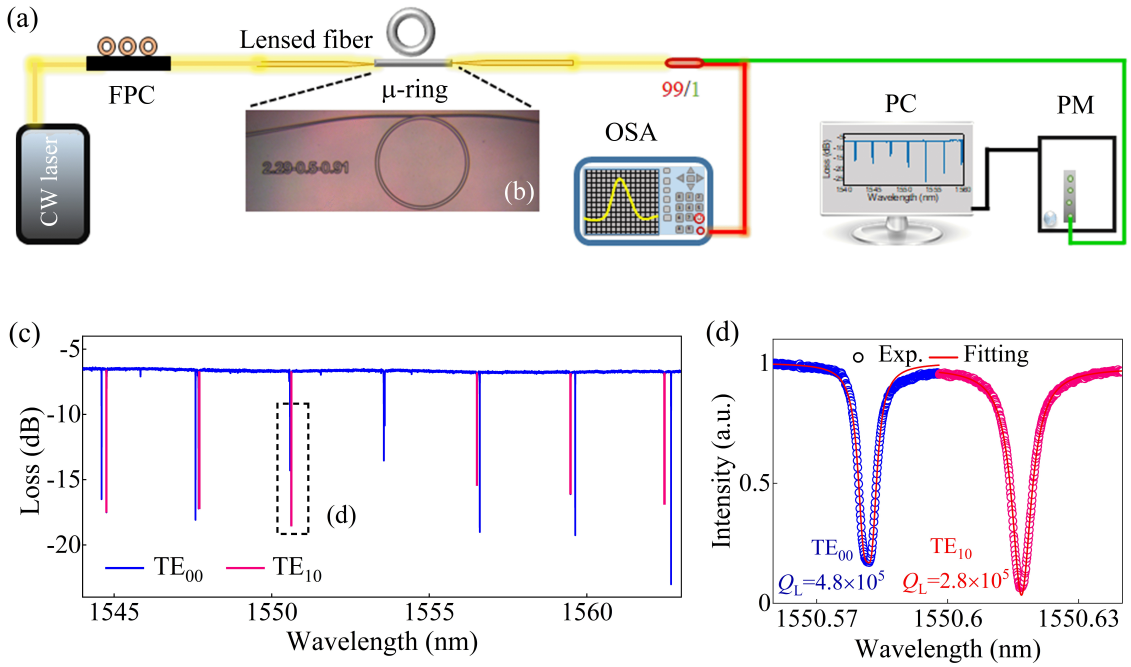


Figure 3.3: (a) Experimental setup used for device characterization. CW: continuous wave laser; FPC: fiber polarization controller; OSA: optical spectrum analyzer; PM: power meter. (b) Microscopic image of one of the devices used in this work. (c) Measured transmission trace of the device with TE mode polarizations. (d) Zoomed in image of the two fitted adjacent modes at around ∼1550 nm.

to -14 dBm, to minimize the thermo-optic effect, and a resolution of 0.1 pm is set to retrieve the cold cavity transmission, ER and the Q-factor. The output power passes through the fiber polarization controller (FPC) to distinguish and select the desired input polarization. The inset microscopic image of the employed microresonator is shown in Fig. 3.3(b). The light is pumped into the bus waveguide via tapered lensed fibers with a diameter of 2.5 μm. The light at the output is collected by another tapered lensed fiber and is split using 99/1% fiber coupler. The fiber coupler sends 99% of the light to the optical spectrum analyzer (OSA) to detect the coupling signal. Whereas the rest 1% of light goes to Santec power monitor (MPM210) to obtain the transmission spectrum.

Figure 3.3(c) shows the transmission spectrum of the transverse electric (TE) polarized light over the range of 20 nm. In the case of TE polarization, the design can support the two TE modes i.e., fundamental (TE_{00}, blue colored) and first order (TE_{10}, magenta colored) which is consistent with the simulation results in chapter 2 section 2.1. Form the measured transmission spectrum the optical insertion loss is ∼6.4 dB, mainly from the coupling loss at the facets of the waveguide. Hence

the coupling loss of the device can be reported ∼3.2 dB per facet. Furthermore, the polarization modes can be distinguished by measuring the free spectral range (FSR) of resonance modes [28]. The measured FSRs of TE_{00} and TE_{10} resonance modes at around 1550 nm are around 374 GHz and 366 GHz, respectively. From the transmission spectrum the resonance modes FSR change due to dispersion. We can achieve the two nearby modes at around ∼1550.68 nm, zoomed-in image is shown in Fig. 3.3(d). The separation between the two adjacent modes, TE_{00} (at around 1550.58 nm) and TE_{10} (at around 1550.62 nm), is 35 pm (∼4.37 GHz). The Lorentzian fitting is used to measure the linewidth and extract the loaded quality (Q_L) factor. The 3-dB linewidth of the TE_{00} and TE_{10} modes are ∼3.5 and ∼5.6 pm, their corresponding loaded quality (Q_L) factors are $\sim 4.8 \times 10^5$ and 2.8×10^5, respectively. The essential physical properties of a microresonator are related to the intrinsic Q-factor (Q_{int}). As shown in Fig. 3.3(d), at around 1550.5 nm the two Q_L factors approach each other indicating weak coupling between the two transverse resonance modes. Owing to the weak coupling effect at around 1550.5 nm the intrinsic Q for the TE_{00} mode is calculated near 1562 nm and taking an over-coupling condition the extracted Q_{int} is 1.4×10^6.

3.3 Experimental setup and generation of an octave-span dissipative Kerr soliton (DKS)

The experimental setup used for the demonstration of an octave-spanning DKS is shown in Fig. 3.4(a). A continuous wave (CW) laser is the foremost component used as a seed. The Santec TSL-710 (tuning range, 1480 nm to 1640 nm) CW laser is used in our setup with a low linewidth (<100 kHz). A fiber polarization controller (FPC) is connected at the output of the CW laser to select and distinguish the resonator transverse modes. To pump the microresonator, a certain threshold power is required to initiate four-wave mixing (FWM) and overcome the coupling and waveguide losses, respectively. The desired TE polarization (in this case) is adjusted, it is boosted by an IPG photonics erbium-doped amplifier (EDFA, maximum output power of 5W). The amplified light is coupled into the waveguide using a lensed fiber with a spot diameter of 2.5 μm. Light at the output of the chip is collected by another lensed fiber with the same spot diameter. The input and

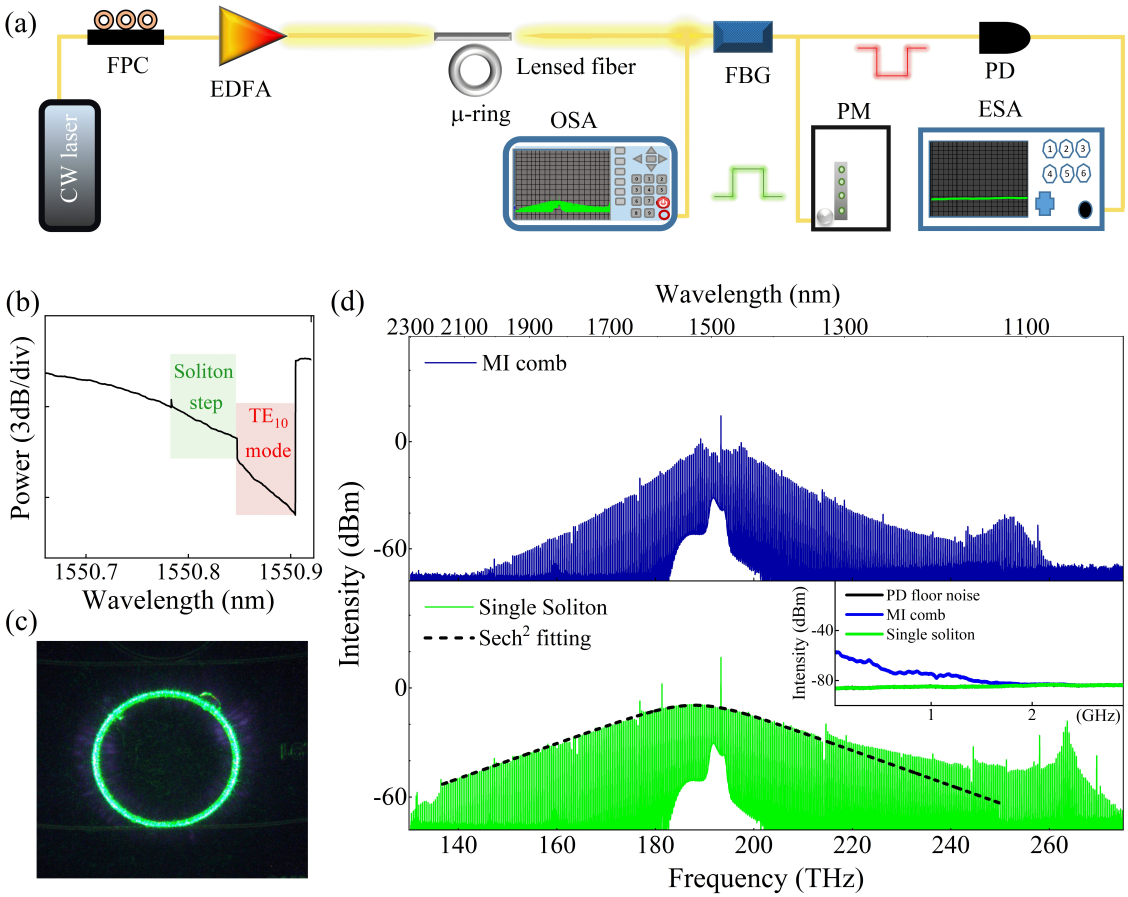


Figure 3.4: (a) Standard experimental setup used for DKS generation. CW: continuous wave seed laser (Santec TSL-710); FPC: fiber polarization controller; EDFA: erbium-doped fiber amplifier; OSA: optical spectrum analyzer (Yokogawa-AQ6375B); FBG: fiber Bragg grating; PM: power meter (Santec MPM-210); PD: photodiode; ESA: electric spectrum analyzer. (b) Recorded transmission trace of the two adjacent modes at 350 mW on-chip and laser sweep speed of 1 nm/s. The different color shadings on the transmission trace correspond to the soliton existence range (SER) and TE_{10} mode. (c) Microscope image of strong green light observed at the soliton state. (d) Measured optical spectra. Upper panel: MI comb, lower panel: single soliton and fitted with the $sech^2$ envelope (black dashed line). Inset is the recorded RF noise spectra of the corresponding MI (blue), single soliton (green) microcomb states and the PD noise floor (black).

output lensed fibers are fixed as recommended to prevent any kind of mechanical vibrations to ensure stable coupling. After the output lensed fiber, the light is split into two branches, one of which is connected to a Yokogawa-AQ6375B optical spectrum analyzer (OSA) to record the spectral output of the microresonator. To study the transmission, microcomb power and characterize the microcomb coherence a fiber Bragg grating (FBG, range 1545 to 1565 nm) with 0.4 nm bandwidth is used. The bandpass (BP) part of the FBG is connected to Santec multi-port MPM-210

power meter (PM) to measure the transmission and monitor the coupling power. At high power injection to the chip and operating the experiment for a long time induces heating in the chip itself and the holder which can potentially change the coupling position of the lensed fibers, consequently, a change in coupling power can occur. The persistent monitoring of the transmission power using the PM helps to adjust the lensed fiber to the best coupling position and reduce the coupling loss. The notch filter, which is narrow in our case (Gaussian shaped), is connected to an electrical spectrum analyzer (ESA) to observe and record the radio-frequency (RF) noise of the generated combs.

To access a single soliton state in a microcavity, we select a suitable pump (enhanced by the EDFA) to the build-up of an intracavity power. The pump power depends on the resonance wavelength Q-factor, ER and separation in the two adjacent pump modes (see Fig. 3.3(d)). Both the pump and auxiliary laser wavelengths red-shift due the cavity thermal effects. We sweep the pump laser wavelength at a faster tuning speed, of 20 nm/s, from blue side of the pump (TE_{00} mode) to the red-detuned position of an auxiliary pump (TE_{10} mode). During the sweeping of the laser wavelength, we slightly adjust the FPC paddles to the best possible position to access the soliton step. The soliton step is the region where soliton state exists and we now name as the soliton existence region (SER) [70]. Figure 3.4(b) shows the recorded transmission trace with a power of 350 mW on chip and a relatively slow sweep speed of 1 nm/s. The green marked area on the transmission trace with an obvious step is the SER and the red marked area is the TE_{10} resonance mode. This SER is calculated to be 63 pm (in range ∼1550.78 and ∼1550.84 nm) wide. We note the higher ER of the TE_{10} mode is due to the low Q-factor and higher cavity absorption. It is worth mentioning that the soliton-step and soliton-excitation in the cavity can be confirmed in a more convenient way by the strong green light observation (corresponds to the third-harmonic generation (THG)), as shown in Fig. 3.4(c). The soliton excitation in the cavity is a non-trivial process, beside the device parameters and suitable laser wavelength tuning speed, the pump power is constantly monitored using the PM. After the confirmation of the soliton step, an octave-span DKS is accessed using the laser forward tuning (towards longer wavelength) technique. Where we sweep the laser wavelength from the blue-detuned position of the pump

to the red-detuned position on the SER to access the DKS. Figure 3.4(d) upper panel is the recorded optical spectrum of the MI comb in the range 140 to 260 THz and the lower panel shows an optical spectrum of an octave-spanning DKS with a FSR of 374 GHz and having a spectral range from 130 to 273 THz (1100-2300 nm). Whereas at ∼264 THz (∼1136 nm) a small hump known as dispersive wave (DW) appears that occurs due to the soliton-induced Cherenkov radiation [55][16]. The DW extends the DKS spectrum towards a shorter wavelength. It is important to mention here that the wide SER lets us not only achieve the deterministic generation of an octave-span DKS by sweeping the laser wavelength at a slow speed of 1 nm/s, but also with the slow laser piezo tuning (by hand) at a several GHz/s. Furthermore, fitting the spectral envelope with a $sech^2$ shape (black dash line), we can find the full-width half-maximum (FWHM) of the soliton to be 15.2 THz, which corresponds to a 21 fs pulse width. The pulse width is obtained using 0.315 for the bandwidth-limited pulses multiplied by the FWHM of the $sech^2$ pulse shape. The comb states can be confirmed by the radio frequency (RF) spectrum, as shown in the inset of Fig. 3.4(d) lower panel. The MI comb has the broader noise (blue), the low-noise corresponds to the soliton state (green) and this corresponds to the noise floor of the PD used for measurements (black).

3.4 Thermal tuning of resonance modes

To study the effect of temperature control on the resonance modes and the mode coupling between the two close modes, we used the same procedure and experimental setup as explained in section 3.2 but with the addition of a thermo-electric controller (TEC). Figure 3.5(a) shows the scheme of the setup with the TEC addition and the inset is the microscopic image of the coupled system. To extract the transmission traces at the desired temperature, we first set the TEC temperature and let the coupling system stabilize. Next, using the FPC we select the pure TE polarization identified from their FSRs (374 GHz for TE_{00}, 366 GHz for TE_{10} and 364 GHz for TM_{00} modes). For the transmission traces at various temperatures, we repeat the two-step procedure. Figure 3.5(b) shows the typical transmission traces in the wavelength range between 1547.5 nm to 1557.5 nm, at the temperature range from

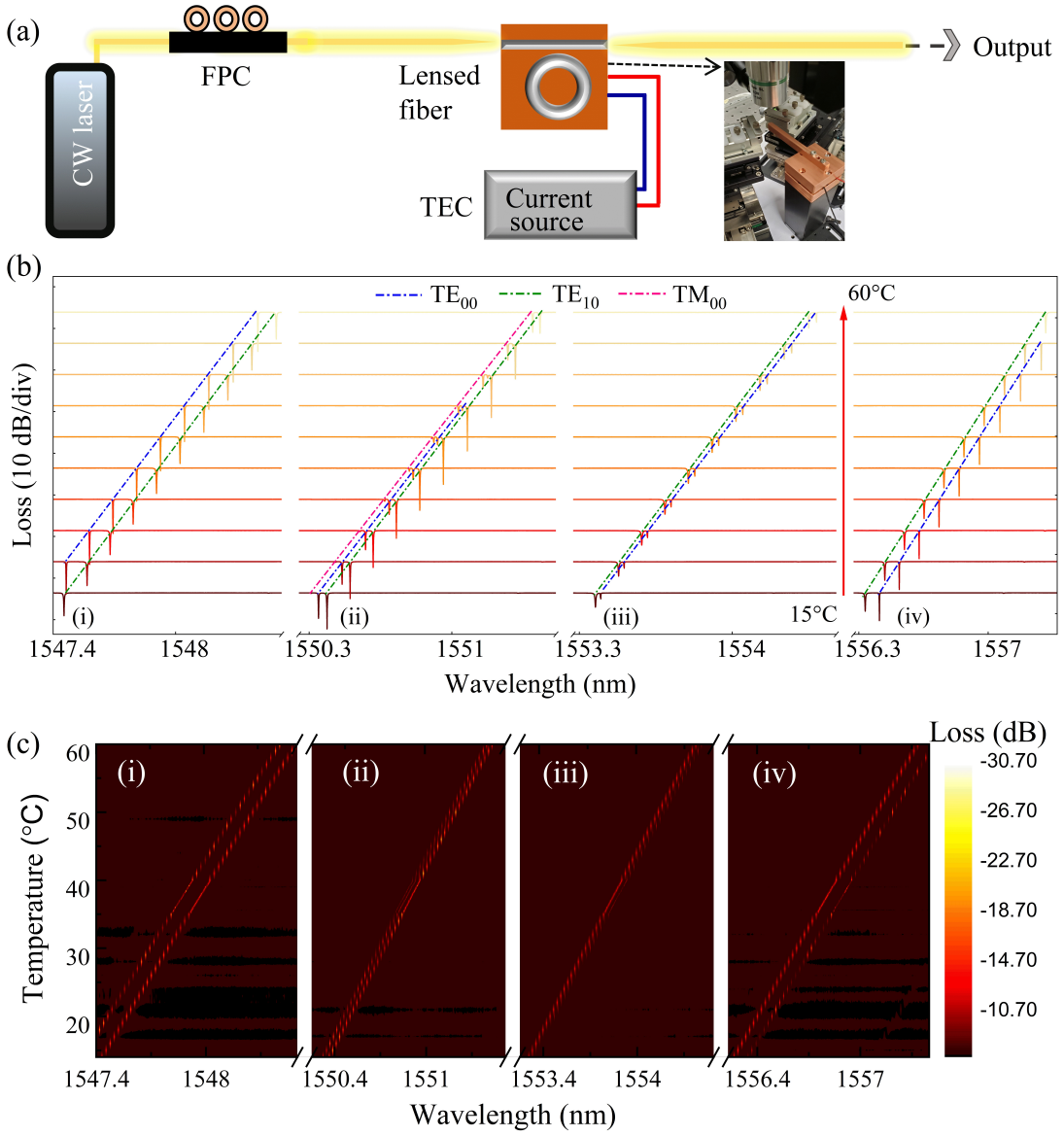


Figure 3.5: (a) Standard experimental setup used for device transmission spectra measurements with the addition of a thermo-electric controller (TEC). Inset is the microscopic image of the coupling system. (b) Measured transmission spectra of four groups of TE resonances, between 1547.5 to 1557.5 nm wavelength range, at various temperatures. (c) Maps of the TE_{00} and TE_{10} modes in the regions (i)-(iv), in temperatures ranging from 15°C to 60°C. The TE_{00} mode is on the left in the regions (i) and (ii) whereas in (iii) and (iv) it shifts to the red side, respectively. In region (ii), the TM_{00} mode appears at temperatures above 30°C.

15 to 60°C, the insertion loss is around 6.4 dB, respectively. For clarity, we shift all transmission traces by 15 dB and denote the resonances in four groups (i)-(iv). Possessing a larger FSR, the TE_{00} modes (denoted by blue dashed lines) are on the blue side of the TE_{10} modes (denoted by green dashed lines) in the regions (i) and (ii) whereas in regions (iii) and (iv) the TE_{00} modes moves to the red side.

The mode coupling phenomenon is common in multi-mode microresonators and can occur between the two adjacent modes that have different transverse orders or polarizations [78]. Such mode coupling can potentially cause localized anomalous dispersion [20] and has been exploited to generate dark-pulse [79][80], dispersive wave (DW) [81] and soliton crystals (SCs) [82][83]. The AlN microresonators waveguide used in this thesis are multi-mode therefore the mode coupling phenomenon is often observed. We note that in region (ii), the TM_{00} mode (marked magenta colored dashed line) appears at higher temperatures which we attribute to the mode coupling with the TE_{00} mode. Figure 3.5(c) shows the maps of the resonances at the various temperatures for the regions (i)-(iv), respectively. Distinctly, all the resonance modes are red-shifted at various TEC temperatures due to the thermo-optic effect [84]. Figure 3.6(a) is the zoomed-in image of the two adjacent pump modes in the region (ii). An obvious TM_{00} mode (marked with a magenta colored square) appears due to mode coupling at higher temperatures. In region (ii), for simplicity, we denote the two fundamental modes (i.e., TE_{00} and TM_{00} modes) at the red- and blue-sides as A and B, below the temperature of 35°C, respectively. Furthermore, to characterize the resonance modes with respect to the temperature, we calculate the wavelength separations between the TE_{10} mode and adjacent fundamental modes, as shown in Fig. 3.6(b) (upper panel). The relation used for the separations calculation is defined as $\Delta\lambda$=λ_{TE10}-λ_{TE00} and λ_{TE10}-λ_{TM00} and 1°C temperature step was used for careful analysis of the modes A and B. The extinction ratios (ERs) versus temperature, of the fundamental modes A and B in region (ii), are plotted in the lower panel of Fig. 3.6(b). In region (ii), at 14°C, the separation between the TE_{10} mode and the fundamental resonance modes A and B are ∼41 and ∼79 pm. An avoided mode crossing is caused between the hybrid modes A and B above ∼35°C and because of mode coupling a significant change in the ERs is observed. In region (i), the two adjacent modes separation linearly decreases from 102.3 to 91.76 pm with the temperature increase from 20°C to 55°C. Similarly, for regions (iii) and (iv), the separations have a smaller increment of 9.4 pm and 10.6 pm. Based on the calculations, we can estimate the separation decreases ∼1 pm with the step of 5°C increment. Therefore, without mode coupling in region (ii), the separation between the two adjacent modes would be ∼31 pm at 60°C, which is sufficient separation to

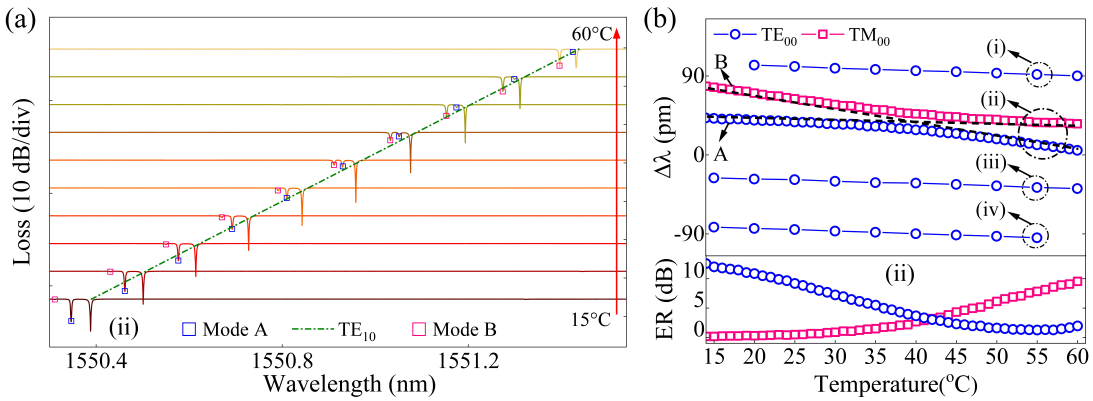


Figure 3.6: (a) Zoomed-in image of transmission spectra of TE resonances (region ii) near 1550 nm at different temperatures with a step of 5°C. (c) Upper panel: The difference of the resonance wavelength between the TE_{10} and TE_{00} modes [also the TM_{00} mode in region (ii)] at different temperatures. Lower panel: The extinction ratios (ERs) versus temperature of the modes A and B.

generate the single soliton at room temperature [27].

For further analysis of the thermal effect on the characteristics of resonance modes, we study the two adjacent modes without the coupling effect. The thermal effect on the quality factor and FSR of the resonance modes are shown in Fig. 3.7. By increasing the temperature from 15°C to 60°C the modes Q-factors remain unchanged, as shown in Fig. 3.7(a). Whereas in Fig. 3.7(b), TE_{00} modes FSR decreases by ∼0.25 GHz with the increasing of the temperature.

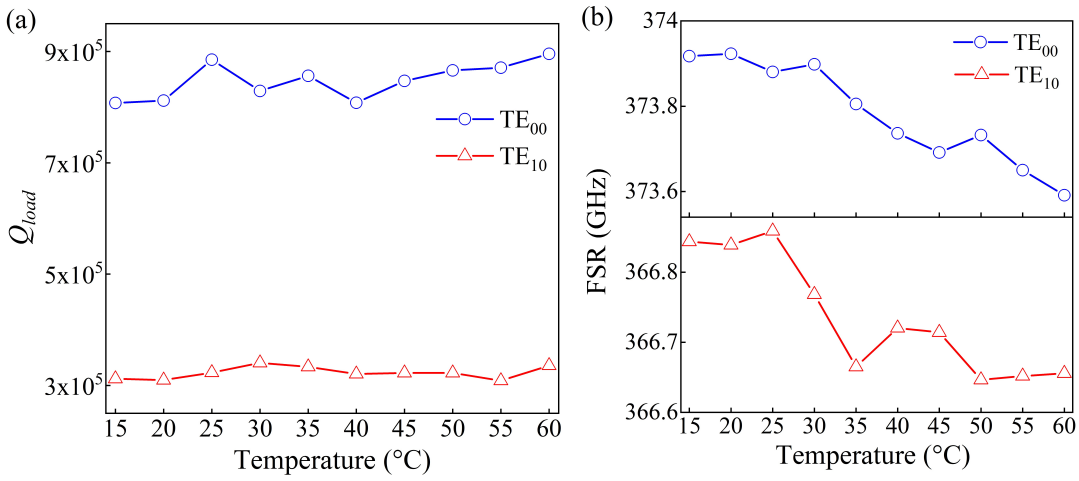


Figure 3.7: (a) Extracted loaded Q-factors of the TE_{00} and TE_{10} resonance modes versus temperatures in the region (iii), without the mode coupling effect. (b) Free spectral range (FSR) variation with temperatures, upper panel: TE_{00} polarization mode and lower panel: TE_{10} polarization mode.

3.5 Experimental demonstration of an octave-span DKS at different temperatures and tuning soliton existence range (SER)

The AlN device used here to excite the DKS using the two nearby modes, under various temperatures, is the same device as explained in section 3.2. The standard soliton setup (with TEC addition) and the procedure used is described in section 3.3. To better understand the work performed, we map the energy flow during the microcomb generation, the schematic is shown in Fig. 3.8(a). Through an evanescent coupling, the pump light is coupled into the microcavity using an integrated waveguide. The pump light circulates in the cavity and at a certain threshold energy part of the pump is converted into the microcomb lines. Both the pump and the microcomb lines have cavity insertion losses (i.e., scattering and absorption). The generated microcomb and the pump energies, after the insertion loss, is coupled out into the waveguide. To get the comb power we eliminate the pump from the microcomb lines. We demonstrate the solitons at temperatures, as low as 16°C and as high as 28°C. We sweep the laser wavelength from blue- to red-detuned position under appropriate power and tuning speed to detect the soliton step and excite the DKS. The transmission trace of all outputs in the waveguide is known as all-transmission. The transmission trace obtained by filtering the pump using a notch filter is denoted as pump-transmission and the difference of the all- and pump-transmission is known as the converted light. It is worth noting, that the obvious soliton/s step/s like structures are clearly detected for the converted light. By sweeping the laser wavelength at a relatively slow speed of 1 nm/s, Fig. 3.8(b) shows the all- and pump-transmissions (upper panel) and their difference the converted light (lower panel) traces, at the temperature of 16°C and an on-chip power of 320 mW, respectively. The SER is determined by the soliton annihilation position i.e., where the soliton power is zero. The soliton annihilation position is visible in general, but it is lacking in our study (see Fig. 3.8(b) lower panel). This we attribute to the presence of the adjacent TE_{10} mode, where the transmission of two modes merge in wide wavelength range. As from our previous work, the transmission of the resonance mode without the adjacent modes, the nonlinear red-shift to the TE_{00} modes

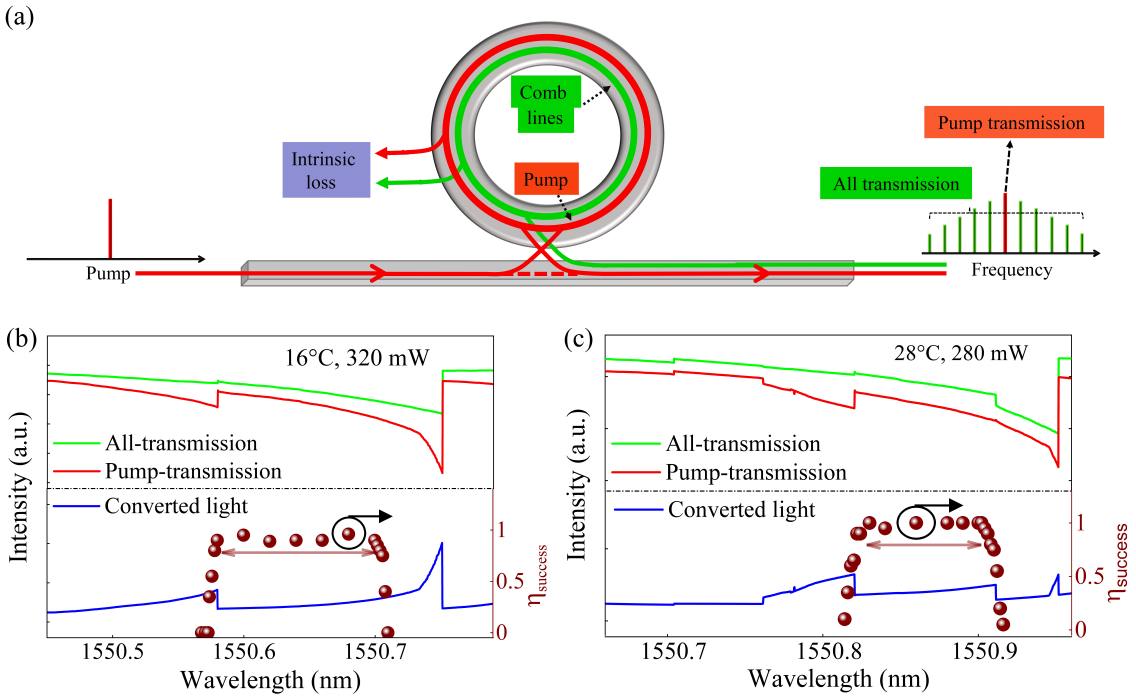


Figure 3.8: (a) Scheme of energy flow in the integrated microresonator. (b) Resonance transmissions, at 16°C with an on-chip power of 320 mW. Upper panel: all- and pump-transmissions at the laser tuning speed of 1nm/s, lower panel: converted light (the difference between all- and pump-transmissions). Soliton access possibility with brown spheres. (c) Resonance transmissions at 28°C with an on-chip power of 280 mW. Upper panel: all- and pump-transmissions at the laser tuning speed of 1 nm/s, lower panel: converted light. Soliton access possibility with brown spheres.

is 150 pm which is larger compared to the modes separation of TE_{00} and TE_{10} [57]. Therefore, with the annihilation of the soliton, the pump power equivalent to the soliton power is coupled into the TE_{10} mode. Further red-detuning the laser wavelength in the TE_{10} mode region, a breather soliton is generated (discussion below in section. 3.5.2). Moreover, a relatively strong peak on the trace of the converted light corresponds to the TE_{10} breather soliton spectrum. Next, to determine the SER for a deterministic DKS generation, we sweep the laser wavelength to different red-detuned positions on the converted light transmission. For a reliable result, we record the soliton access probability (denoted by brown spheres in the lower panel) by repeatedly (50 times) sweeping the laser wavelength and recording the soliton microcomb. The thick double arrow brown colored line depicts the SER (126 pm, ∼16 GHz) with the soliton access possible more than 80% of attempts. We increase the temperature to 28°C and repeat the similar results, as shown in Fig. 3.8(c). A clear soliton step of 80 pm (∼10 GHz) range is observed with an on-chip power of

280 mW. The SER is also confirmed by the probability measurement represented by the double arrow brown colored line, as shown in the lower panel. It is important to note that we could not access any spectrum on the TE_{10} mode at this temperature and therefore can only observe a weak peak on the converted light trace.

Figure 3.9(a) shows that at the temperatures of 16°C and 28°C, a spectrum spanning of one octave (from 1100 to 2380 nm), is directly generated at the pump laser wavelengths of ∼1550.6 and ∼1550.8 nm and using the pump powers of 320 and 280 mW, respectively. The soliton spectrum exhibits $sech^2$ shape. The $sech^2$ spectral envelop fitting, with a 3-dB bandwidth of ∼15 THz, is shown by the black dashed line. In both recorded soliton spectra, we observe DWs at 270 THz, which agrees with the simulated dispersion in section 2.3.2. In the measured spectra we also found some combs lines at the long-wavelength which we attribute to the 2^{nd}-order diffraction of the optical spectrum analyzer. To differentiate we plot the zoom-in of the lines at the long-wavelength, as shown in Fig. 3.9(b). The 1^{st}-order comb lines are marked with red circles and are equally spaced as the cavity FSR. Whereas the 2^{nd}-order lines are spaced by half of the cavity FSR and intensity of lines increases as the wavelength increases. To characterize the soliton state, the RF spectra is measured using the electrical spectrum analyzer (ESA), as shown in Fig. 3.9(c). We observe a low RF noise spectrum (green colored line), a typical signature of the single soliton, and recorded the PD-floor noise (black colored line). The mode coupling is mitigated above 50°C [as shown in Fig. 3.6(b) upper panel] therefore attempted to pump mode A. As a result, we observed only an MI comb and this we attribute to the potential change in the Q-factor, ER and separation between the pump and auxiliary resonance modes. Another limitation is that at relatively higher temperatures the coupling system has relatively poor stability and therefore prevents the generation of a single soliton.

In order to study the effect of pump power and temperature on the soliton generation and its existence (also named SER), the measured results are shown in the histogram plot of Fig. 3.10(a). We can deterministically access the DKS at a relatively slow speed of 1 nm/s with an on-chip power between 290 and 480 mW, by setting suitable temperatures. However, there is an overall decreasing trend in the SER with the increase of on-chip power which is due to the thermal effects in the microcavity. The

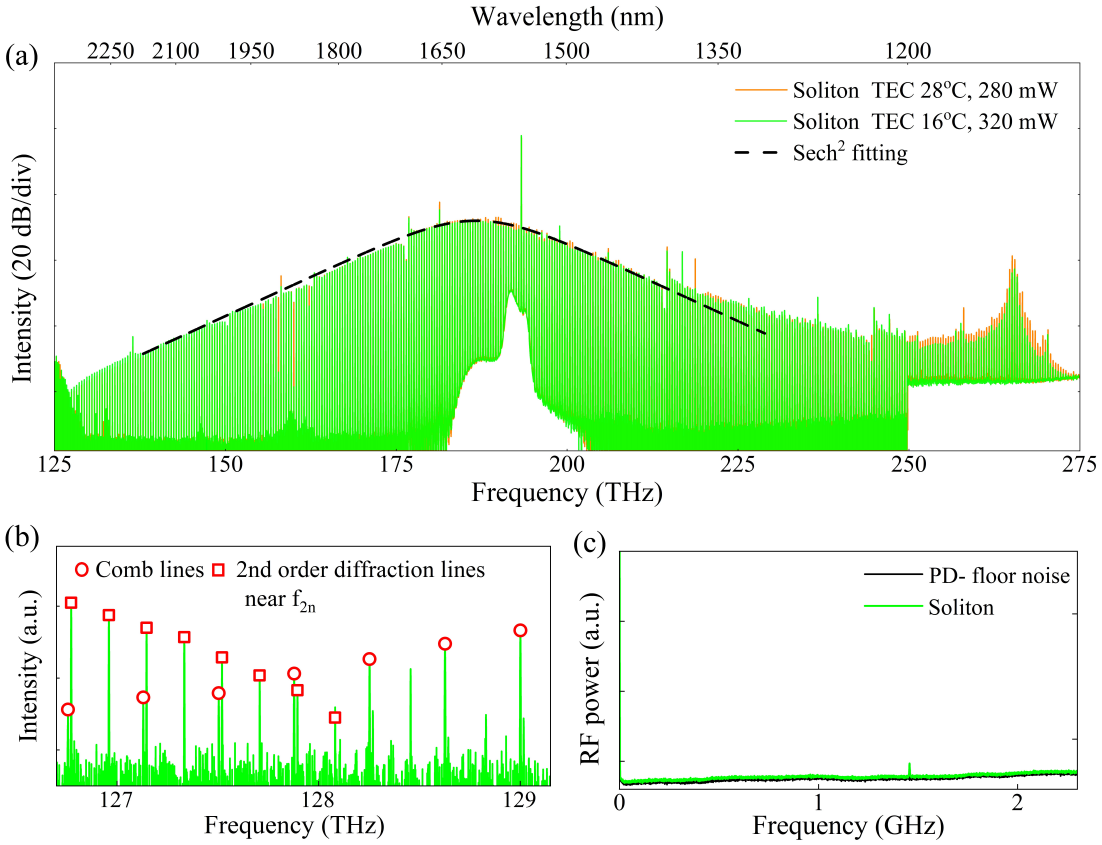


Figure 3.9: (a) Measured optical spectra of single-soliton recorded at the TEC temperatures of 16°C and 28°C, respectively. Corresponding on-chip powers are 280 mW and 320 mW. The black dashed line shows sech^2 fit. (b) Zoomed-in view of the DKS comb lines and second-order diffraction lines at the lower frequency range. (c) RF noise spectra of the single-soliton and PD noise floor.

difference traces (named as converted between all- and pump-transmission, where the widest possible SER at each discrete temperature are recorded as shown in Fig. 3.10(b). At the temperatures (ranging from 14°C to 20°C), there are no obvious soliton steps due to the lack of soliton annihilation position on the converted light traces. We used the similar repeated scanning method which is already explained above and illustrated in Fig. 3.8(b) and (c) to measure the SER. The SERs are found to be ∼15, ∼16, ∼12 and ∼10 GHz (marked with the green-colored rectangles) at the temperatures of 14°C, 16°C, 18°C, and 20°C, respectively. Clear soliton steps were observed in the temperature range of 22°C and 28°C before the power drops and are marked with the green rectangles. We cannot access the single DKS above 28°C. With the 1P2R pump strategy, the separation is significant between the two adjacent TE modes, whereas there is no significant separation change (only 3 pm) in the temperature range of 16°C to 28°C. Indeed, the crucial mode coupling

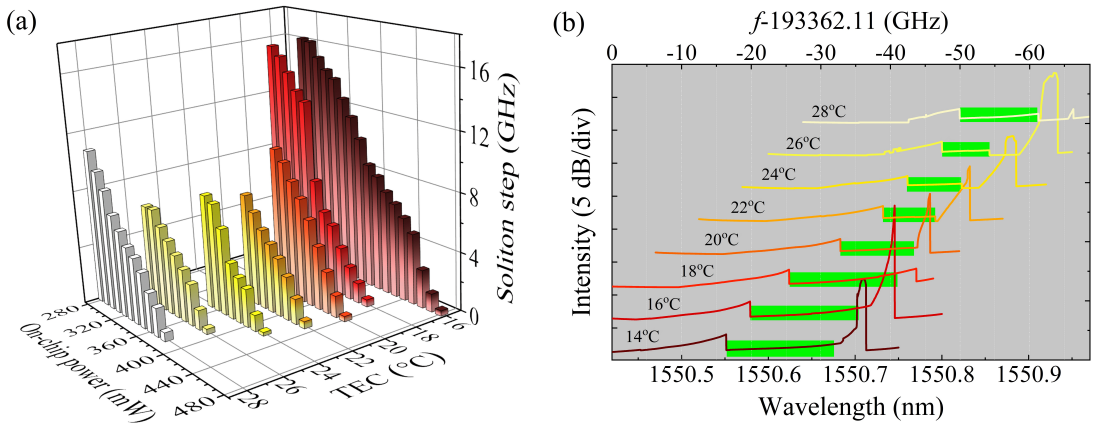


Figure 3.10: (a) 3D histogram showing the relationship between TEC temperature, on-chip power and soliton step (termed as soliton existence range). (b) Soliton existence range (SER) (marked green rectangles) at different temperatures.

between the two fundamental modes affects the separation and ER and therefore may limit the soliton generation. The effect of mode coupling on the SER is revealed at the lower temperatures where we have the widest SER when the two modes are far apart.

3.5.1 Two-solitons generation

Interestingly, we can access the two-solitons with a slight increase of temperature to 29°C. Sweeping the laser wavelength at 1 nm/s, a step-like feature is generated in the converted light trace at an on-chip power of ∼310 mW [85], plotted in Fig. 3.11(a). The height of each step corresponds to the exact number of cavity solitons (N). Here, we have a maximum of two-solitons (N=2) and single soliton (N=1), these can be deterministically obtained by stopping the pump laser wavelength on the desired step. From Fig. 3.11(a), the nonlinear mode shift is much wider which we attribute to the relatively strong mode coupling of the two fundamental modes at 29°C. It is vital to note here that the access to the two-solitons state is polarization sensitive compared to the single soliton generation. Our system can access various two-solitons plotted in Fig. 3.11(b), we have recorded the various spectra by repeatedly sweeping the laser wavelength at the stop wavelengths of 1550.832, 1550.808, 1550.834 and 1550.834 nm, respectively. All the recorded spectra broadening are in the near an octave-span range i.e., 130 to 260 THz. The obvious variation in the

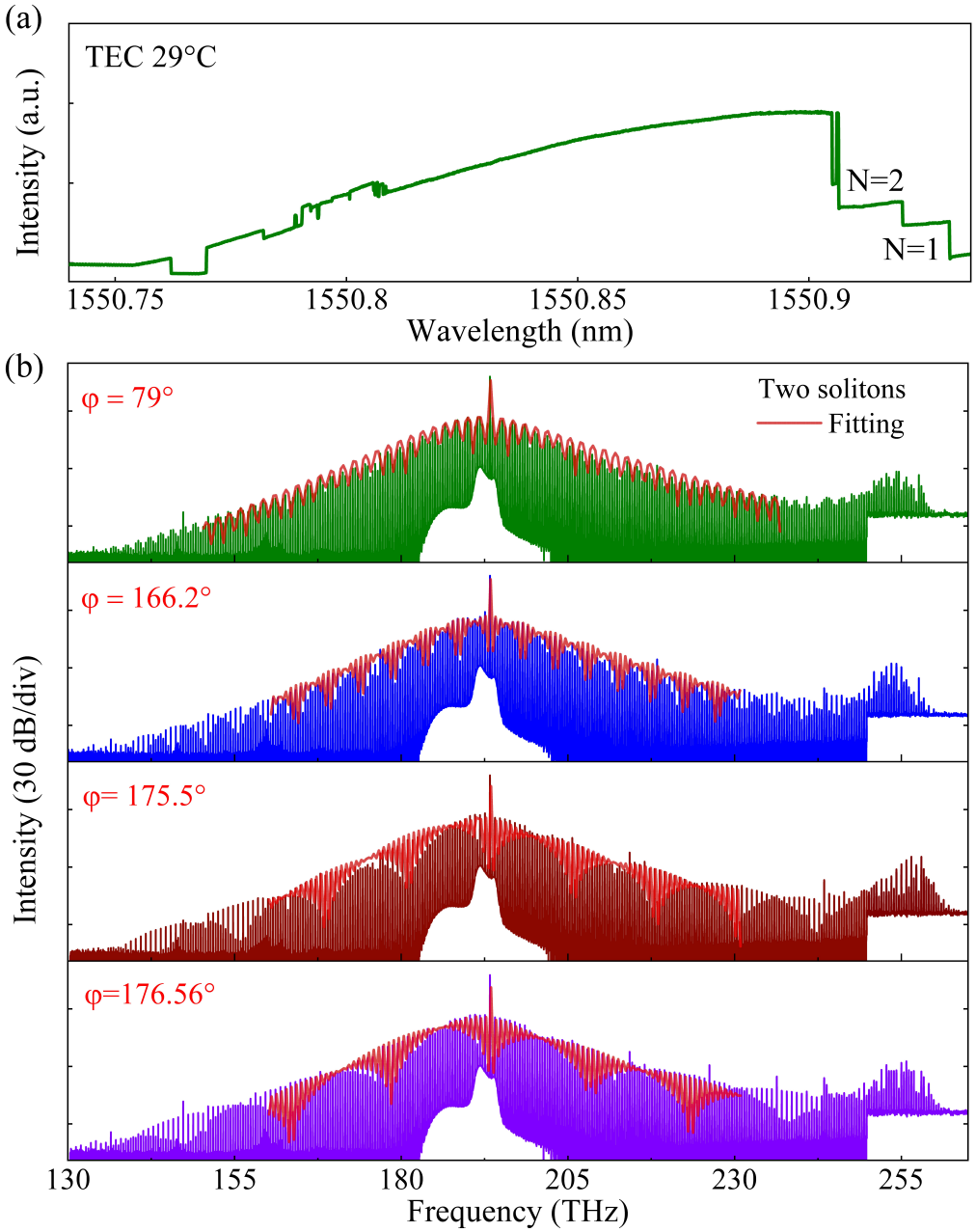


Figure 3.11: (a) Measured converted light trace (difference between all- and pump-transmissions) at 29°C with an on-chip power of ∼310 mW. (b) Measured optical spectra of two-soliton microcombs. The spectra fitting (red colored) reflects the solitons relative positions circulating in the microcavity.

profile of the two-solitons is due to spectral interference of the identical solitons on a single soliton spectrum. Obtained spectra with the relative positions (azimuthal angles) in the microcavity are confirmed by fitting the spectra with the equation (3.1) [16]

$$S^{(N)}(\mu) = S^{(1)}(\mu)(N + 2 \times cos(\mu\phi)) \tag{3.1}$$

where μ is the relative mode index to the pump mode, N is the number of circulating solitons, $S^{(1)}(\mu)$ is spectral envelope of the single-soliton and ϕ is an azimuthal angle [0,2π]. Moreover, no two-solitons are observed beyond 29°C due to the strong mode coupling as explained in the section above.

3.5.2 Microcombs from other mode families

For a more detailed and better understanding of the nonlinear dynamics for the adjacent modes, we pump the TE_{10} and TM_{00} modes at different temperatures. Firstly, pumping the auxiliary TE_{10} mode at the temperature of 28°C, we could not achieve a stable comb spectrum which is recorded in Fig. 3.12(a) (red colored spectrum). This may be due to the enhanced nonlinear resonance shift and competition from the pump mode. However, at the temperature of 16°C and the pump wavelength of 1550.62 nm, a breather soliton was generated as shown in Fig. 3.12(a). Note that a relatively slow forward tuning speed of 1nm/s was adopted, the MI comb was generated followed by the breather state. The strong and weak peaks on the converted light trace at the temperatures of 16°C and 28°C (see Fig. 3.8(b) and (c)) are well correlated here. Moreover, the breather soliton is characterized by measuring the RF noise using the ESA. Figure 3.12(b) is the recorded low noise RF spectra with the narrow spikes corresponding to the breathing states of the microcomb [58][86]. We have observed the breather solitons using the dual mode strategy in another AlN microresonator device which will be explained in the next chapter.

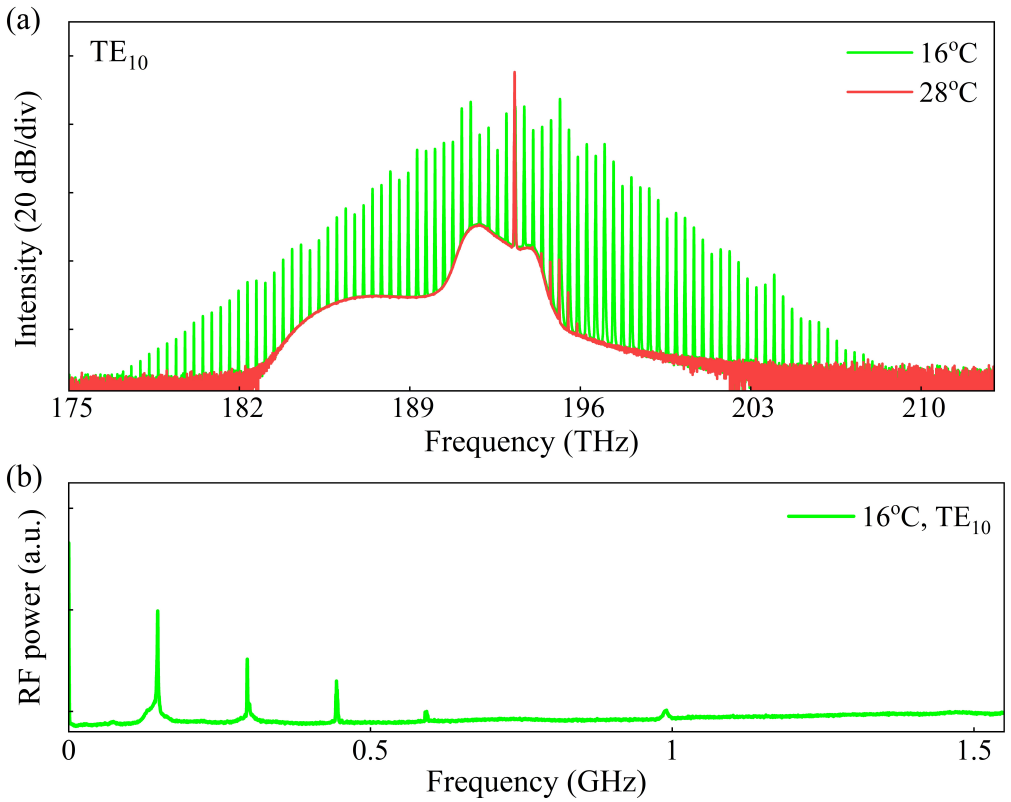


Figure 3.12: Pumping the TE_{10} mode (a) Measured spectra of breather soliton (green) at 16°C and no stable comb (red) at 28°C (b) Low-frequency RF noise spectrum corresponds to breather state.

Next, we pump the TM_{00} mode near the wavelength 1550 nm at different temperatures. Before we commence the pumping of the TM_{00} mode, we measure the transmission spectra at different temperatures [using method explained in section 3.4] and presented in Fig. 3.13(a). The insertion loss of the TM mode polarization is ∼6.8 dB, slightly higher compared to the TE polarization. Figure 3.13(b) shows the recorded spectra of the MI comb by pumping the TM_{00} at the different temperatures with a 2°C step (from 16°C to 28°C). An obvious change in the spectral broadening of the spectra was observed from ∼80 THz at 16°C to ∼130 THz at 28°C i.e., an octave-span. Coincidentally, as with the TE_{00} soliton microcomb [Fig. 3.9(a)], here at the higher temperatures a DW lines appears around 250 THz. Probably, at a higher temperature the global dispersion may change for the TM_{00} mode due to the thermo-optical effect and results in the spectral broadening. Moreover, the mode-crossing induced dispersion perturbation may possibly play a role in the spectral broadening and is now the subject of future work [81][87].

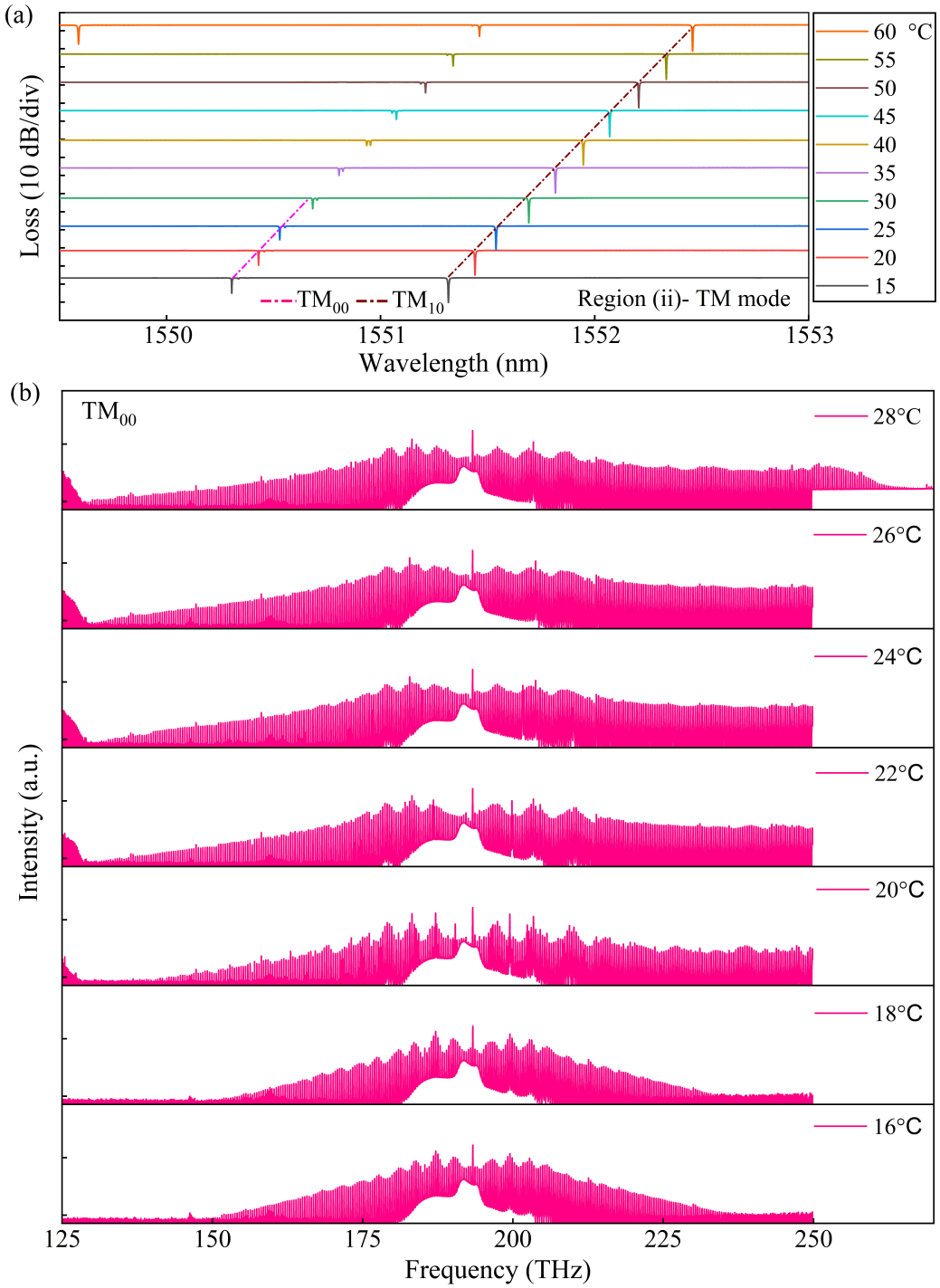


Figure 3.13: (a) Zoomed-in image of transmission spectra of TM resonances (region ii) near 1550 nm at different temperatures with a step of 5°C. (b) Measured MI comb spectra, pumping TM_{00} mode in the temperature range between 16°C to 28°C.

3.6 f_{ceo} characterization measurements

The utilization and stabilization of optical frequency microcombs that use comb lines as a time-distance ruler relies on two significant parameters, the repetition rate (f_{rep}) and carrier offset frequency (f_{ceo}) of the comb. The f_{rep} can be simply obtained by measuring the train of pulses using a suitable fast photo-diode. Whereas the f_{ceo} measurement can be carried via the self-referencing f-$2f$ technique [2]. The self-referencing technique f-$2f$ requires one octave-span microcomb spectra. Hence the achievement of the one-octave span microcomb has paved the way for a breakthrough in the development for many practical applications. Tuning the f_{ceo} close to zero with good stability is ideal and of practical significance in phase-locking [88], time-keeping applications [14] and optical frequency synthesis [15].

In this section, we study the tuning of f_{ceo} and its relative variation with the change in the temperature. As depicted in Fig. 3.14(a), the 1^{st}-order and 2^{nd}-order induced comb lines will coincide at around 2345 nm. The comb lines (circle marked) have a frequency of f_n=n$\times f_{rep}+f_{ceo}$ and second-order lines (square marked) with the FSR half of realistic comb lines, hence their frequency can be written as $f_{2n}/2$= n$\times f_{rep}+f_{ceo}/2$, where n is the comb number. By setting the OSA resolution and sampling interval at 0.01 and 0.025 nm, respectively, we measured the soliton comb spectra in a narrow wavelength region. The f_{ceo} can be calculated through the mathematical calculations as follows

$$f_{ceo} = 2 \times (f_n - f_{2n}/2) \tag{3.2}$$

Figure 3.14(b) shows the measured spectra at 16°C by increasing the laser wavelength over a 0.15 nm range. From Fig. 3.14(c), the estimated f_{ceo} at 16°C is ∼38 GHz (square marked symbols) and we observe a sudden decrease to 33 GHz due to the change of the single-soliton states [27]. Almost similar value of f_{ceo} has be reported in where an auxiliary 2 μm laser and an on-chip integrated AlN waveguide were utilized to realize self-reference [28]. Furthermore the f_{ceo} value can be adjusted by changing the TEC temperatures, as shown in the Fig. 3.14(c). We found that at 14°C the f_{ceo} has a minimum value of around 33 GHz, whereas it increases to around 45 GHz at the temperature of 26°C. In this case, the adjustment is at-

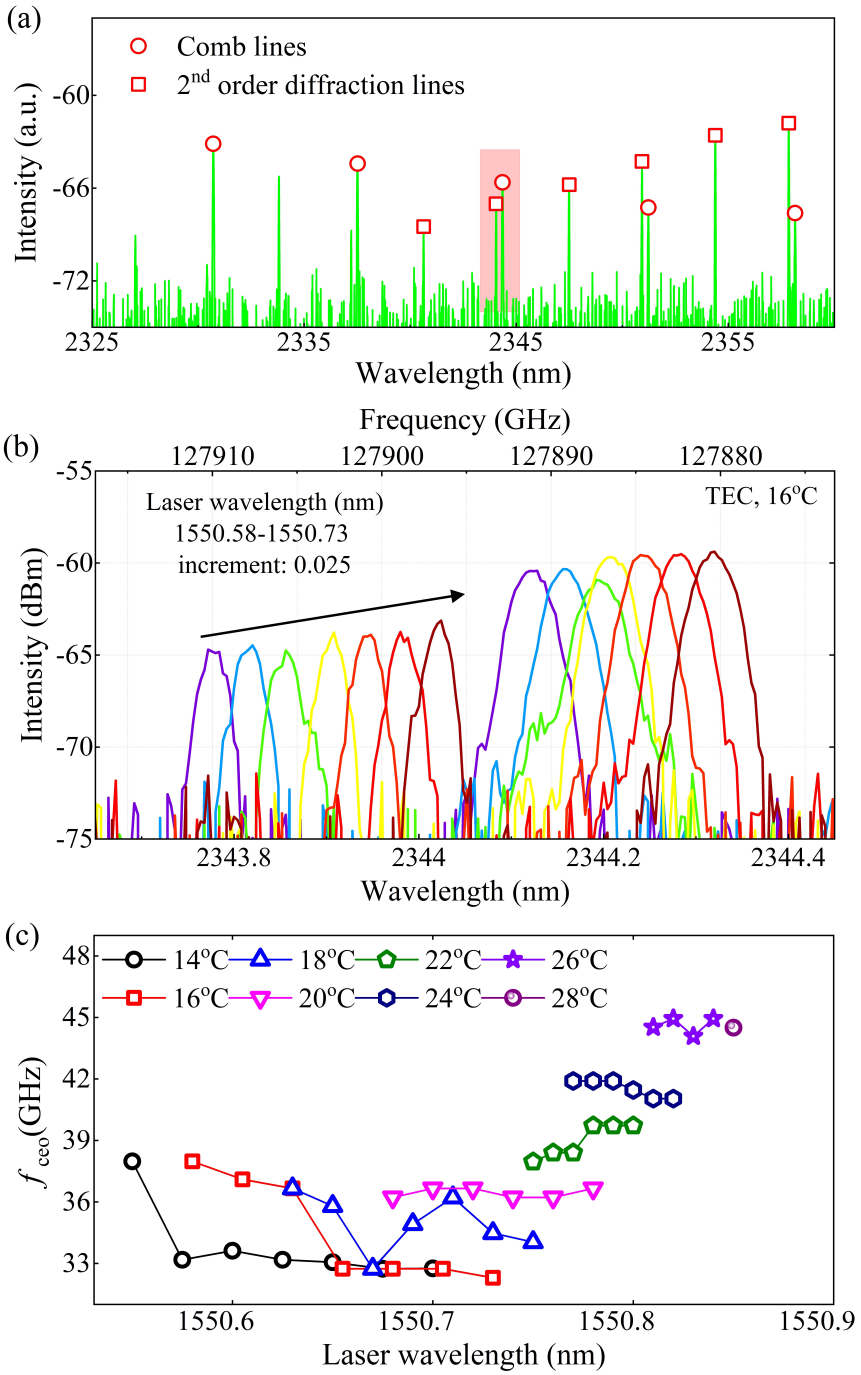


Figure 3.14: (a) Zoomed-in image of the comb-lines and second-order diffraction lines at the longer wavelength. (b) Optical spectral lines of the soliton microcombs at long wavelength by tuning the laser wavelength from 1550.58 to 1550.73 nm. (c) The variation in the carrier-offset frequency (f_{ceo}) versus the laser wavelength at various temperatures.

tributed to the modified FSR and the thermo-optical effect red shift of the resonance wavelength, which was investigated in the preliminary work [89]. Distinct from the typical f-$2f$ self-referencing schemes, the f_{ceo} calculations are purely mathematical with a relatively poor accuracy of ~1 GHz. Nevertheless, these measurements con-

tribute to understanding and estimation of the level of the offset and will play a key role in future design.

3.7 Conclusion

In conclusion, we have presented a straightforward dual mode scheme (named 1P2R) to deterministically access an octave-spanning comb in an AlN resonator. The critical requirement for the scheme is careful design and fabrication, using the COMSOL multiphysics we have simulated the two close modes by varying the ring widths. Next, we investigate the effect of temperature control on the soliton microcomb behavior. With an auxiliary resonance near the pump, an octave-spanning dissipative Kerr soliton is deterministically accessed in an AlN microresonator with an ultra-wide soliton step of ∼16 GHz at 16°C. This was achieved with a slow pump tuning speed of 1 nm/s. Using a rather simple experimental setup with a thermo-electric controller, we explore the soliton existence step versus temperature. The achieved SER is the widest step reported to our knowledge in an AlN microresonator platform.

Furthermore, we explored the mode coupling significance in our study. We observed an avoided mode crossings between TE_{00} and TM_{00} at higher TEC temperatures, which can hinder the soliton access from the pump mode but enhance the bandwidth of the microcomb from the TM_{00} mode. The breather soliton was generated from the auxiliary high-order mode at low temperature due to a large mode separation. Near octave-spanning two-solitons are also demonstrated in the resonator with thermal tuning. Thermo-optical changes and mode coupling alter the dispersion profile of the TM_{00} mode and significantly enhance the comb bandwidth to an octave-spanning range at relatively high temperatures. Hence, mode coupling seems to be a very useful tool for soliton generation and can be further explored by designing microcavities with engineered precise positions to achieve mode coupling. Finally, we can calculate and estimate the f_{ceo} for our device. We can potentially tune the f_{ceo} and can reduce by decreasing the temperature.

Further studies of temperature control are of interest since this material and its sapphire substrate are of high thermal conductivity. Our work shows that AlN is

another potential platform for soliton generation and control building on the outstanding work done on the silicon nitride platform.

Chapter 4

Breather soliton and soliton crystals in AlN microresonators

In this chapter, diverse soliton microcombs in an AlN microresonator are presented. We observe a near-octave-spanning breather soliton, single soliton and breathing perfect soliton crystals (BPSCs). The results obtained are from a microresonator whose geometry provides anomalous dispersion. These novel soliton states were experimentally demonstrated along with numerical simulations. The experimental and numerical simulation results are in good agreement.

4.1 Introduction

Kerr soliton microcombs are phase synchronized, ultra-short, robust pulses and can retain their shape in microresonators for many hours. The double-balance between Kerr non-linearity and dispersion as well as cavity losses and parametric nonlinear gain pave path to access the soliton state [90][53]. The loss in the cavity and gain from the parametric nonlinear four-wave mixing (FWM) make it a dissipative system, with solitons known as dissipative Kerr solitons (DKS). The demonstration of the DKS in microresonators and the achievement of broad spectral width due to soliton-induced Cherenkov radiation makes them a hot research topic in the field of nonlinear photonics with numerous applications [16]. In recent years, dynamic soliton microcomb states have been reported due to the researchers intensive work and interest in studying the physics of frequency comb generation. Beside the bright single soliton, other soliton forms include dark solitons [91], dark-bright solitons [92], soliton molecules [93], Stokes solitons [94], soliton crystals [95] and breather

solitons [86][96][97][98]. All these reported intracavity coherent solitons forms are locked whereas breathing soliton states have intrinsic dynamic instability (periodic oscillations) in time or frequency domain. The period of oscillation resembles any physical system oscillations which returns to its initial positions after one complete cycle. The intrinsic dynamic instability is induced due to unbalanced dispersion and Kerr non-linearity together with cavity loss and gain. Due to the imbalance that led to the imbalance, instabilities can eventually prevent the single soliton access. The breather solitons are excited in microresonators under the intrinsic dynamic instability [86] in the single soliton region and in avoided mode crossings (AMXs) [96]. However, in both phenomena the breather states can be accessed by the detuning cavity resonance between the modulation instability (MI) comb and single soliton region [99]. The narrow existence region of breathing solitons and it significance in microcombs applications attracted significant research. Therefore, to our knowledge the dynamic breather solitons have been reported in integrated microresonator platforms of silicon (Si), silicon nitride (Si_3N_4) and crystalline MgF_2 whispering gallery mode resonators [86][96][99].

The study of novel breather solitons, a near-octave-spanning single soliton and BPSCs are demonstrated here in AlN based integrated microresonator platform. In the following sections, we will present the device characterization results, experimental observation of breather solitons, interplay between breathers and the stimulated Raman scattering Stokes (SRS) line. We also discuss the route to access the near-octave-spanning coherent single soliton. Moreover, to further study breathing soliton states we explore another device with similar geometry. The experimental results are presented together with the numerical simulations of Lugiato-Lefever equation (LLE) and COMSOL multi-physics [100][101]. Finally, we demonstrate the soliton crystals using a resonator with same parameters of cross-section used for the breather solitons section but with slight change in the integrated bus waveguide. Consequently, AMX occurs in the spectral region of the telecommunications C-band and helps to generate perfect soliton crystals. The detailed experimental demonstration of novel near-octave-spanning BPSCs and characterization will be discussed.

4.2 Device characterization

In this work we employ a 60-μm-radius AlN-on-sapphire microring resonator cladded with silicon dioxide (SiO_2). Standard photo-lithography process was used for fabrication, the details are explained in chapter 2 section 2.2 [36]. To remove the high order modes, a rather narrow micro-ring waveguide with the cross-section of $\sim$2.29$\times$1.2 μm^2 (W$\times$H) was employed. A microring with a gap of $\sim$0.5 μm is integrated with a bus-waveguide tapered from 1.11 to 4 μm.

Figure 4.1(a) illustrates the experimental setup used to test the performance of the AlN device and measure the resonance characteristics such as Q-factor, ER and coupling loss. Using the technique explained in section 3.2, we record the transmission spectrum of the transverse electric (TE) polarized light over the range of 20 nm as shown in Figure 4.1(b). In the case of TE polarization, the design can support the two TE modes i.e., fundamental (TE_{00}, blue colored) and first order (TE_{10}, magenta colored) which is consistent with the simulation results in chapter 2 section 2.3.2. From the measured transmission spectrum the optical insertion loss is $\sim$6.4 dB, mainly from the coupling loss at facets of the waveguide. Hence the coupling loss of the device can be reported $\sim$3.2 dB per facet. Furthermore, the polarization modes can be distinguished by measuring the free spectral range (FSR) of resonance modes [102]. The measured FSRs of TE_{00} and TE_{10} resonance modes at around 1550 nm are about 375 GHz and 364 GHz, respectively. From the transmission spectrum the resonance modes FSR changes due to dispersion. We can achieve the two nearby modes at around $\sim$1556.68 nm, zoomed-in image is shown in Fig. 4.1(c). The Separation between the two adjacent modes, TE_{00} (at around 1556.68 nm) and TE_{10} (at around 1556.69 nm), is 12 pm ($\sim$1.5 GHz). The Lorentzian fitting is used to measure the linewidth and to extract the loaded quality (Q_L) factor. The 3-dB linewidth of the TE_{00} and TE_{10} modes are $\sim$334 MHz and $\sim$348 MHz and corresponding loaded quality (Q_L) factors are $\sim 5.9\times10^5$ and 5.5×10^5, respectively. As shown in Fig. 4.1(d), from the extracted loaded Q-factors, at around 1556.68 nm the two Q_L factors approach each other indicating weak coupling between the two transverse resonance modes. Owing to the weak coupling effect at around 1556.68 nm the intrinsic Q for the TE_{00} mode is calculated near 1550 nm. Taking an over-

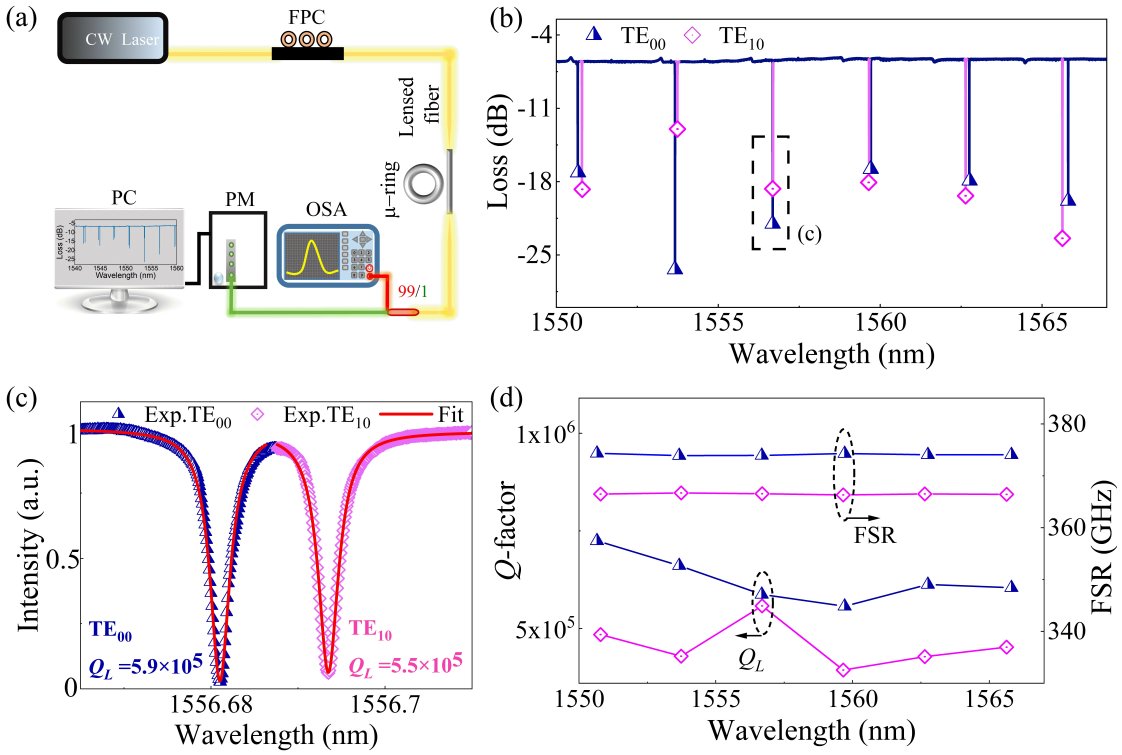


Figure 4.1: (a) Experimental setup used for device characterization. CW, continuous wave laser; FPC, fiber polarization controller; OSA, optical spectrum analyzer; PM, power meter. (b) Transmission of the device with TE modes polarization. (c) Two fitted adjacent modes at around ∼1556 nm. (d) Measured FSRs and extracted Q_{load} for the TE resonances in the range 1550-1570 nm.

coupling condition into account, the extracted Q_{int} is 1.1×10^6 with a propagation loss of 0.33 dB/cm.

4.3 Experimental demonstration of breather solitons

To start the discussion of the experimental demonstration of breather solitons, we first calculate the parametric threshold power (P_{th}) of the device. The appropriate threshold power is vital to access stable microcombs. The input threshold power for parametric oscillation can be estimated using the relation [103]

$$p_{th} = 1.54\frac{\pi}{2}(\frac{Q_c}{2Q_L})\frac{n^2V_{eff}}{n_2\lambda Q_L^2} \tag{4.1}$$

Where Q_c and Q_L are the coupling and loaded Q-factors of the microresonator, respectively. n is the refractive index, V_{eff} is simulated effective-mode volume which

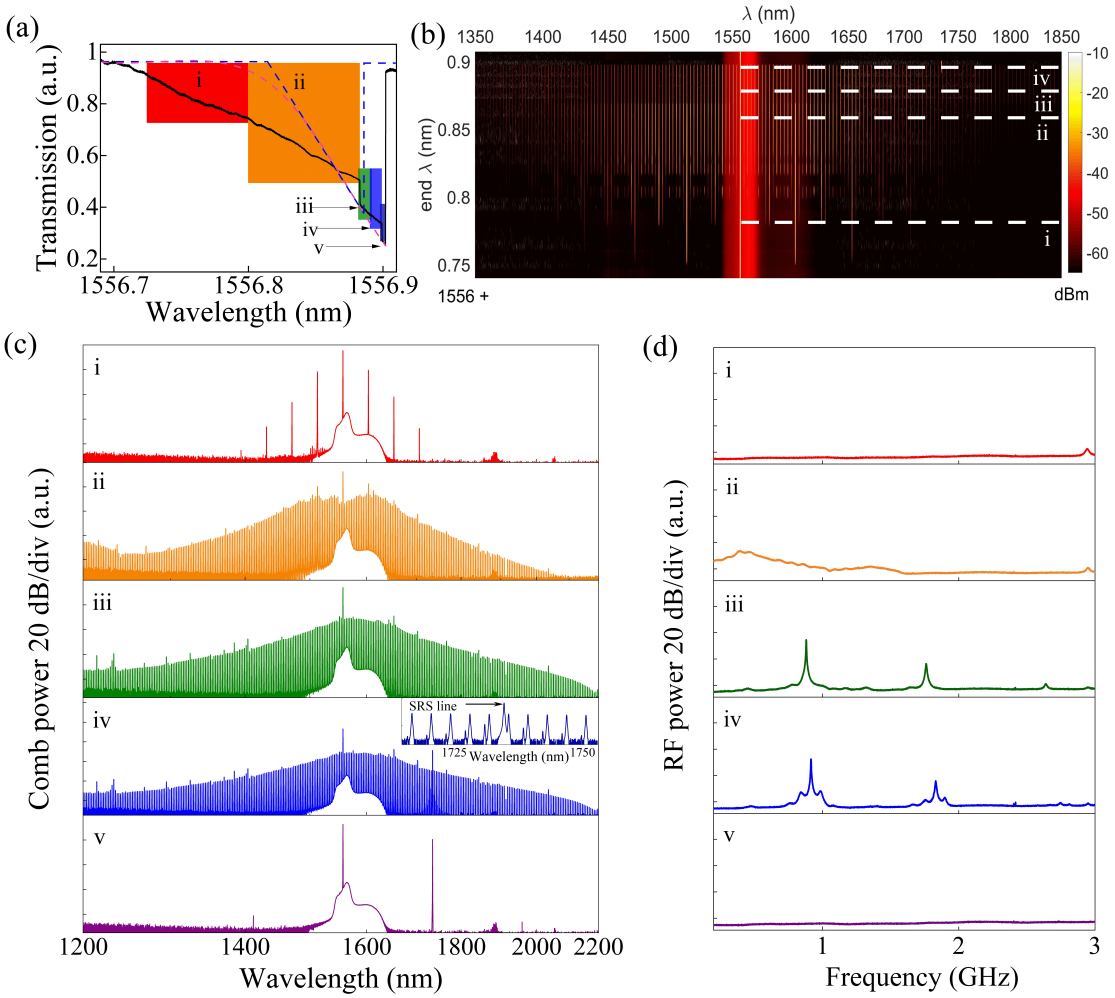


Figure 4.2: (a) Two adjacent modes of resonance transmission at 250 mW and laser sweep speed of 1 nm/s. The different color shadings on the transmission correspond to microcomb states from (i)-(iv). (b) Microcomb evolution map. (c) Measured optical-spectra.(i) Multi-FSR primary comb (ii) MI comb (iii) Breather state (iv) Breather soliton with SRS Stokes line and (v) is the stokes emissions when the laser wavelength stop position is on the TE_{10} mode. Inset of state (iv) is the zoomed-in image of the SRS Stokes and microcomb lines. (d) Recorded RF noise spectra of corresponding microcomb states (i)-(v).

is calculated using COMSOl. n_2 is the second non-linearity and λ_p is the pump wavelength. For our AlN device, the simulated V_{eff} is ~674 μm^3 at the pump wavelength near 1556 nm (TE_{00}). The estimated threshold power of TE_{00} mode is ~40 mW based on refractive index (n≈2.1), Kerr coefficient $n_2 = 3.5\times10^{-19}$ m^2W^{-1} [104] and corresponding Q-factors (Q_c/ Q_L) are $8.4\times10^5/5.9\times10^5$, respectively.

The experimental setup and procedure used for the demonstration of breather solitons resemble the standard soliton setup and details described in chapter 3 section 3.3. To access the breather and/or single soliton, we use our two near-mode strat-

egy [27][22]. The adjacent modes (see Fig. 4.1(c)) are pumped at 250 mW. The TE_{00} mode is used as pump mode whereas TE_{10} mode is an auxiliary resonance. We sweep the laser wavelength across the resonances at a sweep speed of 1 nm/s from lower to higher wavelength until it is off-resonance. Figure 4.2(a) shows the recorded normalized triangular-shaped transmission trace with several features including a prominent soliton step. During the sweep, we see the normalized pump transmission start to decrease from 1 since the light is coupled into the (TE_{00}) mode and it red-shifts due to thermal effects in the microresonator. On further detuning, for the resonance wavelength, there is a sudden reduction in the power and an obvious step appears. The TE_{00} blue shifts and the rest coupling power is compensated by the auxiliary TE_{10} mode and leads to access of the breather or single soliton step. We sweep the laser wavelength until it is off-resonance and back to 1 as shown in Fig. 4.2(a). The colored shaded regions on the transmission trace correspond to the evolution of different comb states. Here we observed five different comb states i.e., (i) primary comb, (ii) modulation instability (MI) comb, (iii) breathing soliton without stimulated Raman scattering (SRS), (iv) breathing soliton with SRS, and (v) SRS, at red-detuned stop positions. Figure 4.2(b) is the evolution map of the comp spectra plotted by sweeping the laser to different detuning positions. The marked white dashed lines correspond to the five different states marked on the transmission trace in Fig. 4.2(a). Figure 4.2(c)-(d), shows the recorded comb spectra and their corresponding RF noise spectra using the OSA and ESA, for these five comb states. It is important to note that during measurements all the recorded comb states were repeatable, stable and can last for hours. Explicitly looking into the comb spectra evolution, when the intracavity power reaches a certain threshold, initially a primary comb with few side bands appears due to the strong third order Kerr non-linearity (χ^3) FWM. At a laser stop wavelength of 1556.77 nm the first parametric side-band appears at N=15 cavity FSRs ($N\times$FSR), as shown in Fig. 4.2(c) state (i). The low-frequency RF noise spectrum in Fig. 4.2(c) state (i) is attributed to the generation of multi-FSR primary comb lines. By further increasing laser wavelength to 1556.86 nm a single-FSR modulation instability (MI) comb is generated with a broad RF noise spectrum (shown in Fig. 4.2(c) state (ii)). We can access the breather soliton (Fig. 4.2(c) state (iii)) in the step-like region by setting the stop

wavelength of 1556.87 nm. The range of the recorded spectrum is from 1200-2200 nm but on the lower wavelength end it can extend beyond 1200 nm, which is beyond our OSA range. The breathing state can deterministically be accessed at around the stop wavelength in the breathing region. Compared to the primary and MI comb states the breather states (iii) and (iv) are red-shifted from the center pump and attributed to the Raman-induced frequency shift [105][106]. The RF noise spectrum in the state (iii) drastically decreases and narrow sharp tones appear i.e., characteristics of the breathing state of a microcomb [86][96]. Further increments on the laser pump wavelength toward the red-detuned position and selecting the stop wavelength of 1556.89 nm can generate the breather together with SRS. The coexistence of SRS can be confirmed by the inset image in the state (iv) of Fig. 4.2(c). We presume the existence of SRS is from the auxiliary TE_{10} mode and worth to mention that comb lines spacing near the SRS is smaller compared to the breather soliton. It is worth noting that the coexistence and interplay between the SRS and FWM have been investigated and reported in previous studies [104][107][108]. The RF noise level in Fig. 4.2(d) state (iv) is low but slight broadening in the sharp tones is observed which we attribute to the coexistence of SRS together with breathing soliton. The breather soliton disappears, and Stokes exists on its own by tuning the pump laser wavelength to 1556.9 nm before going off the cavity resonance. The existence of third-order nonlinear Stokes line corresponds to phonon E_2 high with a shift of 656 cm^{-1} ($\sim$19.5 THz) [109]. The existence of third-order nonlinear SRS line in the higher order (TE_{10}) mode and lack of nonlinear competition in our device is confirmed in the section below.

4.3.1 Pumping other TE resonance modes

To better understand how the dual-mode separation affect the comb behavior, we also pump the other three groups of TE modes near the pump mode $\sim$1556 nm, i.e., $\sim$1553 (orange colored), $\sim$1559 (green colored) and $\sim$1562 nm (blue colored), as shown in Fig. 4.3(a). The on-chip power of is fixed at 250 mW. The recorded transmission traces of these three groups are shown in the Fig. 4.3(b). For the group (i), TE_{00} mode is at the left and TE_{10} is at right side. While in the groups (ii) and (iii), the resonances wavelengths of the TE_{10} modes exceed and that of TE_{00}

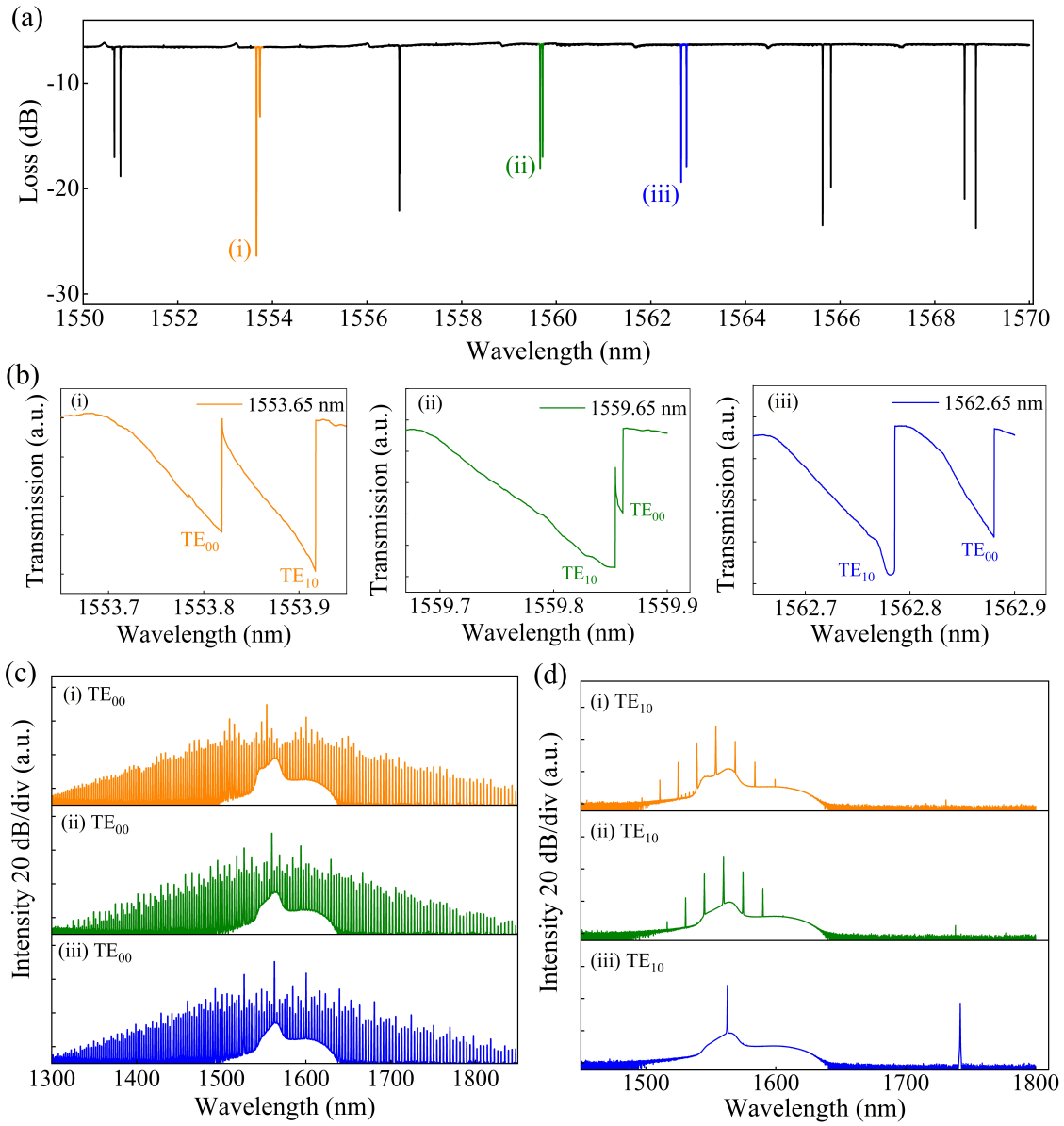


Figure 4.3: (a) Transmission spectrum of TE polarization modes in the range 1550-1570 nm, at power of $\sim$ 40 μW. The three sets (i)-(iii) of pumped resonances are marked with orange, green and blue colors.(b) Transmission traces of resonances (i)-(iii) at a pump power of 250 mW (c) Measured Kerr microcomb optical spectra (range 1300-1850 nm) by pumping the TE_{00} modes of resonance wavelengths in (b). (d) Measured optical spectra of Kerr microcomb primary and/or SRS Stokes lines by pumping the TE_{10} resonance modes in (b).

modes due to the different FSRs of the two-mode families. The transmission traces are in good agreement with measured transmission at low power (see Fig. 4.1(b)). Corresponding comb spectra of both TE_{00} and TE_{10} are recorded and shown in Fig. 4.3(c) and (d). From Fig. 4.3(c), by pumping the TE_{00} modes in all the three groups of resonance (i)-(iii) we can only generate broad MI comb irrespective of blue- or

red-detuned positions of the modes. The suitable Q-factor and sufficient nonlinear coefficient results in the generation of broad Kerr combs. Furthermore, we scan the laser wavelength across the TE_{10} mode of the specific groups of resonances. We observe primary comb (with few comb lines) and/or SRS Stokes lines, as shown in Fig. 4.3(d). We can confirm that there is no nonlinear competition between the two close modes and the SRS line in Fig. 4.3(d) state (iv) and (v) is from the TE_{10} resonance mode.

4.3.2 Breather and single soliton generation with various detuning speeds of the laser wavelength

We next explore the technique to access the stable soliton microcomb. When the microring resonator (MRR) is pumped with high power, the cavity heats up and the MRR is driven out of thermal equilibrium. To excite a coherent single soliton in the MRR it is crucial to achieve a thermal equilibrium in microcavity. Therefore, a lot of extraordinary work has been done to study the significant parameters to achieve microcavity thermal equilibrium and access the DKS [90][53][16]. Beside device threshold power and high Q-factor it is vital to have appropriate pump laser scan speed [90][96][70]. The pump laser scan speed is the speed of tuning the laser wavelength across the resonance from certain start to stop wavelength positions. This technique was adopted in our experiment by setting the CW laser output in the continuous sweep mode.

Figures 4.4(a) and (b), are the recorded optical and corresponding RF noise spectra at various pump laser scan speeds. It is important to note that the pump power is kept constant in these recorded results i.e., 250 mW. We scan the laser wavelengths with the different stop positions of 1556.865 and 1556.845 nm, keeping laser scan speed of 2 and 6 nm/s, respectively. We can deterministically access the breathing solitons (as shown in two upper stacks of Fig. 4.4(a)). The breather states are confirmed by the RF low noise spectra with narrow sharp peaks. The breather spectra are broad which can go below 1200 nm on the low wavelength and up to 2200 nm on the long wavelength range. Moreover, by increasing the scan speed to 10 nm/s and laser wavelength stop position of 1556.805 nm, we can successfully access the coherent single soliton microcomb [see lower stack of Fig. 4.4(a)]. It is important

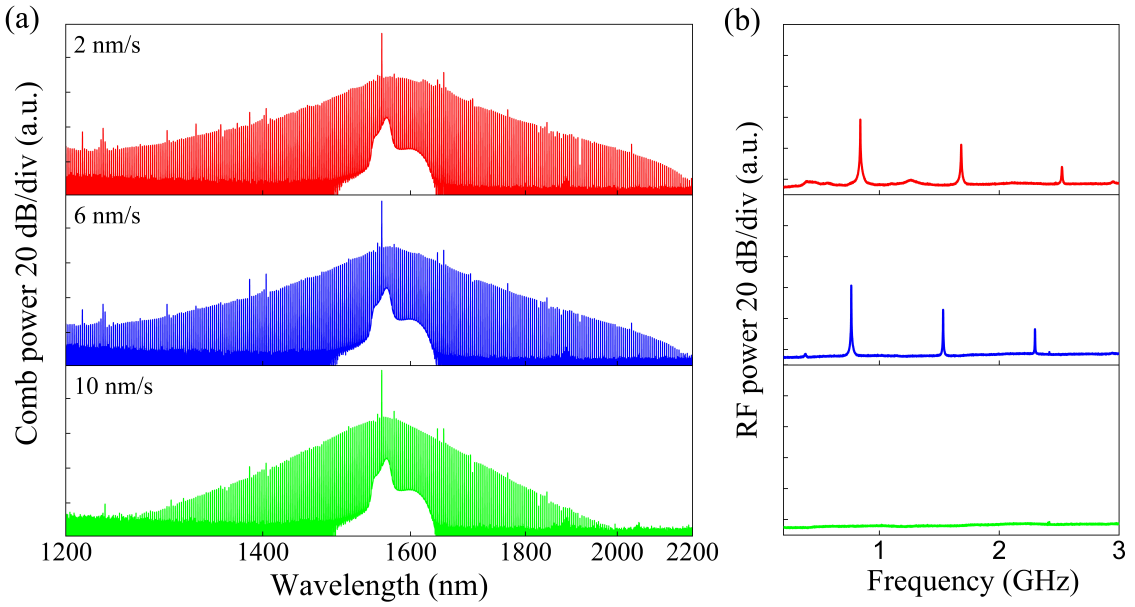


Figure 4.4: Experimental demonstration of breather and single soliton microcombs. (a) Optical spectra of breather and single soliton microcombs at fixed power of 250 mW and various laser sweep speeds of 2, 6 and 10 nm/s.(b) Corresponding RF noise spectra.

to note that owing to the presence of the auxiliary mode, the laser scan speed is relatively slow compared to thermal relaxation in the cavity and an optimized laser scan speed is required to achieve thermal equilibrium [90]. The fast laser scan speed potentially helps to overcome the SRS and access the stable single soliton. The stable soliton microcomb can be confirmed by the disappearance of narrow peaks and low RF noise in the lower stack of Fig. 4.4(b). Finally, we explore to the limits of the laser scan speed and increase the pump power. We used a relatively high power of 400 mW and scan speed of 14 nm/s. This led us to access beyond 4/5 of an octave-span single soliton. From Fig. 4.5(a), the soliton microcomb ranges from 1200 to 2100 nm i.e., 108 THz span. The Fourier-transform of soliton spectrum has sech^2 pulse shape and is one of the soliton characteristics [90]. We fit the soliton with sech^2 envelope with a 3-dB bandwidth of 9 THz, as shown with black dashed line in Fig. 4.5(a). The low-level RF noise spectrum is a characteristic signature of coherent soliton microcomb. Figure 4.5(b) shows the measured RF noise spectrum (resolution bandwidth RBW 1 MHz) of the soliton microcomb with the PD floor noise.

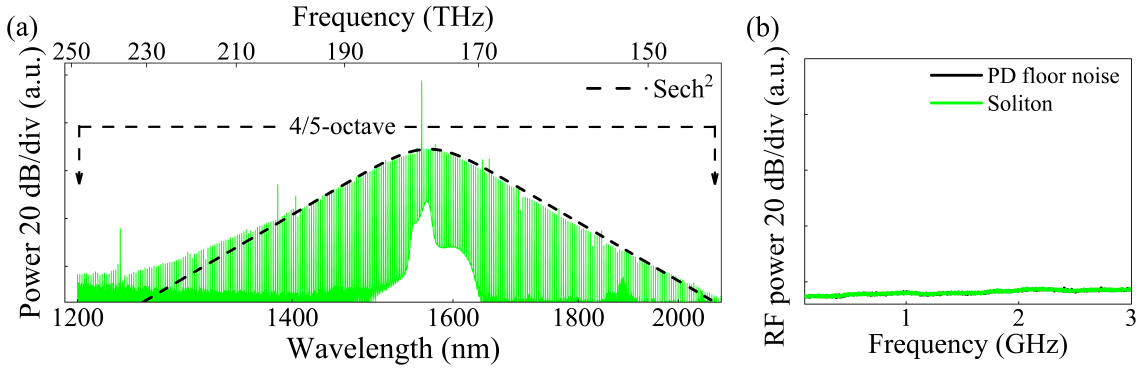


Figure 4.5: Experimental demonstration of 4/5 of an octave-spanning single soliton microcomb. (a) Optical spectra of a single soliton microcomb (1200-2100 nm) at 400 mW pump power and fitted with a sech^2 black dashed line. (b) Corresponding recorded RF noise spectra of the soliton microcomb together with PD floor noise level.

4.3.3 Breather and single soliton in TE_{10} mode

To study further the breather and single soliton generation in our AlN MRRs, we explored various resonance modes with high Q-factor and near-zero anomalous dispersion. In this section, we discuss more experimental results of breather and stable soliton microcombs obtained by pumping the TE_{10} mode. The device employed here is from a different chip having the same cross-sectional (2.29 $\times$ 1.2 μm^2) parameters and radius (60 μm) as explained in section 3.2. To distinguish the resonance modes and extract the Q-factor, a low power (-14 dBm) and high resolution 0.1 pm (within 10 nm range) transmission spectrum is measured and plotted in Fig. 4.6(a). From the transmission spectrum, the TE_{00} (marked with blue colored triangle) and the TE_{10} (marked with magenta colored triangle), respectively. The TE_{10} mode at $\sim$1563.93 nm, was pumped as high as 450 mW, breather and single soliton microcombs with low RF noise spectrum were observed. The TE_{10} mode has FSR of $\sim$366 GHz and relatively high intrinsic Q-factor i.e., 1.05 $\times$ 10^6.We used the same technique of tuning the laser wavelength from the blue- to red-detuned position [see section 4.3] to access the different microcomb states. The crucial difference here is that we used the fine-tuning (manual) technique. Four different microcomb states

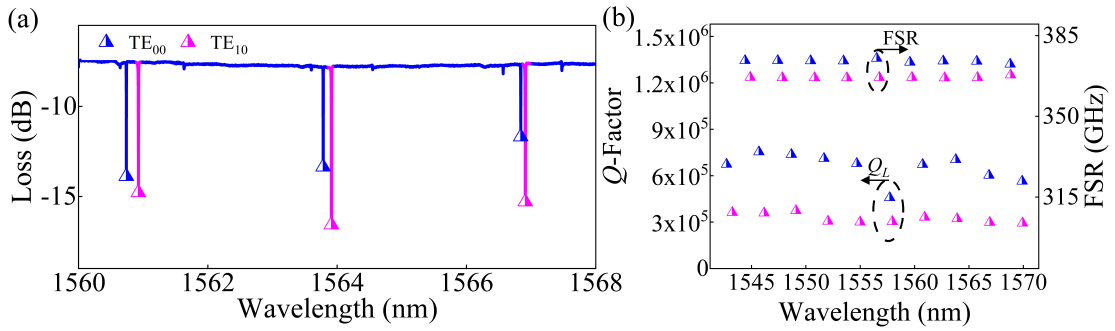


Figure 4.6: (a) Transmission spectrum of the TE polarization mode of the second device in the range 1560 to 1568 nm at ∼40 μW power.(b) Measured FSRs and extracted Q_L-factors in the 1540-1575 nm range.

(i)-(iv) and their corresponding RF noise spectra are plotted in Fig. 4.7(a) and (b). A multi-FSR (N=5) N×FSR apart, side-bands of the primary comb are generated and recorded (see in Fig. 4.7(a) state (i)) at laser stop wavelength position of 1564 nm. An MI comb is generated at a further red-detuned position of 1564.06 nm. A high RF noise level in state (ii) of Fig. 4.7(b) confirms the unlocked microcomb lines. Upon careful laser tuning to a stop position of 1564.08 nm can lead to the access of the breather soliton microcomb. This is also confirmed by the drastic reduction of the Rf noise level and narrow peaks as shown in the state (iv) of Fig. 4.7(b). Finally, an increase to the red-detuned position of 1564.11 nm of the pump laser wavelength can give us stable soliton state. The soliton spectrum can exist in the range from ∼1425 to 1750 nm. The soliton state is verified by the low ESA noise spectrum (see Fig. 4.7(b) state (iv) with the disappearance of the sharp narrow peaks.

Cavity dispersion is one of the vital and basic parameters for the microcomb generation [90][53]. Kerr microcomb generation critically depends on near-zero anomalous dispersion i.e., D_2>0. The calculated (D_{int}) profile for TE_{10} mode is plotted with red solid line in the bottom stack of Fig. 4.7(b). Hence, the extracted values of $D_1/2\pi$ is ∼368 GHz, $D_2/2\pi$ is 37.3 MHZ and β_2 is -0.31 ps^2/m using center frequency of 192.6 THz. The extracted value of β_2<0 confirms the pump is in an anomalous dispersion regime.

Next, based on the calculated dispersion the numerical simulation was done to reproduce the experimental results and to better understand the soliton dynamics.

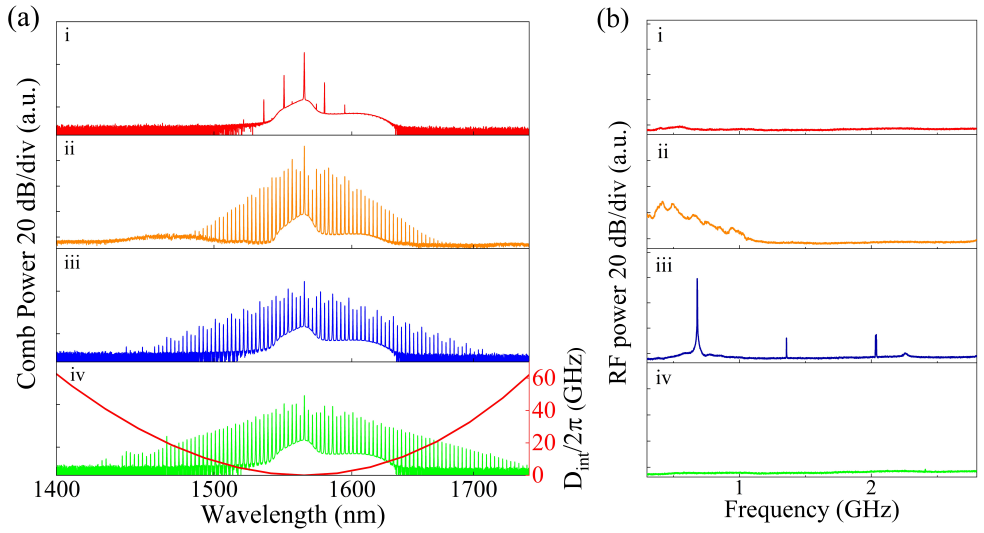


Figure 4.7: Experimental demonstration of breather and single soliton microcombs in the TE_{10} mode.(a) Measured optical spectra at 400 mW (i) primary, (ii) MI, (iii) breather soliton, and (iv) single soliton microcombs, using manual tuning. The red solid line in the lower panel (state iv) is the D_{int} simulation of the TE_{10} mode.(b) Corresponding RF noise spectra (i)-(iv) of states in (a).

We use the LLE model based on a combination of coupled mode theory and the nonlinear Schrödinger equation. To analyze and verify this behavior in our AlN resonator the LLE equation is described as [110][111]

$$t_R \frac{\partial E(t,\tau)}{\partial t} = \left[-\alpha - i\delta + iL \sum_{k\geq 2}^{n} \frac{\beta_k}{k!} \left(i\frac{\partial}{\partial \tau} \right)^k + i\gamma L \left| E \right|^2 \right] E(t,\tau) + \sqrt{\theta} E_{in} \quad (4.2)$$

where E(t,τ) is a slowly varying field envelope, t is the slow evolution time, and τ is the fast time related to cavity group velocity. t_R, α, δ, L, β_k,γ correspond to cavity round-trip time, cavity loss per round-trip time, pump cavity detuning, cavity length, k_{th} order Taylor expansion dispersion coefficient and nonlinear coefficient, respectively. The nonlinear coefficient is defined as $\gamma = n_2\omega_0/cA_{eff}$ with n_2 as nonlinear refractive index, ω_0 is the pump frequency, c is the speed of light and A_{eff} is the effective modal area obtained from FEM simulation. Figure 4.8 shows the simulation results obtained using the TE_{10} resonance mode. The parameters such as ω_0 (~191.7 THz), Q_{int} (~1.05×10^6),γ (0.72 $W^{-1}m^{-1}$) and ER (~ 8 dB) used for the simulations corresponds to our AlN device. Figure 4.8(b) shows the intracavity waveform evolution (top) and pump power versus detuning (bottom). The red dashed line marked in iii corresponds to the breather state, and we can

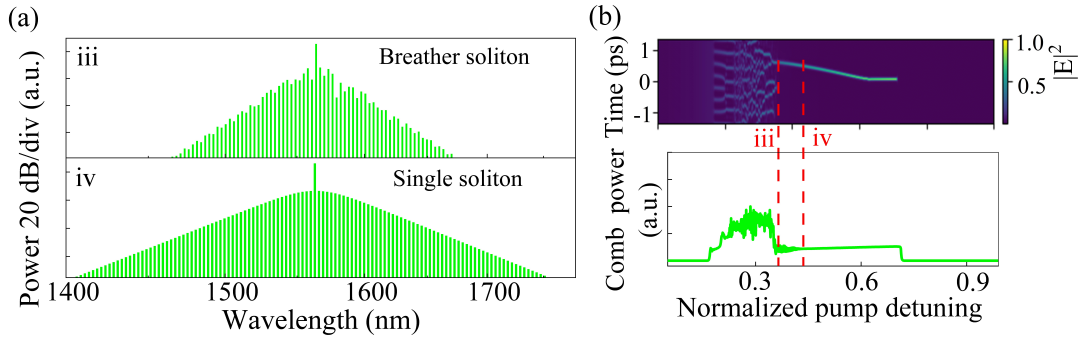


Figure 4.8: Simulation of the TE_{10} breather and single soliton microcombs using the LLE. (a) Simulated breather (upper panel) and single soliton (lower panel) microcomb with 490 mW pump power. (b) Intracavity field evolution map (top) and intracavity power evolution (bottom) by tuning from blue to red regions.

observe an obvious periodic oscillation in this region. Whereas, the red dashed line marked iv on a step-like region corresponds to a single soliton state. The obtained results in Fig. 4.8 agrees very well with the experimental results in Fig. 4.7(a).

4.4 Breather soliton crystals (BSCs)

Avoided mode crossing (AMX) is one of the common and crucial phenomena that occurs and is explored in microresonators. The microresonator cavities support multi-modes and therefore AMX is a ubiquitous process. AMX is the hybridization of two distinct polarization modes and crossings between the modes can happen [78]. The existence of AMX induces a change in the intracavity local dispersion. Hence, mode crossing can lead to generation of frequency comb in normal GVD [79]and phase matching to access dispersive wave (DW) [81]. Moreover, the AMX has been exploited to change and reorganize the $sech^2$ shape of the DKS in the cavity to equidistant temporal DKS pulses. This is achieved by the modulation of the continuous wave background as a result of mode crossing and interaction of co-propagating solitons ending up in self-organized DKSs [112]. These self-organized DKSs are characterized at the output of the MRR by discrete multi-FSR and enhanced comb lines. Such a novel state of the soliton microcomb is known as soliton crystals (SCs) [113][114]. The SCs are further explored and exhibit rich soliton dynamics based on the arrangement of the DKSs in the cavity [112][115][82]. Among these we will focus on the extraordinary breather perfect soliton crystals (BPSCs) in our AlN microresonator.

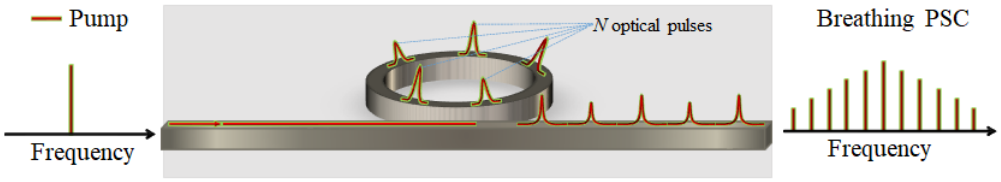


Figure 4.9: Schematic illustration of breathing perfect soliton crystals. N is the maximum number of equidistant optical pulses over the circumference of the cavity.

Firstly, we explain novel perfect soliton crystals (PSCs). The PSCs state is reached by the regularly spaced temporal soliton pulses in the cavity [95][82]. Unlike multi-solitons with stochastic distribution of soliton numbers [116], PSCs are not only evenly distributed but has enhanced comb lines on the output [117][118]. From the schematic diagram in Fig. 4.9, N is the maximum number of solitons in the cavity. Whereas at the output, enhanced comb lines are regularly spaced by N times the cavity FSR. The term breather is explained in section 4.1 for a single soliton. In the context of PSCs, breather corresponds to the temporal periodic oscillation of the cavity solitons. It is vital to mention that the regularity in the space is fixed and maintained despite the breathing state.

4.4.1 Experimental Observation of breather soliton crystals (BSCs)

To experimentally demonstrate the breather SCs we employed a 60-μm-radius AlN microresonator with the cross-section of 1.2×2.29 μm^2. The device used in this experiment has slightly different parameters of integrated bus waveguide compared to the one used in section 4.2. The bus waveguide coupling gap (G) is 0.5 μm and width (W) is 0.91 μm, respectively. Slight variation in the geometry can potentially re-engineer the resonance modes [78][87].The variation in integrated bus waveguide parameters has helped to achieve mode coupling in C-band. To characterize the device, a low power transmission spectrum (range, 1540 nm-1570 nm) is obtained as shown in Fig. 4.10(a). From the transmission spectrum, the device insertion loss is around 6.4 dB i.e., 3.2 dB per facet. Our device supports two modes (TE polarization in this case) which we attribute to narrow waveguide design. For ease of explanation, the modes are indicated with relative numbers (μ). Hence, the pump resonance used to excite the BPSCs is at μ=0 (∼1565.7 nm) and two close modes

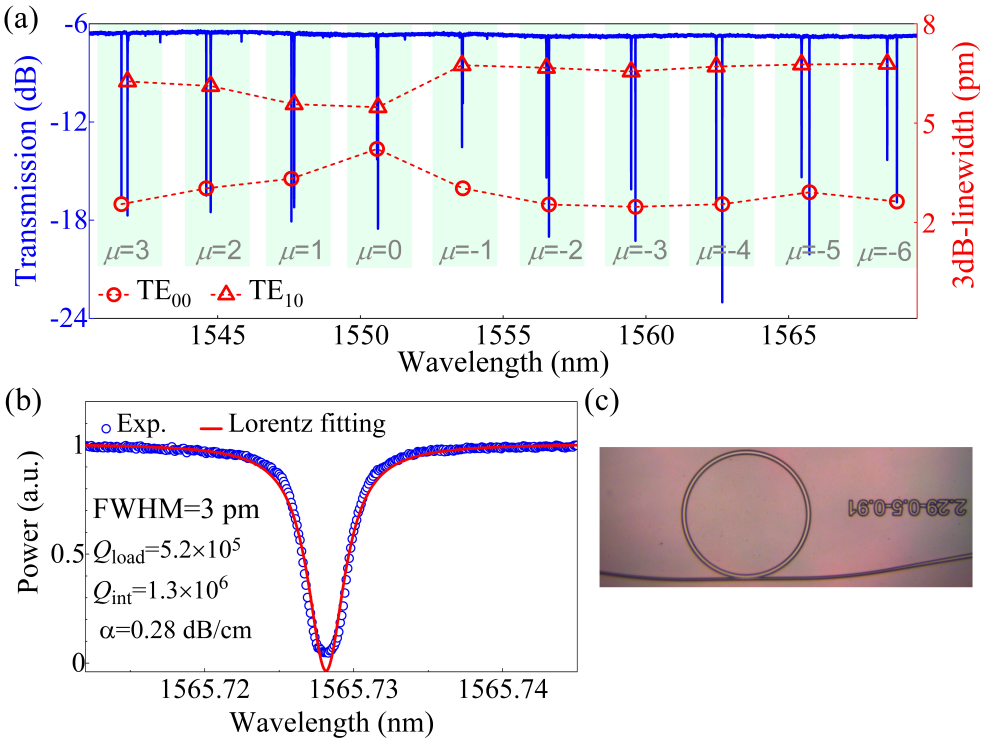


Figure 4.10: (a) Transmission spectrum of the TE polarization modes in the range from 1540 to 1570 nm under ∼40 μW power. The right side scale is 3-dB linewidth of the TE_{00} (marked with triangle symbol) and the TE_{10} (marked with circle symbols) polarization modes.(b) Pump resonance wavelength with Lorentzian fitting.(c) Microscopic image of the 60 μm-radius AlN device.

are at μ=5 (∼1550.7 nm). To pump the resonance mode at μ=0 at suitable pump power, it is crucial to characterize and extract the Q-factors. Figure 4.10(b) is the Lorentzian fitted TE_{00} pump resonance with extracted loaded Q_L and intrinsic Q_{int} quality factors of 5.2×10^5 and 1.3×10^6, respectively. We used the standard soliton generation experimental setup and technique to excite BPSCs. A relatively low pump power of 250 mW was used to pump the device and access the BPSCs. Exciting PSCs at relatively low power has been demonstrated in previous reported work [82][119][95]. Therefore, this piece of work can validate and add significance to demonstrate PSCs in various microresonator platforms. A resonance wavelength at ∼1565.7 nm is pumped with the laser sweep speed of 1nm/s. We obtained a triangle-shaped transmission with a distinct step feature and is shown in the inset of Fig. 4.11(a). The dashed lines (i)-(iii) correspond to the different forward red-detuned stop positions depending on laser wavelength [17]. The obtained combs states at various red-detuned stop positions include, (i) primary comb, (ii) MI comb (iii) disordered SC and (iv) 5-FSR BPSCs, respectively. The recorded comb spectra

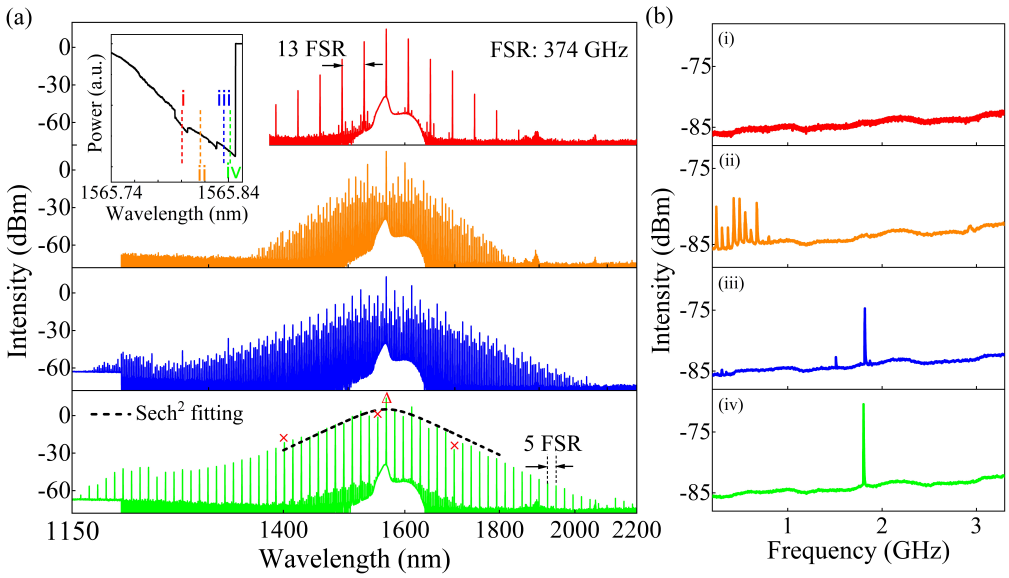


Figure 4.11: Experimental measurements of breathing perfect soliton crystals.(a) Optical spectra recorded at different red-detuned laser wavelength stop positions which is presented in the top inset of (a). 5-FSR soliton crystal (lower panel) is fitted with sech^2, where the pump and mode interaction points are marked with red triangle and cross symbols, respectively. (b) Corresponding RF noise spectra at detuning positions (i)-(iv).

at various stop position are plotted in Fig. 4.11(a). A multi-FSR (13×FSR) primary comb lines appear at the laser tuning position of ∼1565.80 nm. We observe the transition of primary comb to MI comb on red tuning the laser wavelength to a stop position at ∼1565.82 nm. The spectral range of the MI comb is from ∼1390 to ∼1800 nm. Whereas the transition of primary to MI comb is also verified from the recorded ESA RF noise spectra, shown in states (i) and (ii) of Fig. 4.11(b). Next, we move to the step-like region on the transmission. At the stop wavelength of 1565.83 nm we can access the disordered SC, which corresponds to the crystallization state between the breather DKS and PSC regimes. From Fig. 4.11(b) state (iii), the existence range of the disordered SC is between 1200 to ∼2000 nm with a DW wave at ∼1200 nm. There is a drastic reduction of RF noise level in the recorded spectrum, as shown in the state (iii) of Fig. 4.11(b). Finally, before the laser wavelength goes off-resonance, we carefully select the laser stop wavelength at the red-detuned position to access the PSCs. We term it the breather perfect soliton crystals (BPSCs) due to the presence of the narrow frequency tones at 1.53 GHz in the RF noise spectrum, in the state (iv) Fig. 4.11(b). From Fig. 4.11(a) state (iv), the output comb lines of soliton crystals are 5 FSRs apart and comparatively

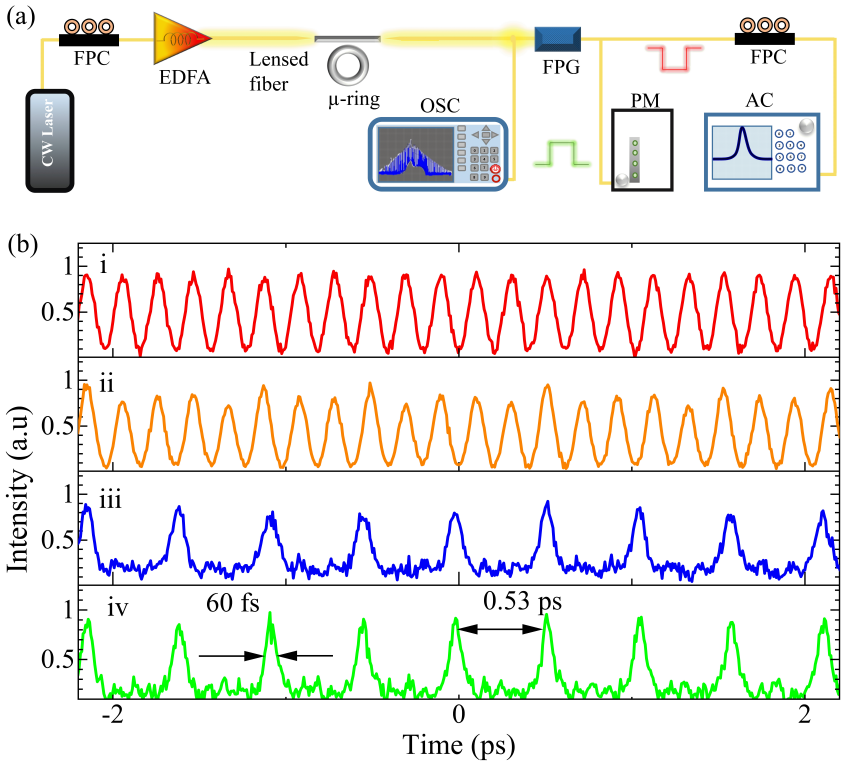


Figure 4.12: Pulse measurement.(a) Experimental setup used for pulse measurements using SHG-based autocorrelator (AC).(b) AC measurement results for the states (i)-(iv).

broader (range, ∼1150 nm to ∼2200 nm). Furthermore, to confirm the secant pulse shape the spectrum is fitted with a sech^2 fitting (shown with a black dashed line) with the 3-dB bandwidth of 8.5 THz.

To study the temporal waveform of microcomb at different states, we used an autocorrelator (AC-pulse width measurement range <10fs to 3.5ps) based on second harmonic generation (SHG) in our experimental setup (shown in Fig. 4.12(a)). The AC measurement helps us to measure the pulse width and repetition rate of the PSC in a coherent state. Figure 4.12(b) shows the temporal traces of microcomb states (i)-(iv). The sinusoidal AC traces correspond to primary and MI comb. The pulse period is 0.2 ps and is in good agreement with the measured spectrum of the multi-FSR primary comb (13×FSR). The AC traces in the states (iii) and (iv) correspond to the disordered SC and BPSCs. The pulse period in the state (iv) is recorded to be 0.53 ps and consistent with the measured BPSCs (5×FSR) spectrum. The 60-fs pulse width is measured by fitting the sech^2. It is comparatively narrower than the measured which we attribute to the low responsivity of our AC beyond 1600 nm.

4.5 Conclusion

We have studied for the first-time have studied and experimentally demonstrated novel breather solitons together with SRS in the AlN platform. The two adjacent modes at TE polarization, with TE_{00} as pump and TE_{10} as auxiliary modes, were used to excite breather solitons together with SRS at a slow tuning speed of 1nm/s. The existence of SRS together with breather solitons was also explored by pumping various TE resonance modes. Therefore, we can confirm the absence of nonlinear competition between the TE_{00} and TE_{10} modes. Further, we explored and studied fast laser tuning speeds significance at different detuning positions. This technique has potentially helped to overcome the SRS and eventually allows access to single solitons. We have demonstrated a near-octave spanning DKS are relatively high laser pump power (400 mW) and tuning speed (14 nm/s). Next, both in experiment and LLE-simulations we demonstrated breather and stable single solitons using the TE_{10} mode in another device with similar dimensions. This was possible with a suitable Q-factor and ER of the TE_{10} mode. Our study of a breather and finally single soliton in an AlN microresonator with various laser pump tuning speeds is a useful addition to soliton microcomb technology. The access of near-octave spanning makes it a promising candidate for future integrated self-referenced Kerr microcombs on an AlN chip [120]. Finally, we have also demonstrated an extraordinary near-octave spanning breather perfect soliton crystals in a third device. Compared to rich soliton dynamics, perfect soliton crystals have regularly space comb lines with enhanced power. We found a slight change in the device parameters can lead to mode-coupling. Based on our experimental results we attribute the generations of BPSCs to AMXs.

It is worth mentioning that the reported results of near-octave perfect soliton crystals in AlN microresonator are broader than the previously reported work. Further, well-designed micro-cavities have the potential to exploit octave-spanning PSCs on demand for potential microcomb applications.

Chapter 5

Dual-mode scheme single soliton generation and AMX-induced soliton crystals (SCs) in S_3N_4 microresonators

This chapter introduces a reliable design strategy of dual-modes in Si_3N_4 microring resonators (MRRs) using the finite element modeling (FEM) simulations, which enables deterministic access to an octave-spanning soliton. We also present the experimental observation of novel soliton crystals (SCs) with various soliton numbers (N) in Si_3N_4 and study their formation due to the existence of the avoided mode crossings (AMX).

5.1 Introduction

Over the past decade, silicon nitride (Si_3N_4) has emerged as one of the most promising potential platforms for photonics integration. A significant amount of effort and continuous research work by scientists have made this platform mature and paved its way from basic research to various applications, as presented in Fig. 5.1 [15][67][121][122][123][124][125]. One of the prominent advantages of the Si_3N_4 platform is its compatibility with the standard complementary metal-oxide semiconductor (CMOS) manufacturing processes [89][126]. This makes the fabrication and integration feasible at an industrial level which is cost-effective for ultimately building photonic integrated circuits (PICs) as required for many applications [127][128]. Second, the optical characteristics of Si_3N_4 material make it an attractive platform,

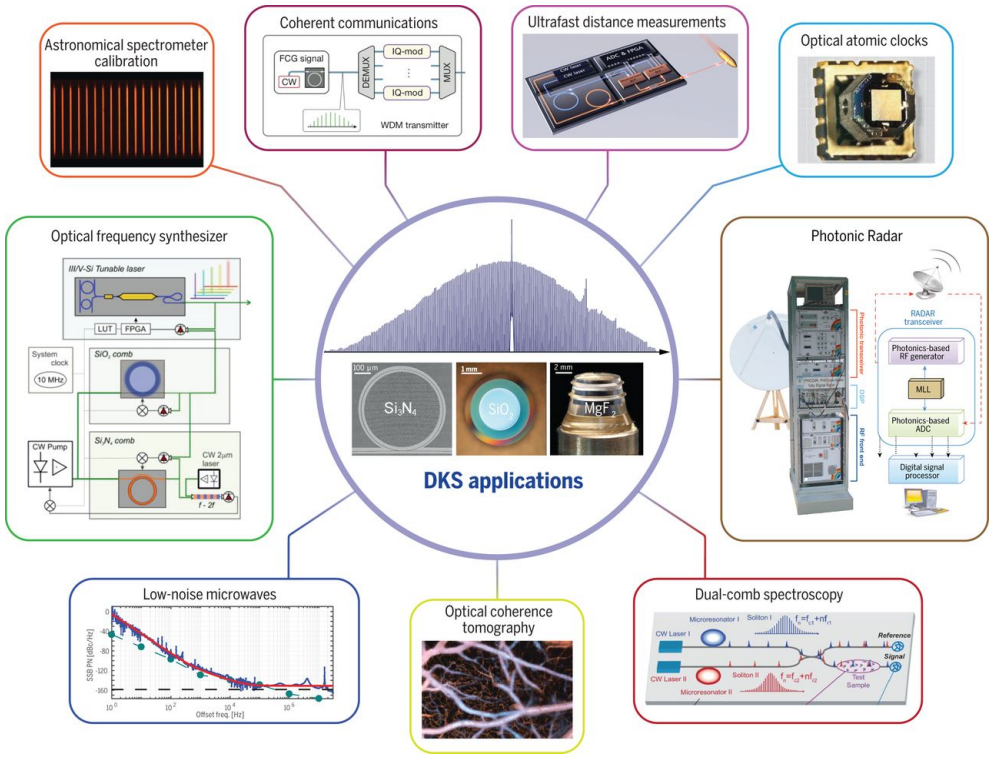


Figure 5.1: Scheme presenting the single soliton microcombs applications [53].

it has a wide transparency window ranging from the visible to mid-infrared (mid-IR) i.e., 2.5-8 μm. A large band-gap of 5eV minimizes two-photon absorption (TPA) close to zero in the given Si_3N_4 transparency window. The TPA is a phenomenon where two-photon absorption leads electrons to excite to a higher state and de-excite with an energy less than the two absorbed photons and causing a significant power loss to the propagating optical wave. It has a refractive index of 2 at 1.55 μm of wavelength and a moderate non-linear coefficient of $\sim 2.4\times10^{-19}$ m^2W^{-1} [129]. The fabrication of Si_3N_4 microcavities embedded in SiO_2 (n $\sim$1.45) can achieve high light confinement due to the index contrast and ultra-high quality (Q) factors [130]. Hence, the negligible TPA, wide transparency window, high confinement and low loss enable efficient nonlinear processes in Si_3N_4 microcavities. The novel properties and performance of the on-chip Si_3N_4 microresonator, makes it ideal choice for the applications such as communication [67][131][132], spectroscopy [73][133], frequency synthesizer [15], LiDAR [50][69][121], astronomical spectrometer calibration [125] and optical clock [134] [14][66].

5.2 Design of dual-mode microresonators and characterization

The microresonator-based soliton microcombs of bandwidth of at least an octave are vital and a prerequisite for many practical applications. Careful dispersion engineered design and a well-controlled fabrication process have enabled the achievement of broadband soliton microcombs. In recent years, researchers have demonstrated an octave-span soliton microcombs in number of microresonator platforms, including Si_3N_4 [15][20][22][56][135][136], AlN [27][28] and LN [137]. One of the key challenges in reaching the soliton state is the cavity thermo-optic induced instability. The high pump power and forward tuning of the laser wavelength result in the cavity heating due to the intracavity heat absorption [17]. Hence, the cavity enters thermal instability at the red-detuned pump region and accessing the stable single soliton can be challenging. It is crucial to overcome this challenge for on-chip integration and a range of promising applications. Therefore, over the past few years, several experimental schemes have been introduced for deterministic access to soliton microcombs. These universal schemes, which apply in all material platforms, include fast laser frequency scan [17][28], power kicking [16], cavity thermal tuning [73], dual-pump and –several resonance schemes [75][76] and dual-pump with single resonance [138]. These methods significantly increase the routes to access the soliton state in the various platforms. Despite all these advances in the experimental schemes, key challenges here are system complexity, cost, and a reliable route to deterministically access the single soliton. For miniaturization and integration of the microresonator in the photonic integrated circuits it is crucial to overcome these challenges [139]. Therefore, deterministic access to an octave span DKS generation at a low cost and low system complexity is essential in practical applications. Here, we introduce straightforward and deterministic access to an octave span DKS using a dual-mode pump scheme. The dual-mode pump scheme, also denoted by 1P2R (see detailed explanation in sec 3.1), utilizes a single pump to two adjacent resonances with the same polarization. The idea of the 1P2R strategy was presented by our group to deterministically access an octave span DKS [27]. We demonstrated an octave and near octave spanning DKSs using 1P2R scheme in the AlN microresonators and

the results are presented in chapters 3 and 4, respectively. We note one previous work of the single DKS demonstration using a dual-mode scheme but with mixed polarization [20][140]. In contrast to our scheme of the same polarization, the dual mode mixed polarization can be rather difficult to operate and requires careful polarization adjustments.

In this work, we present a reliable strategy of modeling and designing of microcavities to achieve the desired adjacent modes for broadband single DKS stabilization. Having observed the dual mode scheme in AlN, we need to establish the design rules for this scheme and the well-developed Si_3N_4 platform offered the best possibility of realizing its development. High-Q Si_3N_4 MRRs were fabricated by the foundry Ligentec (Switzerland) from designs created in our group [37]. The cross-section schematic diagram of Si_3N_4 microcavity waveguide is shown in Fig. 5.2(a). The 0.8 μm thick Si_3N_4 MRRs having a fixed radius of 23.3 μm is buried in the SiO_2 with the top cladding layer of 1.7 μm. We expect these MRRs to have an FSR of about 1THz at 1550 nm. Figure 5.2(b) shows the microscopic images of 23.3-μm-radius Si_3N_4 MRRs integrated with the bus waveguides. The fixed radius cross-section design with varying ring widths (RWs) of the microresonator was carried out by the finite element modeling (FEM) simulations using a COMSOL multiphysics software [51]. Figure 5.2(c) shows the simulated transverse electric (TE) resonance wavelengths in the range from 1540 nm to 1580 nm. An obvious red shift of the modes is observed with the increase of the RWs. For further analysis of the modes shifting, we calculated the slope dλ/dW for TE_{00} and TE_{10} modes to be 0.012 and 0.0094, respectively. We attribute the large slope value of the TE_{10} to the mode field distribution and effective refractive index. Moreover, by calculating the mode separations ($\Delta\lambda$=λ_{10}-λ_{00}), we find that a 1nm RW change will bring a $\sim$0.08 nm variation in the mode separation. By changing the RW by 100 nm, we can estimate the $\Delta\lambda$ variation to be $\sim$8 nm i.e., almost on cavity free spectral range (FSR). Hence, at the RW of 1.68 μm (Fig. 5.1 (c)), the two TE_{00} and TE_{10} modes exist in proximity to one another at a wavelength of 1563 nm, with the angular mode numbers (m) of 165 and 152, respectively. The mode separation ($\Delta\lambda$) between the two adjacent modes is 0.09 nm with the TE_{10} at the red end. With the 100 nm RW change i.e., 1.78 μm, the two close modes appear at the wavelength of $\sim$1572 nm. The separation

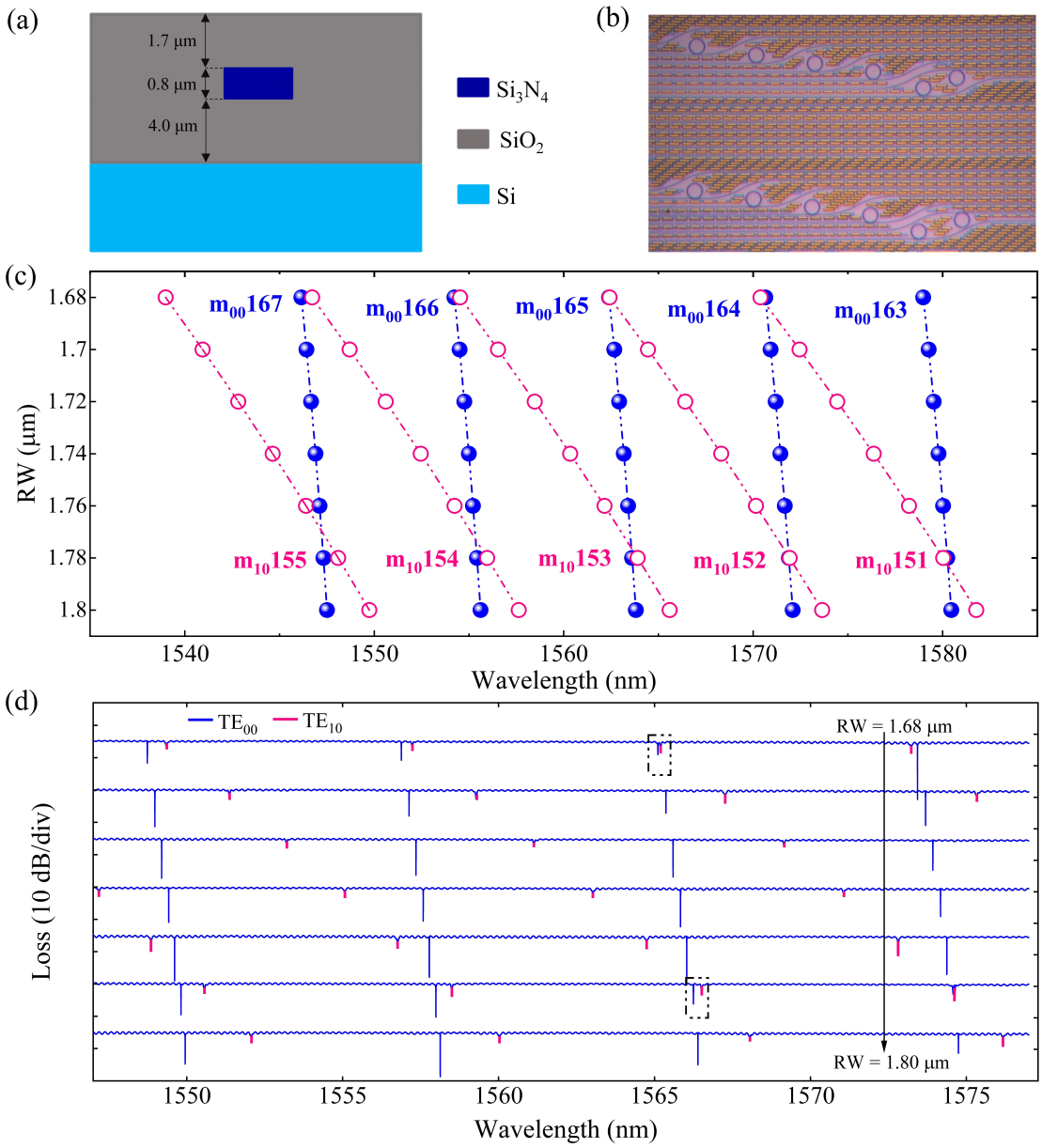


Figure 5.2: (a) Schematic of 2D cross-section parameters of the Si_3N_4 microresonator. (b) Microscopic image of the fabricated 23-μm-radius MRRS with integrated bus waveguides. (c) Simulated TE polarization resonant wavelengths for Si_3N_4 MRRs with a fixed radius of 23-μm , waveguide thickness of 0.80 μm and various RWs of 1.68-1.8 μm with the step of 20 nm. (d) Measured TE polarization transmission spectra of the 23-μm-radius MRRs with the diverse RWs (range of 1.68:0.02:1.80 μm). The target dual-modes with pump on the blue side are denoted by the dashed rectangular boxes.

between the adjacent modes in this case is 0.12 nm.

The typical TE polarization transmission traces of the fabricated 23.3 μm-radius Si_3N_4 microresonators with the varying RWs from 1.68 to 1.80 μm are shown in Fig. 5.2(d). The integrated bus waveguides width and coupling gap is 600 nm and 650

nm, respectively. The transmission traces for both the TE_{00} and TE_{10} (pink-colored) polarization modes, in the wavelength range of 1547nm to 1577 nm, redshift at the almost same rate as in the simulation. The measured FSRs for TE_{00} and TE_{10} modes are ∼1012 and ∼979 GHz, respectively. The target dual-modes in the RW of 1.68 μm are marked with the rectangular dashed line. The center wavelength of the two adjacent modes is 1565.15 nm and the separation between the two modes is 0.08 nm (∼10.5 GHz). Whereas at the RW of 1.78 μm, the dual-modes appear at ∼1566 nm with the relatively large modes separation of ∼0.26 nm. Compared to the simulation the slight shift in the positions of the two adjacent modes is attributed to variations in the fabrication. Our experimental results are still consistent with the FEM simulations and the rigorous modeling paves the way to dual-mode microresonators in various other platforms.

The broadband microcombs generation is potentially achieved by microresonator dispersion and dispersive wave (DW) engineering. For an efficient FWM an anomalous and near-zero positive integrated dispersion (D_{int}) is vital. Whereas, to extend the comb bandwidth the DW is crucial i.e., the position where positive D_{int} switches from positive to negative [16]. Moreover, the position of the DW can be tailored by careful variation of dimensions of the target waveguide cross-section [56][141]. Figure 5.3(a) shows the calculated D_{int} curves of TE_{00} mode family of our above-proposed model of MRRs with a fixed radius of 23.3 μm and various RWs (1.68-1.80 μm). All the MRRs, in the frequency range of 130 THz to 320 THz, can achieve dual-DWs. At the high-frequency end, there is an obvious decreasing trend in the position of the DWs (range, 311 THz to 254 THz) with the increase of the RWs. The second-order dispersion parameter ($D_2/2\pi$) estimated from FEM simulation are 37.2 and 19 MHz for the RWs of 1.68 μm and 1.78 μm, respectively. Next, we measure the optical spectra of the modulation instability (MI) combs in the fabricated MRRs, shown in Fig. 5.3(b). Due to the existence of the dual-DWs, all the MRRs can exceed more than an octave span with an on-chip power of 400 mW. In the optical spectra, the enhanced or reduced comb line intensities (denoted by the dashed lines) are caused by the mode interactions [78]. Based on the simulation results the wider RW has lower second-order dispersion. Hence the MI comb spectra have a flatter envelope and stronger comb lines at the DWs. The experimental results

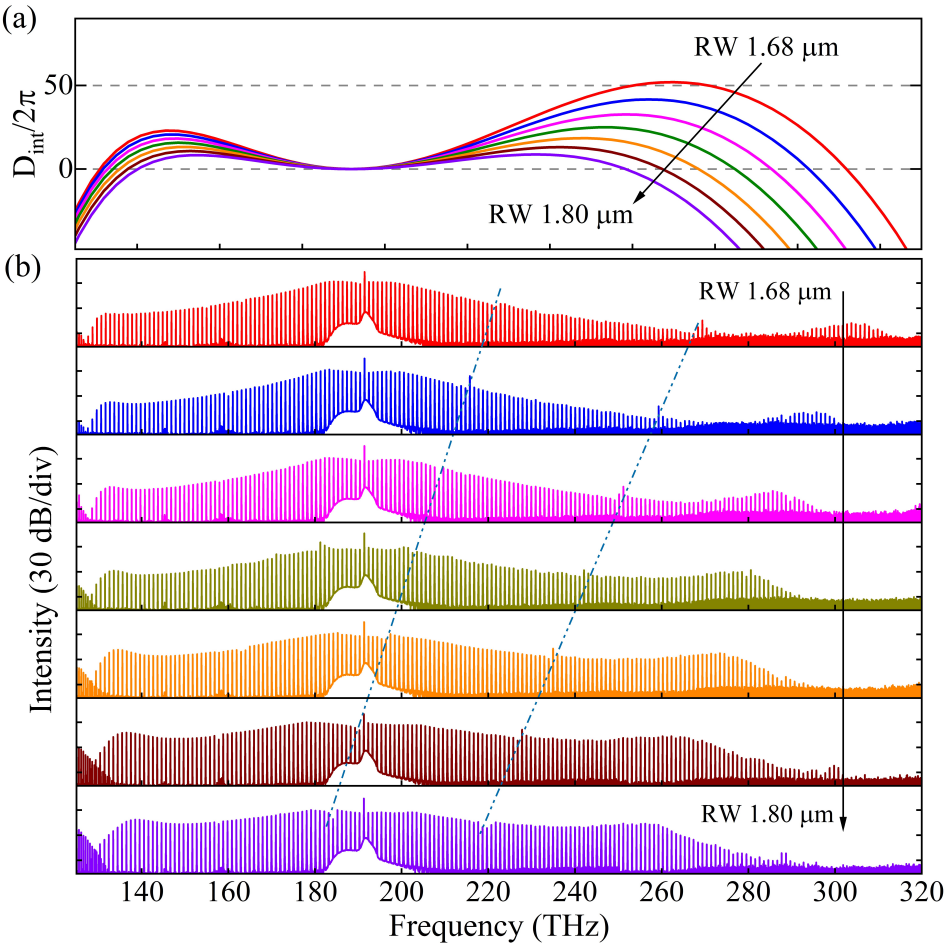


Figure 5.3: (a) Calculated integrated dispersion via FEM-based simulations of the 23-μm Si_3N_4 MRRs with various RWs. (b) Measured optical spectra of the designed MRRs. The dashed lines indicated the mode interaction positions. Variations in the comb spectra are clear from the different RWs.

are quite consistent with the simulated dual-DWs trend, suggesting that rigorous modeling and simulations can be used as universal tools for broadband microcomb generations.

5.3 Generation of an octave-spanning DKS via dual-modes scheme

For the generation of an octave-span soliton we employed the microresonator with the RW of 1.68 μm. The target dual-modes near 1565 nm, zoomed-in image shown in Fig. 5.4(a), are used for the stabilization of the single soliton and the dual-mode scheme is detailed in chapter 3. The separation between the two modes is ~84 pm and the extracted Q-factors for the TE_{00} and TE_{10} modes are 1.1×10^6 and

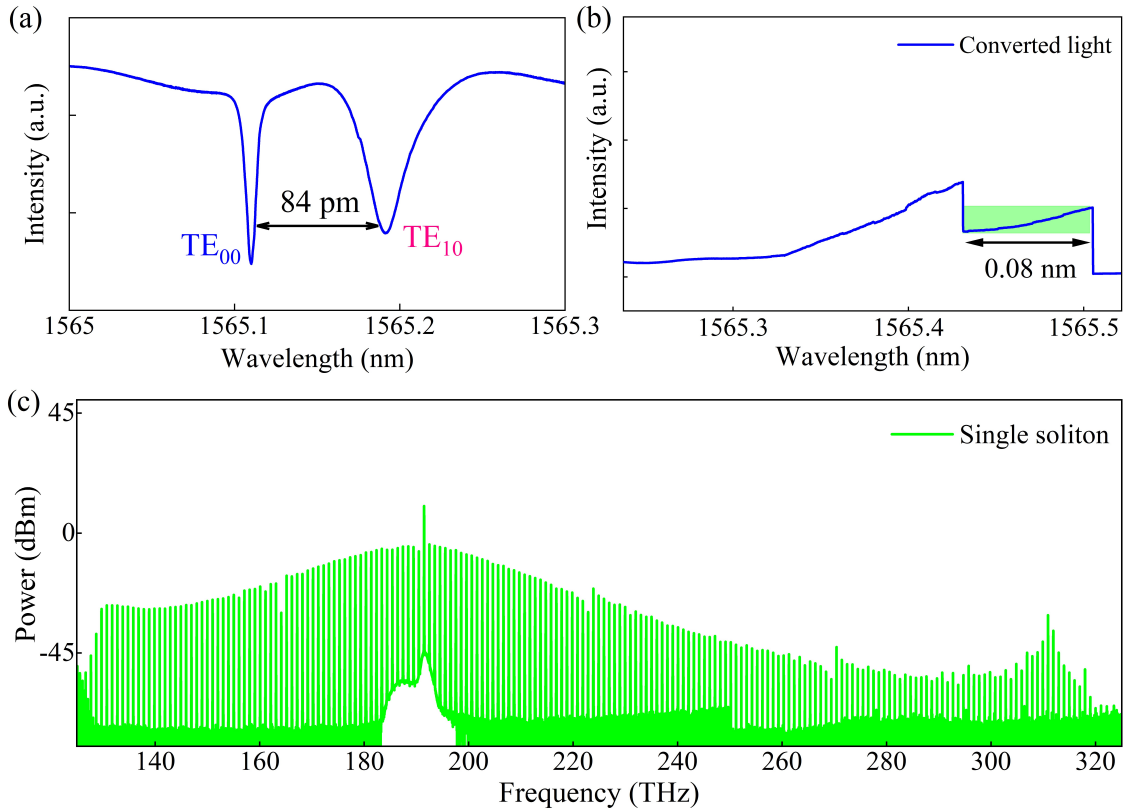


Figure 5.4: (a) Zoomed-in image of the two close modes. (b) Converted light (difference between the pump and all transmission) trace at a pump power of 150 mW. The soliton step, also termed SER, is marked with a green rectangle. (c) Measured optical spectrum of the single soliton.

4.2×10^5, respectively. We use an on-chip power of 150 mW and record the converted light trace i.e., a difference of all- and pump-transmission (measurement details in section 3.5), as shown in Fig. 5.4(b). Using a relatively slow tuning speed of 1 nm/s, a typical 0.08 nm wide single soliton step is observed. To access the single soliton, we sweep the laser wavelength using the forward tuning technique i.e., from blue to red detuned region. Stopping the laser wavelength on any position on the step-like region we can deterministically access the single DKS and recorded optical spectrum as shown in Fig. 5.4(c). The soliton spectrum can exist for approximately an hour and is impressively 1.5-octaves span wide, it ranges from 125 to 322 THz with the dual-DWs at 132 and 311 THz. The position of the dual-DWs coincides very well with the simulated integrated dispersion [141].

5.4 Generation of soliton crystals (SCs)

In multi-mode microresonators, the interaction of the modes from the same or different polarization modes is inevitable and the phenomenon gives rise to what is known as avoided mode crossings (AMXs) [78][87][142]. Achieving the mode coupling has always been a challenge and is generally non-controllable due to variations that can occur in the fabrication process. Our proposed rigorous design, simulations (details in section 5.2) and high-yield fabrication results are universal (they can be applied to Si_3N_4 and other platforms) which pave the way to achieve the desired mode couplings irrespective of which platform is utilized. Several studies have revealed the significance of the AMXs as it leads to the variation of the microresonators local dispersion and the modulation in the CW intracavity background. Therefore, the AMXs-induced intracavity modulation leads to the perturbation of the single DKS spectrum to evenly distributed DKS pulses [82][112][143][144]. These evenly distributed DKS pulses give rise to a novel soliton state known as soliton crystals (SCs) [82]. The irregularities in the evenly distributed DKS pulses can occur due to the missing or shifted soliton pulse/s and is termed as defects [82]. The novel SCs has attracted significant interest among scientists due to their extraordinary characteristics such as, (i) The SCs are free from defects and each pulse exhibits identical characteristics as a single soliton. (ii) The SCs pulses are evenly distributed over the circumference of the micro-ring and separated by the integer number of free-spectral-range (N×FSR) and achieve N^2 energy enhancement in the distributed pulses in contrast to single soliton. (iii) The conversion efficiency (CE) is strikingly enhanced which is crucial for many microcomb applications.

We experimentally demonstrate the deterministic generation of the octave-spanning SCs by exploiting the AMXs in our Si_3N_4 microresonators platform. An anomalous dispersion engineered Si_3N_4 microresonator device (D1) with a fixed radius of 23.3 μm and a cross-section of 0.8×1.7 μm^2 (Height × Width) was employed. We observed a variety of SCs with the various fixed comb line spacings associated with the mode interaction position. A typical transmission trace (full CW laser range, 1480-1640 nm) of the TE polarization mode of the D1 is shown in Fig. 5.5. From the transmission trace, we can easily identify that the D1 can support both the

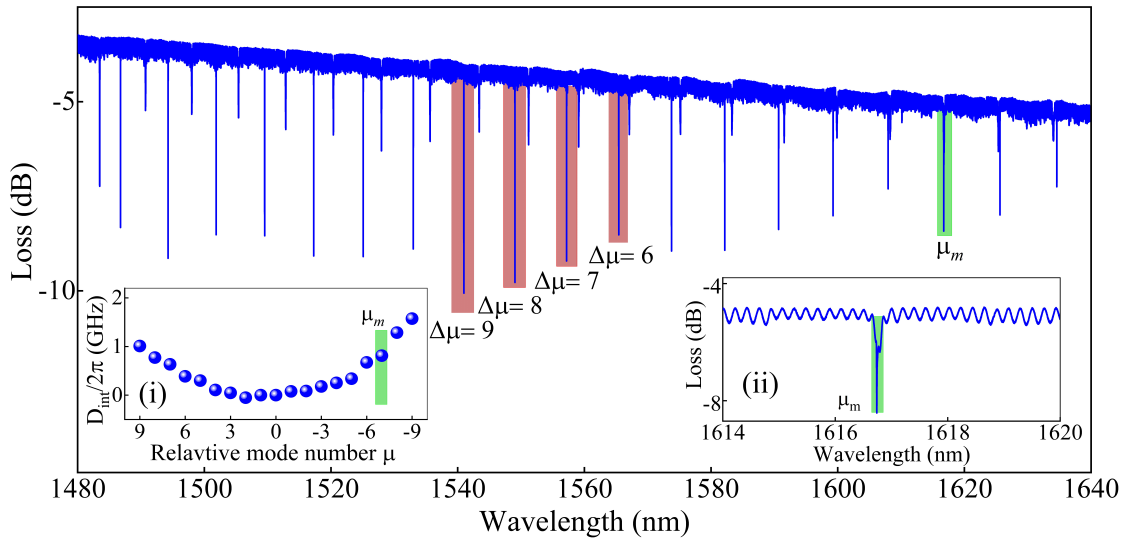


Figure 5.5: Measured transmission spectrum at TE polarization mode for the device D1 at the laser wavelength range between 1480 nm to 1640 nm. The longitudinal pumped modes (marked with red rectangles) to obtain the various SCs are denoted by the relative mode numbers (μ_p) far from the mode crossing position (marked with green rectangle and denoted by the relative mode number (μ_m). Inset (i) is the calculated integrated dispersion for the TE_{00} mode as a function of relative mode numbers μ where μ_p=0 is at around 1557 nm. Inset (ii) is the zoomed-in image of the mode interaction near 1615 nm.

TE fundamental and higher order modes. We denote the modes with relative mode numbers (μ). The mode interaction position is denoted by μ_m=-7 and marked with green rectangles. The red-circled marked modes are the pump modes to access the SCs. The inset (left) of Fig. 5.5 shows the calculated integrated dispersion of the measured fundamental TE modes. The dispersion profile shows it has anomalous dispersion with the $D_2/2\pi$=32 MHz. The marked region (green rectangle) on the dispersion curve shows the mode interaction position.

In order to study the SCs evolution, we select the mode at $\Delta\mu$ =6 (near 1566 nm) which can match our FBG bandwidth range. Figure 5.6(a) shows the recorded comb power trace i.e., filtering the pump and with launching an on chip-power of 255 mW in D1 and at a relatively slow speed of 1 nm/s. An obvious SC existence step (green rectangle marked) can be observed on the comb power trace with a range of 0.04 nm (∼5GHz). Whereas the recorded optical spectra plotted in Fig. 5.6(b) corresponds to the (i) primary comb, (ii) MI comb, and (iii) SC with the line spacing of N=6 FSRs apart obtained at the stop wavelengths of 1565.90, 1566.10, and 1566.22 nm, respectively. To verify different comb states, the RF intensity noise spectra were

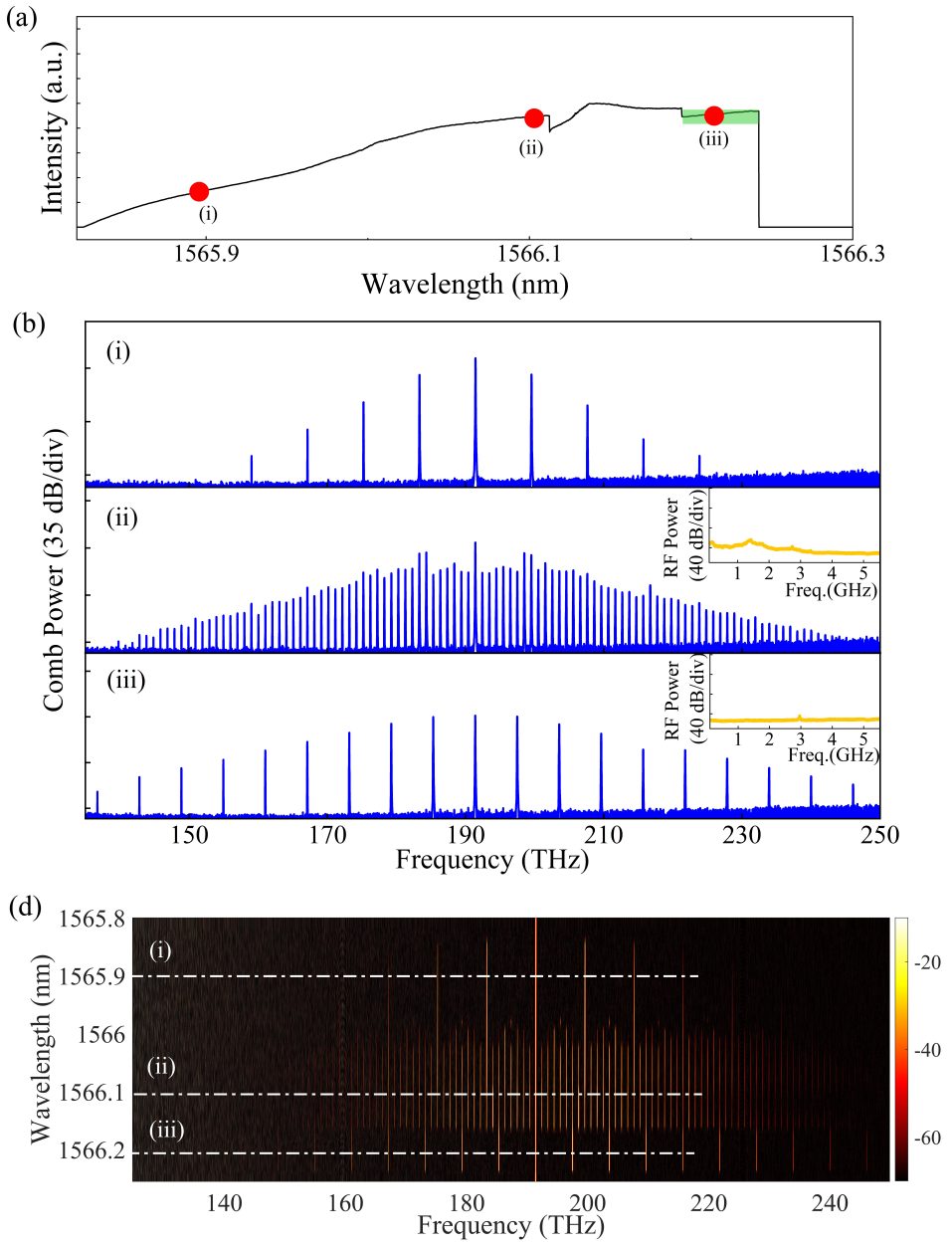


Figure 5.6: Experimental results of N=6 SCs in device D1. (a) Measured comb power at on-chip power of 255 mW. The SCs access region of 0.04 nm i.e, $\sim$ 5 GHz, is marked with a green rectangle. The red circular dots denotes the wavelength stop position to access the three comb states i.e., Primary, MI and SCs microcombs. (c) Measured optical spectra (i) Primary comb (ii) MI comb and (iii) SCs. Insets in states (ii)-(iii) of Fig. 5.6(c) are the corresponding RF spectra. (d) SCs evolution map and different comb states are marked with white dashed lines (i) Primary comb (ii) MI comb and (iii) SCs with N=6.

also recorded for the states (ii) and (iii), as shown in the insets of Fig. 5.6(b). A drastic reduction in the noise level is observed during the transition of the comb

from the states (ii) to the desired state (iii) i.e., SCs regime.

Furthermore, to study the SCs existence step we plot the evolution map. The evolution map is obtained by sweeping the laser wavelength to different stop wavelengths and recording the optical spectrum at a step of 15 pm, respectively. We select the mode at $\Delta\mu$ =6 (near 1566 nm) which can match our FBG bandwidth range. The evolution map of the SCs obtained by sweeping the laser to various red detuned stop positions on the comb power transmission trace is shown in Fig. 5.6(c). The three marked regions with white dashed lines on the map corresponds to the (i)-(iii) states of SCs spectral evolution.

Tunable octave-spanning SCs generation

The novel and versatile octave-spanning SCs with various soliton numbers N were deterministically generated in our device (D1). To experimentally access the SCs, we use the forward tuning technique [17] and a relatively low pump power [82][143] which is crucial (see details in sec. 3.3 and 4.4.1). From Fig. 5.5, we observe an obvious AMX is at a relative mode number μ_m=-7 and select the pump modes far (N×FSR) from this AMX position to achieve various SCs. We inject an on-chip power of 255 mW and pump the wavelengths at ∼1541 nm (μ_p=2), ∼1549nm (μ_p=1), ∼1557 nm (μ_p=0) and ∼1566 nm (μ_p=-1) to obtain the SCs (range, 1200-2400 nm) with N=7,8,7,6, respectively and depicted in Fig. 5.7(a). For the pump modes μ_p=1,0,-1 the obtained N=8,7,6 SCs where N=$\Delta\mu$=μ_p-μ_m i.e., at the difference of one N×FSR. Whereas, for the achieved N=7 SCs at the μ_p=2 we assume a potential AMX at the lower wavelength i.e., an integral multiple of N×FSR [140]. All the realized SCs were deterministic and stable as a high resolution of 0.05 nm was used to record the optical spectra. To monitor the temporal waveforms auto-correlator (AC) measurements were performed. The AC pulse traces for N=7,8,7,6 SCs are shown in Fig. 5.7(b). We measure the pulse periods (inversely proportional to f_{rep}) of 0.14, 0.125, 0.14 and 0.17 ps for the N=7,8,7,6 SCs, respectively.

Similarly, we realized SCs with various comb line spacings in another device denoted as D2. The design and dimension parameters are similar to our D1 but with a relatively large bus waveguide coupling gap (G=0.7 μm). Figure 5.8(a) shows the typical transmission trace of the TE polarization mode for device D2. The mode coupling

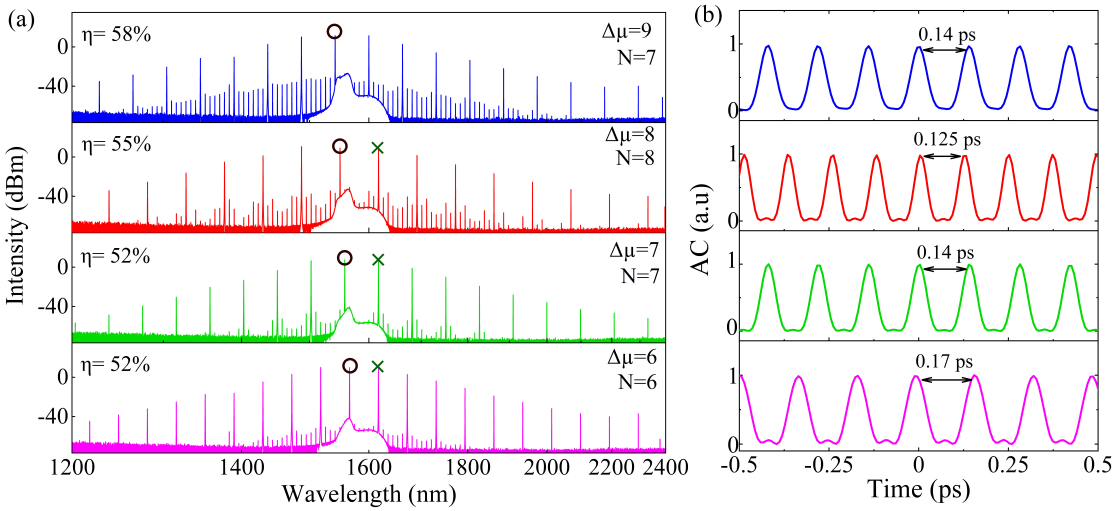


Figure 5.7: (a) Optical spectra of different octave-spanning SCs obtained in D1 at the relative pump modes μ_p= 2,1,0,-1 and the mode interaction at μ_m=-7. The symbols circle and cross denote the pump and mode interaction, respectively. (b) Measured auto-correlation traces of the obtained different SCs.

of TE_{00} and TE_{10} is observed at μ_m=-7 and indicated with the green rectangles. The pump modes are at μ_p=0,-2,-3 and indicated with red rectangles. Figure 5.8(b) shows the achieved various SCs with the particular pump mode. When the pump wavelength is ∼1548 nm (μ_p=0) we obtained N=4 SCs at a relatively low on-chip power of 175 mW. The N=4 SCs at μ_p=0 is at a difference of integer number multiple of N×FSR and due to the possible AMX at lower wavelength. Similarly, at an on-chip power of 275 mW we select the pump wavelengths of ∼1565 (μ_p=-2) and 1573 nm (μ_p=-3) to achieve N=6,5 SCs which are at the difference of one N×FSR. The temporal waveforms of N=4,5,6 SCs are measured with the AC and plotted in Fig. 5.8(c). From the AC measurements we can calculate the pulse periods of 0.25, 0.17 and 0.2 ps for the N=4,6,5 SCs. Next, the obtained SCs in the devices D1 and D2 at the various pump modes (μ_p) are summarized in table I.

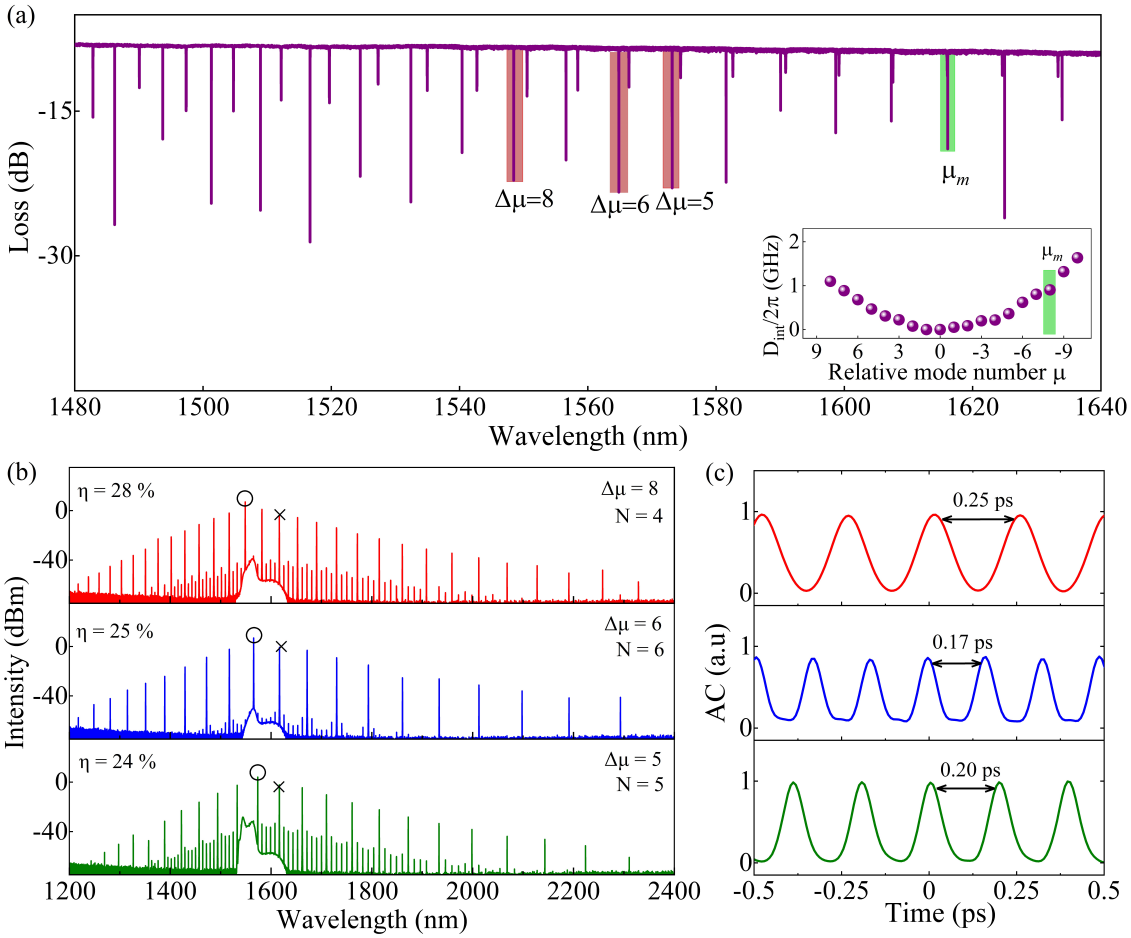


Figure 5.8: (a) Measured transmission spectrum of D2 at the TE polarization mode in the laser wavelength range 1480-1640 nm. The pump modes are marked with red rectangles far from the mode interaction position (marked with a green rectangle). Inset is the calculated integrated dispersion for the TE_{00} mode as a function of relative mode numbers μ at the around μ_p=0, i.e., 1548 nm. (b) Optical spectra of different SCs in device D2. The symbols circle and cross denote the pump and mode interaction, respectively. (c) Measured corresponding AC traces.

Device D1		N	7	8	7	6
R (μm)	23.30	Wavelength (nm)	∼1541	∼1549	∼1557	∼1566
W (μm)	1.70	μ_p	2	1	0	-1
G (μm)	0.55	μ_m	...	-7	-7	-7
Device D2		N	4	...	6	5
R (μm)	23.30	Wavelength (nm)	∼1548	...	∼1565	∼1573
W (μm)	1.7	μ_p	0	...	-2	-3
G (μm)	0.70	μ_m	...	...	-8	-8

Table 5.1: Summary of the dimensions of the employed devices D1 and D2. Obtained diverse SCs with N soliton number, pump wavelengths at the relative mode numbers and the mode interaction positions.

Conversion efficiency of soliton crystals (SCs)

We also investigate the conversion efficiency (CE) of the obtained various SCs. The CE is the ratio between the input pump power to the power converted into the comb lines at the output without the pump i.e., $P_{pump}/P_{comblines}$ (see microresonator energy flow details in section 3.5) [145]. The higher CE is critical and a key requirement in the miniaturization and on-chip integration of microcombs [146][147][148][149]. In recent years immense efforts have been made on the microcavities design and pumping schemes to improve the overall performance [145][150][151]. Here, we report the CEs of the measured various SCs with above ∼50% performance in one of the devices. In the device (D1), the CEs for the N=7,8 SCs at μ_p=2,1 are 58% and 55% at an error of 4%. Whereas for the N=7,6 SCs at μ_p=0,-1 the CEs are calculated to be 52% and 52%. Furthermore, in the device (D2) the obtained overall CEs of the N=4,6,5 SCs at the μ_p=0,-2,-3 are 28%, 25% and 24% with an error of 3%, respectively. It is important to note that the comparatively low performance of the D2 resonator can be possibly attributed to the relatively large waveguide coupling gap and poor performance of the external coupling power. The achieved broad SCs in this work are in the range of an octave-span and with the performance of above 50% in CE makes it a potential candidate for diverse industrial and commercial applications.

5.5 Conclusion

In conclusion, we have carried out detailed simulation work on the design and modeling of the Si_3N_4 microresonator waveguides to realize dual-modes reliably. Next, using the dual-mode strategy (termed 1P2R) we have deterministically demonstrated an octave-span soliton in Si_3N_4 MRRs. We believe the systematic design and high-yield fabrication, i.e., the performances of the fabricated devices match very well the desired design, is a universal strategy for the realization of dual-modes and broadband DKSs. The octave-span DKS generation with the 1P2R scheme is potentially significant and cost-effective for the on-chip integration of soliton microcombs [152]. Furthermore, we observed AMXs due to the rigorously designed microcavities. We demonstrated the AMX-induced octave-spanning of various SCs deterministically

and our devices enable on-demand generation of SCs. Finally, we also tested the performance of the devices by measuring the CEs. The performance of the D1 is impressive with the CEs above 50%.

The overall results of simulations and design match very well with the fabrication and pave a path to future reliable design in various platforms. The study significantly contributes to the rich dynamics of soliton microcombs and specifically to AMX-induced SCs. Furthermore, the findings related to broad versatile SCs are vital for applications such as data communication [67][153] and self-referencing [28].

Chapter 6

Conclusion and Future work

In conclusion, this thesis investigates the study of soliton microcomb generation in aluminum nitride (AlN) and silicon nitride (Si_3N_4) microresonators. Chapter 1 provides the fundamental theory of microresonators including the response of transmission and power enhancement factors as well as the quality factors at different coupling conditions. Anomalous dispersion is a crucial condition for efficient and broadband microcombs generation. Both the material and device geometry contribute to the total dispersion whereas, particularly the microresonator dimension can significantly help to tailor the dispersion profile for broadband comb formation. Therefore, chapter 2 explains the dispersion engineering in the AlN microcavities study via a numerical model developed in COMSOL. The optimization of various parameters, such as ring width, height and radius, to achieve a near-zero anomalous dispersion is studied as well. The materials presented in both chapters contributes to understanding the fundamentals and potential future design schemes with desired dispersion profiles and coupling conditions that are vital for microcomb generation. Chapter 3 demonstrates the experimental observation of an octave-spanning (range, 1100-2300 nm) soliton microcomb in an AlN microresonator (repetition rate, 374 GHz), using a rather simple and straightforward dual-mode (same polarization) scheme, proposed for the first time by our group. To date, many experimental techniques have been developed by researchers to overcome the thermal instability that accompanies soliton formation. Schemes to improve the soliton state stability in microresonators include dual-pumping, rapid-laser frequency scanning, thermal tuning using micro-heater, and dual-pump mixed polarization. The drawbacks of

these techniques are the requirement of additional opto-electronic equipment, such as an extra laser, amplifier, RF-sources, and complex polarization control. Whereas, the dual-modes we study are two close transverse modes belonging to the same polarization which approach each other (within several GHz) at the pump wavelength region. Our dual-mode method enables the accessing of the soliton state with slow pump sweeping (or even manually change), which paves the way to simplify the generation of soliton microcomb sources without additional equipment or complicated control. Moreover, we also studied the soliton behavior and mode interactions with the addition of an external temperature controller (TEC). Interestingly, we can increase the soliton existence range (SER), the region where stable soliton microcomb is accessed deterministically, from 10 GHz to 16 GHz. The achieved prominent octave-spanning solitons with wide SER are crucial for monolithic integration and microcomb applications. Above room temperature, two-soliton states were also observed in the same device.

In chapter 4, using other dual-mode AlN devices with the same dimension as the previous one, we also explore breather solitons and soliton crystals induced via mode interaction. In the first set of breather results, we explored the laser pump power and scan speed to overcome the breather state and access the stable single soliton. However, at the pump power of 400 mW and a scan speed of 14 nm/s, we can successfully achieve a 4/5 octave-span of microcomb with potential application for the self-referenced 2f−3f scheme with Kerr microcombs [120]. Next, a near octave-spanning (range, 1150-2200 nm) soliton crystals (SCs) (line spacing of N×FSR) were demonstrated in carefully designed AlN devices. The realization of SCs in AlN devices is a significant addition to understanding the soliton behavior. Further design research will help realize tunable SCs in the same device and explore the microcavities with various free spectral ranges (FSRs).

The stable octave-spanning soliton microcombs generation across various materials will confirm the reliability, robustness, and universe of the dual-mode scheme for soliton generation and stabilization. Lastly, in chapter 5, we successfully presented a rigorous design strategy using Si_3N_4 platforms to realize the dual-mode resonators and demonstrate the deterministic generation of an octave-spanning (∼930-2400 nm, f_{rep}= 1 THz) soliton microcomb. Such dual-mode will also enrich the soliton dy-

namics especially, the soliton crystals. We also observed the avoided mode crossing (AMX) induced octave-spanning perfect soliton crystal (PSC) in multiple devices but with various repetition rates ($f_{rep} \approx$ 4, 5, 6, 7, 8 THz). The achieved PSCs have low noise and enhanced individual line power. Furthermore, the temperature control is an effective tool to tune the resonance modes therefore fabrication of the micro-heaters will be worth exploring the PSCs behavior.

Self-referencing soliton microcombs for timing and precision metrology [154][14] will greatly impact the fundamental science and technical applications. The low conversion efficiency (CE) and high pump power in single solitons are crucial limitations for on-chip integration [150]. In future work, we would focus to optimize the cavity design to realize the broadband soliton microcomb with further improved CE and enhanced intensities of the dispersive waves at both blue and red sides. Firstly, a 'perfect' silicon nitride resonator geometry supporting a near-zero anomalous dispersion will be designed through the simulations of COMSOL and LLE. This design will offer the octave-spanning single-soliton microcombs with hundreds of GHz repetition rates, which could be characterized by another microcomb or EO comb [15][14]. Secondly, we will design an integrated chip consisting of two microresonators with different repetition rates of THz and 30 GHz or less, respectively, for f_{rep} characterization. The f_{ceo} was found to be associated with the geometry and we will attempt to design it for low frequency, which can be electrically detected [135].

Finally, to reduce the cost and complexity, we are replacing the tunable laser with a semiconductor laser chip to generate the soliton microcomb generation. The EDFA will be removed once the Q factors of the dual-mode AlN microresonators are improved to a level of about 4×10^6. Then a highly compact soliton microcomb source with simplified experimental protocol and reduced cost will be delivered.

Bibliography

[1] H Schnatz et al. "First phase-coherent frequency measurement of visible radiation". In: *Physical Review Letters* 76.1 (1996), p. 18.

[2] Th Udem, Ronald Holzwarth, and Theodor W Hänsch. "Optical frequency metrology". In: *Nature* 416.6877 (2002), pp. 233–237.

[3] Florian Tauser, Alfred Leitenstorfer, and Wolfgang Zinth. "Amplified femtosecond pulses from an Er: fiber system: Nonlinear pulse shortening and self-referencing detection of the carrier-envelope phase evolution". In: *Optics express* 11.6 (2003), pp. 594–600.

[4] Steven T Cundiff. "Phase stabilization of ultrashort optical pulses". In: *Journal of Physics D: Applied Physics* 35.8 (2002), R43.

[5] Brian R Washburn et al. "Fiber-laser-based frequency comb with a tunable repetition rate". In: *Optics Express* 12.20 (2004), pp. 4999–5004.

[6] R Holzwarth et al. "Optical frequency synthesizer for precision spectroscopy". In: *Physical review letters* 85.11 (2000), p. 2264.

[7] Th Udem et al. "Absolute frequency measurements of the Hg+ and Ca optical clock transitions with a femtosecond laser". In: *Physical review letters* 86.22 (2001), p. 4996.

[8] Scott A Diddams, Leo Hollberg, and Vela Mbele. "Molecular fingerprinting with the resolved modes of a femtosecond laser frequency comb". In: *Nature* 445.7128 (2007), pp. 627–630.

[9] Pascal Del'Haye et al. "Optical frequency comb generation from a monolithic microresonator". In: *Nature* 450.7173 (2007), pp. 1214–1217.

[10] G Rohit, J Heebner, and T Ibrahim. "Optical microresonators". In: *Optical Microresonators: theory, fabrication, and applications* (2008), pp. 1–2.

[11] Scott A Diddams et al. "Direct link between microwave and optical frequencies with a 300 THz femtosecond laser comb". In: *Physical review letters* 84.22 (2000), p. 5102.

[12] Pascal Del'Haye et al. "Octave spanning tunable frequency comb from a microresonator". In: *Physical Review Letters* 107.6 (2011), p. 063901.

[13] Tobias J Kippenberg, Ronald Holzwarth, and Scott A Diddams. "Microresonator-based optical frequency combs". In: *science* 332.6029 (2011), pp. 555–559.

[14] Tara E Drake et al. "Terahertz-rate Kerr-microresonator optical clockwork". In: *Physical Review X* 9.3 (2019), p. 031023.

[15] Daryl T Spencer et al. "An optical-frequency synthesizer using integrated photonics". In: *Nature* 557.7703 (2018), pp. 81–85.

[16] Victor Brasch et al. "Photonic chip–based optical frequency comb using soliton Cherenkov radiation". In: *Science* 351.6271 (2016), pp. 357–360.

[17] Tobias Herr et al. "Temporal solitons in optical microresonators". In: *Nature Photonics* 8.2 (2014), pp. 145–152.

[18] Xu Yi et al. "Soliton frequency comb at microwave rates in a high-Q silica microresonator". In: *Optica* 2.12 (2015), pp. 1078–1085.

[19] Mengjie Yu et al. "Mode-locked mid-infrared frequency combs in a silicon microresonator". In: *Optica* 3.8 (2016), pp. 854–860.

[20] Qing Li et al. "Stably accessing octave-spanning microresonator frequency combs in the soliton regime". In: *Optica* 4.2 (2017), pp. 193–203.

[21] Zhichao Ye et al. "Integrated, Ultra-Compact High-Q Silicon Nitride Microresonators for Low-Repetition-Rate Soliton Microcombs". In: *Laser & Photonics Reviews* 16.3 (2022), p. 2100147.

[22] Haizhong Weng et al. "Dual-mode microresonators as straightforward access to octave-spanning dissipative Kerr solitons". In: *APL Photonics* 7.6 (2022), p. 066103.

[23] Gregory Moille et al. “Dissipative Kerr Solitons in a III-V Microresonator”. In: *Laser & Photonics Reviews* 14.8 (2020), p. 2000022.

[24] Yang He et al. “Self-starting bi-chromatic LiNbO 3 soliton microcomb”. In: *Optica* 6.9 (2019), pp. 1138–1144.

[25] Zheng Gong et al. “Near-octave lithium niobate soliton microcomb”. In: *Optica* 7.10 (2020), pp. 1275–1278.

[26] Lutong Cai et al. “Octave-spanning microcomb generation in 4H-silicon-carbide-on-insulator photonics platform”. In: *Photonics Research* 10.4 (2022), pp. 870–876.

[27] Haizhong Weng et al. “Directly accessing octave-spanning dissipative Kerr soliton frequency combs in an AlN microresonator”. In: *Photonics Research* 9.7 (2021), pp. 1351–1357.

[28] Xianwen Liu et al. “Aluminum nitride nanophotonics for beyond-octave soliton microcomb generation and self-referencing”. In: *Nature communications* 12.1 (2021), pp. 1–7.

[29] Hojoong Jung et al. “Tantala Kerr nonlinear integrated photonics”. In: *Optica* 8.6 (2021), pp. 811–817.

[30] Yanzhen Zheng et al. “Integrated gallium nitride nonlinear photonics”. In: *Laser & Photonics Reviews* 16.1 (2022), p. 2100071.

[31] Ioannis Chremmos, Otto Schwelb, and Nikolaos Uzunoglu. *Photonic microresonator research and applications*. Vol. 156. Springer, 2010.

[32] Wim Bogaerts et al. “Silicon microring resonators”. In: *Laser & Photonics Reviews* 6.1 (2012), pp. 47–73.

[33] Amnon Yariv. “Critical coupling and its control in optical waveguide-ring resonator systems”. In: *IEEE Photonics Technology Letters* 14.4 (2002), pp. 483–485.

[34] Jacob Levy. “Integrated nonlinear optics in silicon nitride waveguides and resonators”. In: (Thesis 2011).

[35] John Heebner, Rohit Grover, and Tarek Ibrahim. *Optical Microresonators: Theory, Fabrication, and Applications*. eng. Vol. 138. Optical Sciences. New York, NY: Springer New York. ISBN: 0387730672.

[36] Jia Liu et al. "Photolithography allows high-Q AlN microresonators for near octave-spanning frequency comb and harmonic generation". In: *Optics Express* 28.13 (2020), pp. 19270–19280.

[37] "See https://www.ligentec.com/ligentec-foundry/mpw/ for information regarding the fabrication". In: ().

[38] Chi Xiong et al. "Aluminum nitride as a new material for chip-scale optomechanics and nonlinear optics". In: *New Journal of Physics* 14.9 (2012), p. 095014.

[39] Xianwen Liu et al. "Aluminum nitride-on-sapphire platform for integrated high-Q microresonators". In: *Optics express* 25.2 (2017), pp. 587–594.

[40] Hojoong Jung et al. "Green, red, and IR frequency comb line generation from single IR pump in AlN microring resonator". In: *Optica* 1.6 (2014), pp. 396–399.

[41] Zheng Gong et al. "High-fidelity cavity soliton generation in crystalline AlN micro-ring resonators". In: *Optics letters* 43.18 (2018), pp. 4366–4369.

[42] Yanzhen Zheng et al. "Soliton comb generation in air-clad AlN microresonators". In: *CLEO: Science and Innovations*. Optical Society of America. 2020, SW4J–3.

[43] Xiang Guo et al. "Efficient generation of a near-visible frequency comb via Cherenkov-like radiation from a Kerr microcomb". In: *Physical Review Applied* 10.1 (2018), p. 014012.

[44] Alexander W Bruch et al. "On-chip χ (2) microring optical parametric oscillator". In: *Optica* 6.10 (2019), pp. 1361–1366.

[45] Alexander W Bruch et al. "Pockels soliton microcomb". In: *Nature Photonics* 15.1 (2021), pp. 21–27.

[46] Yi Zhang et al. “Fast growth of high quality AlN films on sapphire using a dislocation filtering layer for ultraviolet light-emitting diodes”. In: *CrystEngComm* 21.27 (2019), pp. 4072–4078.

[47] Govind P Agrawal. “Nonlinear fiber optics”. In: *Nonlinear Science at the Dawn of the 21st Century*. Springer, 2000, pp. 195–211.

[48] Teng Tan et al. “Multispecies and individual gas molecule detection using Stokes solitons in a graphene over-modal microresonator”. In: *Nature communications* 12.1 (2021), pp. 1–8.

[49] Jindong Wang et al. “Long-distance ranging with high precision using a soliton microcomb”. In: *Photonics Research* 8.12 (2020), pp. 1964–1972.

[50] Johann Riemensberger et al. “Massively parallel coherent laser ranging using a soliton microcomb”. In: *Nature* 581.7807 (2020), pp. 164–170.

[51] Shun Fujii and Takasumi Tanabe. “Dispersion engineering and measurement of whispering gallery mode microresonator for Kerr frequency comb generation”. In: *Nanophotonics* 9.5 (2020), pp. 1087–1104.

[52] T Herr et al. “Universal formation dynamics and noise of Kerr-frequency combs in microresonators”. In: *Nature photonics* 6.7 (2012), pp. 480–487.

[53] Tobias J Kippenberg et al. “Dissipative Kerr solitons in optical microresonators”. In: *Science* 361.6402 (2018), eaan8083.

[54] C Milián and DV Skryabin. “Soliton families and resonant radiation in a micro-ring resonator near zero group-velocity dispersion”. In: *Optics express* 22.3 (2014), pp. 3732–3739.

[55] Nail Akhmediev and Magnus Karlsson. “Cherenkov radiation emitted by solitons in optical fibers”. In: *Physical Review A* 51.3 (1995), p. 2602.

[56] Martin HP Pfeiffer et al. “Octave-spanning dissipative Kerr soliton frequency combs in Si_3N_4 microresonators”. In: *Optica* 4.7 (2017), pp. 684–691.

[57] Haizhong Weng et al. “Octave-spanning Kerr frequency comb generation with stimulated Raman scattering in an AlN microresonator”. In: *Optics Letters* 46.3 (2021), pp. 540–543.

[58] Adnan Ali Afridi et al. “Breather solitons in AlN microresonators”. In: *Optics Continuum* 1.1 (2022), pp. 42–50.

[59] Cheng Wang et al. “Monolithic lithium niobate photonic circuits for Kerr frequency comb generation and modulation”. In: *Nature communications* 10.1 (2019), pp. 1–6.

[60] Zihan Li et al. “Tightly confining lithium niobate photonic integrated circuits and lasers”. In: *arXiv preprint arXiv:2208.05556* (2022).

[61] Mingbo He et al. “High-performance hybrid silicon and lithium niobate Mach–Zehnder modulators for 100 Gbit s- 1 and beyond”. In: *Nature Photonics* 13.5 (2019), pp. 359–364.

[62] Mian Zhang et al. “Broadband electro-optic frequency comb generation in a lithium niobate microring resonator”. In: *Nature* 568.7752 (2019), pp. 373–377.

[63] Joerg Pfeifle et al. “Coherent terabit communications with microresonator Kerr frequency combs”. In: *Nature photonics* 8.5 (2014), pp. 375–380.

[64] Di Zhu et al. “Integrated photonics on thin-film lithium niobate”. In: *Advances in Optics and Photonics* 13.2 (2021), pp. 242–352.

[65] Ewelina Obrzud et al. “Stable and compact RF-to-optical link using lithium niobate on insulator waveguides”. In: *APL Photonics* 6.12 (2021), p. 121303.

[66] Zachary L Newman et al. “Architecture for the photonic integration of an optical atomic clock”. In: *Optica* 6.5 (2019), pp. 680–685.

[67] Pablo Marin-Palomo et al. “Microresonator-based solitons for massively parallel coherent optical communications”. In: *Nature* 546.7657 (2017), pp. 274–279.

[68] Mikael Mazur et al. “High spectral efficiency coherent superchannel transmission with soliton microcombs”. In: *Journal of Lightwave Technology* 39.13 (2021), pp. 4367–4373.

[69] Myoung-Gyun Suh and Kerry J Vahala. “Soliton microcomb range measurement”. In: *Science* 359.6378 (2018), pp. 884–887.

[70] Victor Brasch et al. “Bringing short-lived dissipative Kerr soliton states in microresonators into a steady state”. In: *Optics express* 24.25 (2016), pp. 29312–29320.

[71] Xu Yi et al. “Active capture and stabilization of temporal solitons in microresonators”. In: *Optics letters* 41.9 (2016), pp. 2037–2040.

[72] Chaitanya Joshi et al. “Thermally controlled comb generation and soliton modelocking in microresonators”. In: *Optics letters* 41.11 (2016), pp. 2565–2568.

[73] Avik Dutt et al. “On-chip dual-comb source for spectroscopy”. In: *Science advances* 4.3 (2018), e1701858.

[74] Naoya Kuse et al. “Continuous scanning of a dissipative Kerr-microresonator soliton comb for broadband, high-resolution spectroscopy”. In: *Optics Letters* 45.4 (2020), pp. 927–930.

[75] Zhizhou Lu et al. “Deterministic generation and switching of dissipative Kerr soliton in a thermally controlled micro-resonator”. In: *Aip Advances* 9.2 (2019), p. 025314.

[76] Heng Zhou et al. “Soliton bursts and deterministic dissipative Kerr soliton generation in auxiliary-assisted microcavities”. In: *Light: Science & Applications* 8.1 (2019), pp. 1–10.

[77] Thibault Wildi et al. “Thermally stable access to microresonator solitons via slow pump modulation”. In: *Optics letters* 44.18 (2019), pp. 4447–4450.

[78] Sven Ramelow et al. “Strong polarization mode coupling in microresonators”. In: *Optics letters* 39.17 (2014), pp. 5134–5137.

[79] Yang Liu et al. “Investigation of mode coupling in normal-dispersion silicon nitride microresonators for Kerr frequency comb generation”. In: *optica* 1.3 (2014), pp. 137–144.

[80] Elham Nazemosadat et al. “Switching dynamics of dark-pulse Kerr frequency comb states in optical microresonators”. In: *Physical Review A* 103.1 (2021), p. 013513.

[81] Qi-Fan Yang et al. “Spatial-mode-interaction-induced dispersive waves and their active tuning in microresonators”. In: *Optica* 3.10 (2016), pp. 1132–1135.

[82] Maxim Karpov et al. “Dynamics of soliton crystals in optical microresonators”. In: *Nature Physics* 15.10 (2019), pp. 1071–1077.

[83] Bill Corcoran et al. “Ultra-dense optical data transmission over standard fibre with a single chip source”. In: *Nature Communications* 11.1 (2020), pp. 1–7.

[84] Xiaoxiao Xue et al. “Normal-dispersion microcombs enabled by controllable mode interactions”. In: *Laser & Photonics Reviews* 9.4 (2015), pp. L23–L28.

[85] Hairun Guo et al. “Universal dynamics and deterministic switching of dissipative Kerr solitons in optical microresonators”. In: *Nature Physics* 13.1 (2017), pp. 94–102.

[86] Mengjie Yu et al. “Breather soliton dynamics in microresonators”. In: *Nature communications* 8.1 (2017), pp. 1–7.

[87] T Herr et al. “Mode spectrum and temporal soliton formation in optical microresonators”. In: *Physical review letters* 113.12 (2014), p. 123901.

[88] Travis C Briles et al. “Interlocking Kerr-microresonator frequency combs for microwave to optical synthesis”. In: *Optics letters* 43.12 (2018), pp. 2933–2936.

[89] Alexander Gondarenko, Jacob S Levy, and Michal Lipson. “High confinement micron-scale silicon nitride high Q ring resonator”. In: *Optics express* 17.14 (2009), pp. 11366–11370.

[90] T. Herr et al. “Temporal solitons in optical microresonators”. In: *Nature photonics* 8.2 (2013), pp. 145–152.

[91] Xiaoxiao Xue et al. “Mode-locked dark pulse Kerr combs in normal-dispersion microresonators”. In: *Nature Photonics* 9.9 (2015), pp. 594–600.

[92] Shuangyou Zhang et al. “Dark-bright soliton bound states in a microresonator”. In: *Physical Review Letters* 128.3 (2022), p. 033901.

[93] Wenle Weng et al. “Heteronuclear soliton molecules in optical microresonators”. In: *Nature communications* 11.1 (2020), pp. 1–9.

[94] Qi-Fan Yang et al. “Stokes solitons in optical microcavities”. In: *Nature Physics* 13.1 (2017), pp. 53–57.

[95] Yang He et al. “Perfect soliton crystals on demand”. In: *Laser & Photonics Reviews* 14.8 (2020), p. 1900339.

[96] Erwan Lucas et al. “Breathing dissipative solitons in optical microresonators”. In: *Nature communications* 8.1 (2017), pp. 1–11.

[97] Erwan Lucas et al. “Detuning-dependent properties and dispersion-induced instabilities of temporal dissipative Kerr solitons in optical microresonators”. In: *Physical Review A* 95.4 (2017), p. 043822.

[98] AB Matsko, AA Savchenkov, and L Maleki. “On excitation of breather solitons in an optical microresonator”. In: *Optics letters* 37.23 (2012), pp. 4856–4858.

[99] Chengying Bao et al. “Observation of Fermi-Pasta-Ulam recurrence induced by breather solitons in an optical microresonator”. In: *Physical review letters* 117.16 (2016), p. 163901.

[100] Luigi A Lugiato and René Lefever. “Spatial dissipative structures in passive optical systems”. In: *Physical review letters* 58.21 (1987), p. 2209.

[101] Stéphane Coen and Miro Erkintalo. “Universal scaling laws of Kerr frequency combs”. In: *Optics letters* 38.11 (2013), pp. 1790–1792.

[102] Hojoong Jung et al. “Optical frequency comb generation from aluminum nitride microring resonator”. In: *Optics letters* 38.15 (2013), pp. 2810–2813.

[103] BJM Hausmann et al. “Diamond nonlinear photonics”. In: *Nature Photonics* 8.5 (2014), pp. 369–374.

[104] Xianwen Liu et al. “Integrated high-Q crystalline AlN microresonators for broadband Kerr and Raman frequency combs”. In: *ACS Photonics* 5.5 (2018), pp. 1943–1950.

[105] Carles Milián et al. “Solitons and frequency combs in silica microring resonators: Interplay of the Raman and higher-order dispersion effects”. In: *Physical Review A* 92.3 (2015), p. 033851.

[106] Maxim Karpov et al. “Raman self-frequency shift of dissipative Kerr solitons in an optical microresonator”. In: *Physical review letters* 116.10 (2016), p. 103902.

[107] Yoshitomo Okawachi et al. “Competition between Raman and Kerr effects in microresonator comb generation”. In: *Optics Letters* 42.14 (2017), pp. 2786–2789.

[108] Shun Fujii et al. “Transition between Kerr comb and stimulated Raman comb in a silica whispering gallery mode microcavity”. In: *JOSA B* 35.1 (2018), pp. 100–106.

[109] M Bickermann et al. “Orientation-dependent phonon observation in single-crystalline aluminum nitride”. In: *Applied Physics Letters* 86.13 (2005), p. 131904.

[110] Stéphane Coen et al. “Modeling of octave-spanning Kerr frequency combs using a generalized mean-field Lugiato–Lefever model”. In: *Optics letters* 38.1 (2013), pp. 37–39.

[111] Gregory Moille et al. “pyLLE: A fast and user friendly Lugiato-Lefever equation solver”. In: *Journal of Research of the National Institute of Standards and Technology* 124 (2019), p. 1.

[112] Daniel C Cole et al. “Soliton crystals in Kerr resonators”. In: *Nature Photonics* 11.10 (2017), pp. 671–676.

[113] Pascal Del’Haye et al. “Phase steps and resonator detuning measurements in microresonator frequency combs”. In: *Nature communications* 6.1 (2015), pp. 1–9.

[114] Weiqiang Wang et al. “Robust soliton crystals in a thermally controlled microresonator”. In: *Optics letters* 43.9 (2018), pp. 2002–2005.

[115] Rui Niu et al. “Perfect soliton crystals in the high-Q microrod resonator”. In: *IEEE Photonics Technology Letters* 33.15 (2021), pp. 788–791.

[116] Chengying Bao et al. “Spatial mode-interaction induced single soliton generation in microresonators”. In: *Optica* 4.9 (2017), pp. 1011–1015.

[117] Ayata Nakashima et al. “Deterministic generation of a perfect soliton crystal microcomb with a saturable absorber”. In: *Optics Letters* 47.6 (2022), pp. 1458–1461.

[118] Jin Li et al. “Thermal tuning of mode crossing and the perfect soliton crystal in a Si 3 N 4 microresonator”. In: *Optics Express* 30.8 (2022), pp. 13690–13698.

[119] Tianye Huang et al. “Nonlinear-mode-coupling-induced soliton crystal dynamics in optical microresonators”. In: *Physical Review A* 103.2 (2021), p. 023502.

[120] Victor Brasch et al. “Self-referenced photonic chip soliton Kerr frequency comb”. In: *Light: Science & Applications* 6.1 (2017), e16202–e16202.

[121] Philipp Trocha et al. “Ultrafast optical ranging using microresonator soliton frequency combs”. In: *Science* 359.6378 (2018), pp. 887–891.

[122] Paolo Ghelfi et al. “A fully photonics-based coherent radar system”. In: *Nature* 507.7492 (2014), pp. 341–345.

[123] Myoung-Gyun Suh et al. “Microresonator soliton dual-comb spectroscopy”. In: *Science* 354.6312 (2016), pp. 600–603.

[124] Wei Liang et al. “High spectral purity Kerr frequency comb radio frequency photonic oscillator”. In: *Nature communications* 6.1 (2015), pp. 1–8.

[125] Ewelina Obrzud et al. “A microphotonic astrocomb”. In: *Nature Photonics* 13.1 (2019), pp. 31–35.

[126] Kazuhiro Ikeda et al. “Thermal and Kerr nonlinear properties of plasma-deposited silicon nitride/silicon dioxide waveguides”. In: *Optics express* 16.17 (2008), pp. 12987–12994.

[127] Jacob S Levy et al. “CMOS-compatible multiple-wavelength oscillator for on-chip optical interconnects”. In: *Nature photonics* 4.1 (2010), pp. 37–40.

[128] Alexander L Gaeta, Michal Lipson, and Tobias J Kippenberg. “Photonic-chip-based frequency combs”. In: *nature photonics* 13.3 (2019), pp. 158–169.

[129] Abdul Rahim et al. “Expanding the silicon photonics portfolio with silicon nitride photonic integrated circuits”. In: *Journal of lightwave technology* 35.4 (2017), pp. 639–649.

[130] Xingchen Ji et al. “Methods to achieve ultra-high quality factor silicon nitride resonators”. In: *APL Photonics* 6.7 (2021), p. 071101.

[131] Attila Fülöp et al. “High-order coherent communications using mode-locked dark-pulse Kerr combs from microresonators”. In: *Nature communications* 9.1 (2018), pp. 1–8.

[132] Bok Young Kim et al. “Turn-key, high-efficiency Kerr comb source”. In: *Optics letters* 44.18 (2019), pp. 4475–4478.

[133] Mengjie Yu et al. “Gas-phase microresonator-based comb spectroscopy without an external pump laser”. In: *ACS Photonics* 5.7 (2018), pp. 2780–2785.

[134] Scott B Papp et al. “Microresonator frequency comb optical clock”. In: *Optica* 1.1 (2014), pp. 10–14.

[135] Su-Peng Yu et al. “Tuning Kerr-soliton frequency combs to atomic resonances”. In: *Physical Review Applied* 11.4 (2019), p. 044017.

[136] Travis C Briles et al. “Generating octave-bandwidth soliton frequency combs with compact low-power semiconductor lasers”. In: *Physical Review Applied* 14.1 (2020), p. 014006.

[137] Yang He et al. “Octave-spanning lithium niobate soliton microcombs”. In: *CLEO: Science and Innovations*. Optical Society of America. 2021, STu2G–1.

[138] Kenji Nishimoto et al. “Thermal control of a Kerr microresonator soliton comb via an optical sideband”. In: *Optics Letters* 47.2 (2022), pp. 281–284.

[139] Chao Xiang, Warren Jin, and John E Bowers. “Silicon nitride passive and active photonic integrated circuits: trends and prospects”. In: *Photonics Research* 10.6 (2022), A82–A96.

[140] Fuchuan Lei, Zhichao Ye, et al. “Thermal noise reduction in soliton microcombs via laser self-cooling”. In: *Optics Letters* 47.3 (2022), pp. 513–516.

[141] Maxim Karpov et al. “Photonic chip-based soliton frequency combs covering the biological imaging window”. In: *Nature communications* 9.1 (2018), pp. 1–8.

[142] AA Savchenkov et al. “Kerr frequency comb generation in overmoded resonators”. In: *Optics express* 20.24 (2012), pp. 27290–27298.

[143] Haizhong Weng et al. “Near-octave-spanning breathing soliton crystal in an AlN microresonator”. In: *Optics Letters* 46.14 (2021), pp. 3436–3439.

[144] Jianqi Hu et al. “Reconfigurable radiofrequency filters based on versatile soliton microcombs”. In: *Nature communications* 11.1 (2020), pp. 1–9.

[145] Xiaoxiao Xue et al. “Microresonator Kerr frequency combs with high conversion efficiency”. In: *Laser & Photonics Reviews* 11.1 (2017), p. 1600276.

[146] Brian Stern et al. “Battery-operated integrated frequency comb generator”. In: *Nature* 562.7727 (2018), pp. 401–405.

[147] Boqiang Shen et al. “Integrated turnkey soliton microcombs”. In: *Nature* 582.7812 (2020), pp. 365–369.

[148] Haowen Shu et al. “Microcomb-driven silicon photonic systems”. In: *Nature* 605.7910 (2022), pp. 457–463.

[149] Jiang Li et al. “Efficiency of pulse pumped soliton microcombs”. In: *Optica* 9.2 (2022), pp. 231–239.

[150] Jae K Jang et al. “Conversion efficiency of soliton Kerr combs”. In: *Optics Letters* 46.15 (2021), pp. 3657–3660.

[151] Óskar B Helgason et al. “Power-efficient soliton microcombs”. In: *arXiv preprint arXiv:2202.09410* (2022).

[152] Lin Chang, Songtao Liu, and John E Bowers. “Integrated optical frequency comb technologies”. In: *Nature Photonics* 16.2 (2022), pp. 95–108.

[153] Yong Geng et al. “Wavelength-division multiplexing communications using integrated soliton microcomb laser source”. In: *arXiv preprint arXiv:2206.00256* (2022).

[154] Myoung-Gyun Suh et al. “Searching for exoplanets using a microresonator astrocomb”. In: *Nature photonics* 13.1 (2019), pp. 25–30.